Electronic Structure and Transport Properties of Quantum Dots

Dissertation
zur Erlangung des Doktorgrades
des Fachbereichs Physik
der Universität Hamburg

vorgelegt von
Michael Tews
aus Nürtingen

Hamburg
2004

Gutachter der Dissertation:	Prof. Dr. D. Pfannkuche Prof. Dr. J. König
Gutachter der Disputation:	Prof. Dr. D. Pfannkuche PD Dr. M. Morgenstern
Datum der Disputation:	30. Januar 2004
Vorsitzender des Prüfungsauschusses:	Prof. Dr. D. Fay
Vorsitzender des Promotionsausschusses:	Prof. Dr. R. Wiesendanger
Dekan des Fachbereichs Physik:	Prof. Dr. G. Huber

Electronic Structure and Transport Properties of Quantum Dots

Michael Tews

Universität Hamburg, Germany

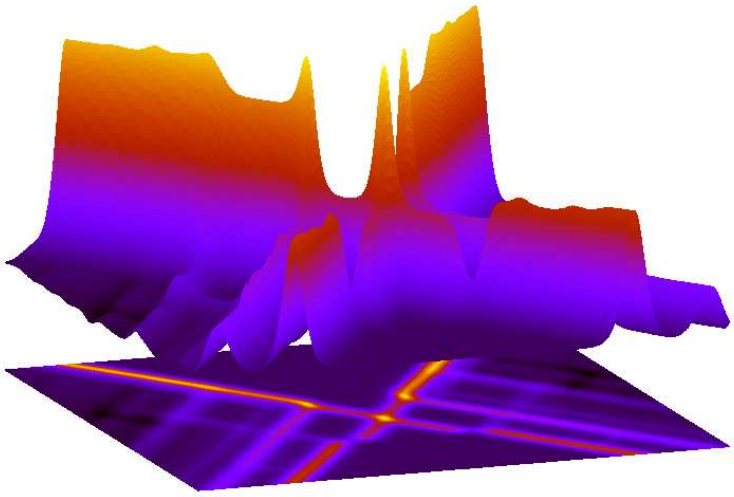

Abstract

The subject of this thesis are electronic properties of isolated quantum dots as well as transport properties of quantum dots coupled to two electronic reservoirs. Thereby special focus is put on the effects of Coulomb interaction and possible correlations in the quantum dot states.

First, the regime where the quantum dot is only weakly coupled to the reservoirs is investigated by using a master equation approach with tunneling rates obtained by Fermi's Golden Rule. It is shown that in case more than two quantum dot states participate in transport, the resonance positions in the differential conductance generally depend on temperature and the number of participating states. Therefore transport spectra generally cannot be interpreted in a straightforward manner by the energy levels of the isolated quantum dot. At the same time it is shown how this effect can be used to directly probe degeneracies in a quantum dot spectrum. In a spherical quantum dot occupied by two and three Coulomb interacting electrons, a mechanism is found which leads to a complete blocking of the quantum dot for transport. This blocking mechanism results in an enhancement of the Coulomb blockade regime where transport is exponentially suppressed and is explained by a cascade of transitions which ends in a state blocked for further transport due to spin-selection rules.

In the second part, the electronic structure of spherical quantum dots is calculated within a particle-in-a-sphere model for interacting electrons. In order to account for correlation effects, the few-particle Schrödinger equation is solved by an exact diagonalization procedure. It is shown that the calculated electronic structure compares to experimental findings obtained on colloidal semiconductor nanocrystals by Scanning Tunneling Spectroscopy. The electric field induced by the tunneling tip is studied and it is found that the resulting Stark effect can lead to a toroidal symmetry of the electronic ground state density which is in agreement with wave-function mapping experiments. For the five-particle ground state it is found that the symmetry depends on the nanocrystal radius. This is explained by a competition between exchange energy and the Stark energy.

Studying the excitation spectrum, it is found that Coulomb interaction can lead to a reduction of the low lying excitations for increasing number of electrons occupying the quantum dot which explains recent experimental findings on self-organized quantum dots.

In the last part, co-tunneling in the Coulomb blockade regime is studied. For this end the tunneling current is calculated up to the forth order perturbation theory in the tunnel coupling by a real-time Green's function approach for the non-equilibrium case. The differential conductance calculated for a quantum dot containing up to two interacting electrons shows complex signatures of the excitation spectrum which are explained by a combination of co-tunneling and

sequential tunneling processes. Thereby the calculations show a peak structure within the Coulomb blockade regime which has also been observed in experiment.

Zusammenfassung

Diese Arbeit beschäftigt sich mit den elektronische Eigenschaften von isolierten Quantenpunkten sowie Transporteigenschaften von Quantenpunkten die mittels Tunnelbarrieren an zwei elektronische Reservoire gekoppelt sind.

Zunächst wird das Regime schwacher Tunnelankopplung untersucht, welches mittels einer Master-Gleichung mit Tunnelraten nach Fermis Goldener Regel beschrieben wird. Tragen mehr als zwei Quantenpunktzustände zum Transport bei, wird gezeigt, dass die Position der differenziellen Leitfähigkeitsspitzen im Allgemeinen von der Anzahl der beitragenden Zustände sowie von der Temperatur abhängt. Dadurch können Transportspektren in der Regel nicht unmittelbar mit Hilfe der Energieniveaus des isolierten Quantenpunktes interpretiert werden. Gleichzeitig wird ein Weg aufgezeigt, der es erlaubt mit Hilfe dieser Abhänigkeiten Entartungen in Quantenpunktspektren direkt zu messen. Desweiteren wird ein Mechanismus am Beispiel eines spärischen Quantuenpunktes der mit zwei bis drei wechselwirkenden Elektronen besetzt ist, untersucht. Er führt zu einer Erweiterung des Coulomb-Blockadebereichs, indem der Quantenpunkt für Transport vollständig blockiert ist. Dieser Mechanismus kann durch eine Kaskade von Tunnelübergängen erklärt werden, die in einem Quantenpunktzustand endet welche für weiteren Transport durch Spinauswahlregeln blockiert ist.

Im zweiten Teil dieser Arbeit wird die elektronische Struktur sphärischer Quantenpunkte mittels eines effektiven Massenmodells für wechselwirkende Elektronen berechnet. Um Korrelationen in den Quantenpunktzuständen zu berücksichtigen, wird die Vielteilchen Schrödinger Gleichung mittels exakter Diagonalisierung gelöst. Die berechnete elektronische Struktur steht im Einklang mit Transportexperimenten an Halbleiternanokristallen, die mittels Rastertunnelspektroskopie durchgeführt wurden. Bei der Berechnung des Starkeffekts aufgrund des durch die Rastertunnelspitze induzierten elektrische Feldes wird gezeigt, dass bestimmet Grundzustandsdichten eine torusförmige Symmetrie besitzen. Diese Symmetrie wurde experimentell in sogenannten Wellenfunktionskartierungsexperimenten nachgewiesen. Eine Größenabhängigkeit der Symmetrie gibt es im Grundzustand für fünf Elektronen aufgrund eines Wechselspiels zwischen Starkenergie und Austauschenergie.

Des weiteren zeigt die Berechnung der Anregungspektren des isolierten Quantenpunkts, dass die Coulombwechselwirkung zu einer Reduktion der tiefliegenden Anregungen als Funktion der Elektronenzahl führen kann. Diese Reduktion erkärt aktuelle experimentelle Befunde an selbstorganisierten Halbleiterquantenpunkten.

Der letzte Teil behandelt die Untersuchung von Co-Tunnel-Prozesse im Bereich der Coulomb-Blockade. Dazu wird der Tunnelstrom in vierter Ordnung

Störungstheorie in der Tunnelankopplung mittels eines Echtzeit-Greensfunktionenansatzes im Nichtgleichgewicht berechnet. Für einen Quantenpunkt, der mit bis zu zwei wechselwirkenden Elektronen besetzt werden kann zeigt die berechnete differenzielle Leitfähigkeit eine komplexe Struktur des Anregungsspektrums innerhalb des Coulomb-Blockadebereichs. Dabei zeigen die Rechnungen neben Stufen insbesondere Spitzen in der differentiellen Leitfähigkeit, die auch experimentell gefunden wurden.

Acknowledgments

I want to acknowledge the support of many people, without whom this work would not have been possible.

- **Daniela Pfannkuche** was my supervisor and competent in all questions concerning quantum dots and transport. She read the manuscript for this thesis very carefully.
- **Alexander Chudnovskiy** was always interested in my work and contributed to many discussions about my results.
- **Markus Morgenstern** contributed many valuable ideas connected to the nanocrystals in STM setup.
- **Christian Schüller** gave me an interesting insight in Raman spectroscopy on quantum dots which lead to a very fruitful collaboration.
- **Bernhard Wunsch** was always interested in my work which lead to innumerable interesting discussions about physics and the "outside" world. He also read the manuscript for this thesis carefully.
- **Karel Výborný** carefully read the manuscript for this thesis. He also did contribute to this work due to competent help in questions concerning physics and especially mathematics.
- **Benjamin Krüger** contributed computer code to the program package calculating the electronic structure of spherical quantum dots and also helped in vectorizing the co-tunneling transport program.
- **Frank Hellmuth** answered all my questions concerning data plotting and LaTeX.
- **David Jacob** was my office mate with whom I enjoyed discussing questions related to the quantum mechanical few-particle problem. With his very special humor he contributed to a relaxed atmosphere.
- **Till Vorrath** was always interested in the progress of this work which lead to some very helpful discussions.

- **Mark Görbig** was my first colleague and considerably contributed to a good working atmosphere.

Of course I want to thank all my colleagues for the good atmosphere at the institute. Finally, much thanks to my family and especially to my girl-friend Katrin who was patient whenever I spent too much time at work. In case I have missed somebody in the list I kindly ask the person to not feel offended and blame it on my forgetfulness.

Contents

1 Introduction **1**

2 Sequential Transport in Semiconductor Quantum Dots **5**
2.1 Basic Concepts of Sequential Transport 6
2.1.1 Model Hamiltonian 6
2.1.2 Transition Rates 8
2.1.3 Tunneling Current and Master Equation 10
2.1.4 Coulomb Blockade 11
2.1.5 Charging Diagram 12
2.2 Multi-channel Transport at Finite Temperatures 14
2.2.1 Degenerate Quantum Dot States 14
2.3 Correlation Effects and Spectral Weights 18
2.3.1 Ground State Channel Blocking in Non-linear Transport . 22

3 Colloidal Semiconductor Nanocrystals **27**
3.1 Transport Experiments 28
3.1.1 Scanning Tunneling Spectroscopy 29
3.1.2 Wave-function Mapping 30
3.2 Electronic Quantum Dot States 32
3.2.1 Single-particle States 32
3.2.2 Energy-dependent Effective Mass 34
3.2.3 Few-particle States 35
3.2.4 Exact Diagonalization 36
3.2.5 Coulomb Matrix Elements 37
3.2.6 Shell-tunneling and Shell-filling Spectroscopy 40
3.2.7 Excitation Spectra 43
3.3 Quantum Confined Stark Effect 47
3.3.1 Tip-induced Electrostatic Field 47
3.3.2 Single-particle Calculation 48
3.3.3 Few-particle Calculations: Stark versus Exchange 52

4 Co-tunneling Effects in Charge Transport **57**
4.1 Real-time Transport Theory 59
4.1.1 Hamiltonian 59
4.1.2 Formalism and Diagrams 60
4.1.3 Kinetic Equation 66
4.1.4 Mirror Symmetry 69
4.1.5 Current 70
4.1.6 Stationary Density Matrix and Current 71
4.1.7 Sequential Tunneling 71
4.1.8 Diagrammatic Rules in Energy Space 73
4.2 Co-tunneling 74
4.2.1 Diagrams 74
4.2.2 Example of a Co-tunneling Contribution 75
4.3 Signatures of the Excitation Spectrum in the Coulomb Blockade Regime 77

5 Conclusions **83**

A Spectral Weights **85**
A.1 Sequential Tunneling 85
A.2 Co-tunneling 86

B Transformed Time-evolution Operator **88**
B.1 Transport Hamiltonian 89

C Commutators **92**

D Interaction Picture **97**

E Keldysh Contour **98**

F Separation of Reservoir and Dot Operators **100**

G Co-tunneling Energy Integrals **102**
G.1 Integrals of 1st Kind 102
G.2 Integrals of 2nd Kind 104

List of Figures

2.1 Schematic transport setup of a quantum dot 6
2.2 Sequential tunneling process 9
2.3 Coulomb blockade 11
2.4 Example of a charging diagram 12
2.5 Linear transport through a single channel 14
2.6 Linear transport through a degenerate channel 16
2.7 Non-linear transport through a degenerate channel 17
2.8 Spectral weights 19
2.9 Occupation probability 20
2.10 Channel blocking 22
2.11 Transport channels 23
2.12 Blocking cascade 24

3.1 Scanning Tunneling Spectroscopy of nanocrystals 29
3.2 Differential conductance of nanocrystals 30
3.3 Differential conductance of core-shell system 31
3.4 Wave-function mapping data 31
3.5 Single-particle states 34
3.6 Energy profile of the three lowest transport channels 42
3.7 Ground state channel energies 43
3.8 Excitation spectra 44
3.9 Dielectric core-shell sphere 48
3.10 Perturbative quantum confined Stark effect 50
3.11 Electronic densities in an electric field 50
3.12 Stark effect in an InAs nanocrystal 51
3.13 Ground state configurations 53
3.14 Five-electron states as a function of the electric field strength . . . 54
3.15 Ground state as a function of the nanocrystal size 55
3.16 Five-particle density 56

4.1 Keldysh contour 63
4.2 Time evolution of reduced density operator 64
4.3 Second order diagram 66
4.4 Second order kernel diagrams 67

4.5 Dyson like equation of the reduced density matrix 68
4.6 Mirror symmetry 69
4.7 Dyson like equation of the current 70
4.8 Sequential tunneling diagrams 72
4.9 Co-tunneling diagrams 74
4.10 Transport channels 77
4.11 Charging diagram in the sequential tunneling approximation . . . 78
4.12 Co-tunneling in the Coulomb blockade regime 78
4.13 Energy profile: inelastic co-tunneling 79
4.14 Energy profile: inelastic co-tunneling and sequential tunneling . . 80
4.15 Schematic charging diagram in co-tunneling approximation 80
4.16 Calculated charging diagram in co-tunneling approximation 81
4.17 Inelastic co-tunneling diagram 82

List of Tables

3.1 Comparison of $1S$-$1P$ excitation energies 34
3.2 First order correction in the Coulomb operator 45

4.1 Vertex time orderings of co-tunneling diagrams 74

Chapter 1

Introduction

One of the most interesting questions of topical solid-state research is: What happens if current carrying devices are reduced in size down to the nanometer scale? The answer to this question is not only of fundamental interest, but it is also of great importance for semiconductor industries. The rapid progress in scaling down the basic building blocks of many electronic devices has already approached the 100 nm scale and within ten to fifteen years, feature sizes in production are expected to reach 10 nm [1].

For device sizes in the order of or smaller than the phase-coherence length quantum effects start to play an important role and the devices have to be treated as actual quantum systems. The physics of these structures intermediate between atomic and macroscopic scales, turned out to be so rich that the field got its own name, nowadays known as mesoscopic physics. A typical property of mesoscopic systems is a large number of energy-scales and particles leading to the necessity to develop effective models. Beyond that those quantum systems are usually not isolated but incorporated in an electrical circuit and therefore coupled to some macroscopic reservoirs. Such a coupling generally leads to a loss of phase-coherence in the actual quantum system and touches the question how quantum effects are observed in the macroscopic world.

The current carrying device subject to this work is a quantum dot coupled by tunneling barriers to two lead electrodes. A quantum dot is a *zero-dimensional structure* in which the electronic motion is confined in all three spatial directions, which leads to discretized energy levels of the electronic states in the isolated dot [2]. Due to the coupling to the macroscopically large lead electrodes the electronic structure of the quantum dot can strongly deviate from the isolated case. In this work transport properties of quantum dots are investigated analytically and numerically in the regime of weak and intermediate tunnel coupling to the connecting reservoirs. Thereby special attention is paid to the effect of electronic correlations in the quantum dot states on transport properties.

The best understood transport regime so far is the regime where the quantum dot is only weakly coupled to the environment [3, 4]. In that case the effect of

the reservoirs can be described in the lowest order perturbation theory using Fermi's Golden Rule together with a master equation approach which leads to the concept of *single electron tunneling* [5]. Single electron effects are among the most dramatic new mesoscopic phenomena. The Coulomb energy involved in adding a single electron to a nanometer-sized quantum dot has been found to be the dominant energy scale of the system which can result in a gap in the electronic states of the dot at the Fermi energy such that transport is Coulomb blocked [6, 7]. This led to the discovery of the single-electron transistor [8], in which the transistor action is controlled by a single electron added to or removed from a quantum dot. Open questions still exist also in this regime and some of them are addressed in this work. They are related to correlations in the quantum dot states or to the interplay of many dot states participating in transport.

In the regime of intermediate tunnel coupling no powerful theoretical tool exists to describe coherent transport through a region of interacting electrons for arbitrary tunneling barriers and temperatures. Scattering formalism, which is capable to describe coherent transport, is restricted to non-interacting systems and cannot be applied [9]. On the other hand the master equation approach is non-perturbative in the interactions within the quantum dot, but perturbative in the tunnel coupling and hence restricted to the weak coupling regime. A possibility to describe coherent transport through a region of interacting electrons is to setup a systematic perturbative treatment of the tunneling coupling and to go beyond the lowest order [10]. It turns out that the second non-vanishing order can be interpreted as coherent tunneling processes of pairs of electrons called co-tunneling [11, 12, 13]. Those co-tunneling processes lead e.g. to violation of the Coulomb blockade, but many untouched questions exist. One of the questions, related to the interplay between Coulomb interaction and quantum dot excitations, is studied within this work.

This work is organized as follows:

In **Chapter 2** the basic results of the weak coupling regime are reviewed. It will be shown that most of the experimental finding in the weak coupling regime can be straightforwardly understood by the energy spectrum of the isolated quantum dot together with the concept of single electron tunneling. Nevertheless there are still open questions concerning the interplay of more than two quantum dot states participating in transport. How this interplay can effect transport at finite temperature is addressed in the second part of this chapter. In the last part effects of correlations in the quantum dot states are discussed.

In **Chapter 3** a model is developed allowing to describe the electronic properties of colloidal nanocrystals. Colloidal nanocrystals are spherical quantum dots built of semiconducting materials. Their transport properties have been extensively studied by means of Scanning Tunneling Microscopy (STM). It turns out that the electric field induced by the STM tip can strongly affect the elec-

tronic states in the quantum dot. Consequences for experiments and the dot size dependence are discussed.

In **Chapter 4** the intermediate coupling regime is addressed by considering co-tunneling processes. In the first part of this chapter the Real-time Transport Theory (RTT) developed by SCHOELLER et al. [10] is reviewed, which provides a systematic perturbation theory in the tunneling coupling to the electronic reservoirs for the non-equilibrium case. In the second part the effect of Coulomb interaction and quantum dot excitations on co-tunneling transport is studied within the Coulomb blockade regime.

Publications

Some of the main results of this thesis have been published in the following articles:

- M. Tews and D. Pfannkuche, *"Stark effect in colloidal indium arsenide nanocrystal quantum dots: Consequences for wave-function mapping experiments"*, PRB **65**, 073307 (2001), (This work has been selected for the February 11, 2002 issue of the Virtual Journal of Nanoscale Science & Technology).

- M. Tews and D. Pfannkuche, *"Mapping of few-electron wave-functions in semiconductor nanocrystals - evidence of exchange interaction"*, Proceedings of 26th International Conference on the Physics of Semiconductors, Edinburgh, 2002.

- T. Brocke, M.-T. Bootsmann, B. Wunsch, M. Tews, D. Pfannkuche, Ch. Heyn, W. Hansen, D. Heitmann, and C. Schüller, *"Inelastic Light Scattering on Few-Electron Quantum-Dot Atoms"*, Physica E, in press.

- T. Brocke, M.-T. Bootsmann, M. Tews, B. Wunsch, D. Pfannkuche, Ch. Heyn, W. Hansen, D. Heitmann, and C. Schüller, *"Spectroscopy of Few-Electron Collective Excitations in Charge-Tunable Artifical Atoms"*, PRL **91**, 257401 (2003).

Chapter 2

Sequential Transport in Semiconductor Quantum Dots

Aim of the first part of this chapter is to review the basic concepts and results of transport in the weak coupling regime [3, 4], i.e., where the temperature broadening of the Fermi levels in the reservoirs is much bigger than the finite lifetime broadening of the quantum dot states. It will be shown that in this regime transport is described by sequential tunneling processes where charge is transfered one by one. Due to the only weak coupling of the quantum dot to the reservoirs the spectral density of the quantum dot remains unchanged. At zero temperature this allows a straightforward interpretation of transport data by the isolated quantum dot spectrum which makes it possible to use transport as a spectroscopical tool. In fact, aside from optical spectroscopy, transport in the weak coupling regime has become a major tool to probe the electronic structure of quantum dots [14, 15, 16]. For finite temperatures, the interpretation gets more complicated whenever more than two quantum dot states participate in transport. This hardly addressed detail is discussed in the second part of this chapter. For a quantum dot containing some degenerate states a transparent analytical solution exists which shows a non-trivial dependence of the tunneling characteristic on temperature and degeneracy. At the same time it is discussed how this might allow to directly probe degeneracies of quantum dot states. In the last part of this chapter emphasis will be put on the investigation of correlation effects on the tunneling characteristics. It is already known that the sequential tunneling rates are strongly affected by correlations of the dot electrons [17] which can lead to pronounced phenomena like e.g. spin-blockade [18, 19] and negative differential conductances [20]. As another example of correlation effects a mechanism is discussed which leads to a complete blocking of transport through the quantum dot although tunneling transitions are in principle allowed and energetically possible.

2.1 Basic Concepts of Sequential Transport

The experimental setup of the system considered throughout the entire work is sketched in Fig. 2.1. It consists of a quantum dot connected to two electronic reservoirs via tunneling barriers and possibly some additional gate electrodes. Those gate electrodes couple only electrostatically to the quantum dot and allow to tune the electronic dot potential. Applying a transport voltage between the two reservoirs a tunneling current is driven through the system which strongly

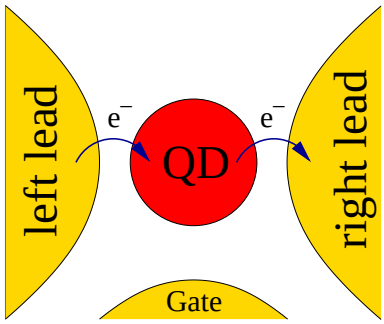

Figure 2.1: Schematic picture of the considered system consisting of a quantum dot in the center connected to two electron reservoirs via tunneling barriers. One or more gate electrodes in the surrounding of the quantum dot, which couple only capacitively to the dot, can be used to tune the electronic potential of the quantum dot.

depends on the electronic structure of the quantum dot.

In the following the Hamiltonian used for the theoretical description is introduced and it will be shown that in the weak coupling regime reservoir electrons are only able to enter the quantum dot if their energy matches the energy needed to charge the quantum dot by a further electron. This condition allows at zero temperature a straightforward interpretation of transport data in terms of the isolated dot spectrum. Knowing the transition rates a master equation can be set up describing the dynamics of the dot states' occupation probabilities. Solving this equation for the steady state allows to calculate the non-equilibrium current driven through the system for arbitrary transport voltages.

2.1.1 Model Hamiltonian

The model Hamiltonian used in this work in order to study transport through quantum dots consists of a reservoir part, a part describing the quantum dot,

and a third part providing the tunneling between dot and reservoirs,

$$\hat{H} = \hat{H}_R + \hat{H}_D + \hat{H}_T \tag{2.1}$$

$$\hat{H}_R = \sum_{\boldsymbol{k},r} \epsilon_{\boldsymbol{k}r} a^+_{\boldsymbol{k}r} a_{\boldsymbol{k}r} + e \sum_r V_r \hat{N}_r \tag{2.2}$$

$$\hat{H}_D = \sum_s E_s \hat{P}_{ss} + eV_D \hat{N} \tag{2.3}$$

$$\hat{H}_T = \sum_{\boldsymbol{k},l,r} T^r_{\boldsymbol{k}l} a^+_{\boldsymbol{k}r} c_l + (h.c.). \tag{2.4}$$

Guided by a typical experimental setup where the reservoir leads rapidly broaden into metallic contacts the reservoir electrons are viewed as non-interacting except for an overall self-consistent potential [21]. Thus, the reservoir Hamiltonian (2.2) is described by the single particle term $\sum_{\boldsymbol{k},r} \epsilon_{\boldsymbol{k}r} a^+_{\boldsymbol{k}r} a_{\boldsymbol{k}r}$ where the electron operator $a^{(+)}_{\boldsymbol{k}r}$ annihilates (creates) an electron with wave vector $\boldsymbol{k}$ (in which the electron spin is included) and energy $\epsilon_{\boldsymbol{k}r}$ in reservoir $r \in \{L, R\}$. Physically, applying a transport voltage between source and drain contacts corresponds to accumulating or depleting charge around the central quantum dot region. The resulting different electrostatic potentials V_r in the left and right reservoir lead to an energetic shift of the reservoir states described by the second term in $\hat{H}_R$, with the (negative) electron charge e and the number operator of the reservoir electrons $\hat{N}_r = \sum_{\boldsymbol{k}} a^+_{\boldsymbol{k}r} a_{\boldsymbol{k}r}$.

The quantum dot Hamiltonian (2.3) is assumed to be already solved by the many-particle states $|s\rangle$ with total energy E_s, hence written by means of the corresponding projector $\hat{P}_{ss} = |s\rangle\langle s|$. Since the electronic motion in a quantum dot is confined in all three dimensions the energy spectrum E_s is discrete. Other than atoms, the confining potential of a quantum dot can be controlled by the used material, size, and shape and it turns out that the actual energy spectrum strongly depends on those parameters [2]. Nevertheless for the following considerations it is enough to keep in mind the discrete nature of the energy levels in quantum dots. The second term in H_D is due to the electrostatic coupling of additional gate electrodes which is assumed to be described by a constant potential V_D with the dot number operator $\hat{N} = \sum_l c^+_l c_l$. The dot electron operator $c^{(+)}_l$ annihilates (creates) a dot electron in the single particle state $|l\rangle$ (in l the electron spin is included). In case there is a considerable electrostatic potential drop across the quantum dot due to the applied transport voltage the electronic structure of the dot can be affected in a non-trivial way which cannot be described by a simple energy shift as for the case of constant potentials. To describe such effects the quantum dot states $|s\rangle$ need to be calculated as a function of the potential drop across the quantum dot.

The tunneling Hamiltonian (2.4) with the tunneling matrix elements $T^r_{\boldsymbol{k}l}$ transfers electrons from the reservoirs to the dot and vice versa [22] where it is assumed that the electron spin is conserved during a tunneling process.

2.1.2 Transition Rates

Considering the tunneling Hamiltonian $\hat{H}_T$ as a perturbation the transition rates between the eigenstates of the isolated quantum dot can be calculated to lowest order by Fermi's Golden Rule (see e.g. [23])

$$\Gamma_{i\to f} = \frac{2\pi}{\hbar}\left|\left\langle f\left|\hat{H}_T\right|i\right\rangle\right|^2 \delta\left(E_i - E_f\right). \tag{2.5}$$

The two states $|i\rangle$, $|f\rangle$ and energies E_i, E_f occurring in this expression belong to the total unperturbed system with the states given by a product of a dot and the two reservoir states $|i\rangle = |s_i\rangle \otimes |\boldsymbol{k}_i^L\rangle \otimes |\boldsymbol{k}_i^R\rangle$. Inserting the tunneling Hamiltonian (2.4) in (2.5) and assuming that the reservoirs are described by grand canonical ensembles it is possible to trace out the reservoir degrees of freedom leading to the sequential tunneling rate

$$\begin{aligned}\Gamma_{s_i\to s_f} &= \frac{2\pi}{\hbar}\sum_{\boldsymbol{k},r} S^r_{\boldsymbol{k},s_i s_f} f^r(\epsilon_{\boldsymbol{k}})\delta\left(E_{s_f} - E_{s_i} - \epsilon_{\boldsymbol{k}} + e(V_D - V_r)\right) \\ &+ \frac{2\pi}{\hbar}\sum_{\boldsymbol{k},r} S^r_{\boldsymbol{k},s_f s_i}(1 - f^r(\epsilon_{\boldsymbol{k}}))\delta\left(E_{s_i} - E_{s_f} - \epsilon_{\boldsymbol{k}} + e(V_D - V_r)\right)\end{aligned} \tag{2.6}$$

between dot state s_i and s_f (see e.g. [5, 24, 25]). In this rate the Fermi function $f^r(\epsilon) = \left(e^{\frac{\epsilon-\mu_r}{kT}} + 1\right)^{-1}$ with the chemical potential μ_r of reservoir r, the temperature T, Bolzmann's constant k, and the spectral weights

$$S^r_{\boldsymbol{k},s_i s_f} = \left|\sum_l T^r_{\boldsymbol{k}l}\langle s_i|c_l|s_f\rangle\right|^2 \tag{2.7}$$

have been introduced. The spectral weights provide transport amplitudes similar to oscillator strengths in optical transitions. For some fixed reservoir index r the first term of Eq. (2.6) describes the tunneling of an electron from the reservoir r into the quantum dot and will be further on denoted as $\Gamma^{r,+}_{s_i\to s_f}$ whereas the second term is a *tunneling out* rate and hence is from now on called $\Gamma^{r,-}_{s_i\to s_f}$. Looking at the tunneling rate (2.6) the following observations can be made: First, due to the annihilator matrix elements occurring in the spectral weights (2.7) only transitions between dot states with electron numbers differing by ± 1 are possible which means that electrons are transported one by one. Second, a transition is only possible if the energy difference between initial and final dot state matches the reservoir electron energy which is expressed by the Dirac δ-functions. For example for the *tunneling out* process described by the second term of (2.6) the energy difference between the initial and final dot state is $E_{s_i} + eV_D - E_{s_f}$. The additional potential energy of a single dot electron eV_D has to be added since in this *tunneling out* rate the initial state has one more electron as compared to the

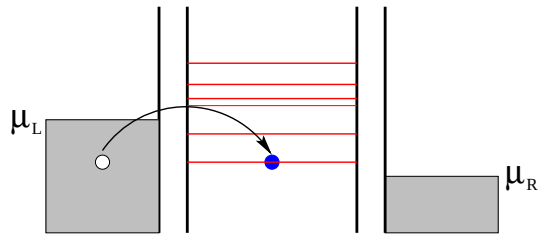

Figure 2.2: Example of a possible transition according to Fermi's Golden Rule shown in a schematic energy profile of the system. On the left and right the Fermi seas of the connecting reservoirs with their electrochemical potentials are shown. A sequential tunneling process is only possible if the energy of the reservoir electron matches the energy difference between initial and final dot state. Those discrete energy differences are drawn as red lines in the quantum dot region and are called transport channels.

final state. Since a single reservoir electron has the energy $\epsilon_{\boldsymbol{k}} + eV_r$ a *tunneling out* process is only possible if $E_{s_i} + eV_D - E_{s_f} = \epsilon_{\boldsymbol{k}} + eV_r$ (compare this expression with the argument of the Dirac δ-function occuring in the second term of (2.6)). Third, a *tunneling in (out)* process is only possible if an occupied (unoccupied) state in the corresponding reservoir is available which is accounted by the Fermi functions. Such a sequential tunneling process is depicted in Fig. 2.2 where the red lines drawn in the central region are the energy differences of the $(\mathcal{N}+1)$ and $\mathcal{N}$-particle state (e.g. $E_{s_i} + eV_D - E_{s_f}$) involved in the transition and are further on called transport channels. In Fig. 2.2 and all following energy profiles shown in this work, the electrochemical potential of the two reservoirs is drawn, i.e., the potential energy eV_r which an electron gains by tunneling through barrier r has been already added to the chemical potential of the corresponding reservoir. Therefore a *tunneling in (out)* process is only possible if the corresponding transport channel lies below (above) the highest (lowest) electrochemical potential. Hence transport channels can be opened or closed by changing the relative position of the electrochemical potentials in the two reservoirs with respect to the channel energies (by changing the potentials V_r and V_D) resulting in a change of the tunneling current. Since the channel energies are directly related to the discrete energy levels in the dot transport can be used as a spectroscopic tool for probing the quantum dot energy levels [14, 15, 16].

The single particle tunneling matrix elements $T^r_{\boldsymbol{kl}}$ occurring in the spectral weights (2.7) have not been specified so far. Apart from the quantum dot and reservoir state they generally depend on the actual shape of the tunneling barrier which is not known for most experimental setups. In the following it is assumed that the absolute value of the tunneling matrix element does only depend on the reservoir index r. The phases of the tunneling matrix elements are assumed to be random with respect to the direction of the reservoir wave vector as described in Appendix A. Replacing the summation in $\boldsymbol{k}$-space of (2.6) by

$\sum_{\boldsymbol{k}} \to \int d\epsilon D(\epsilon)/4\pi \int d\Omega$ with the reservoir density of states $D(\epsilon)$ and following the steps described in Appendix A the sequential transition rates can be written as

$$\begin{aligned}\Gamma^{r,+}_{s_i\to s_f} &= \frac{2\pi}{\hbar} S^r_{s_i s_f} D(E_{s_f} - E_{s_i} + e(V_D - V_r)) \\ &\quad \cdot f^r(E_{s_f} - E_{s_i} + e(V_D - V_r)) \qquad (2.8)\\ \Gamma^{r,-}_{s_i\to s_f} &= \frac{2\pi}{\hbar} S^r_{s_f s_i} D(E_{s_i} - E_{s_f} + e(V_D - V_r)) \\ &\quad \cdot \left[1 - f^r(E_{s_i} - E_{s_f} + e(V_D - V_r))\right] \qquad (2.9)\end{aligned}$$

with the spectral weights

$$S^r_{s_i s_f} = |T^r|^2 \sum_l |\langle s_i|c_l|s_f\rangle|^2. \qquad (2.10)$$

Notice that different to Eq. (2.7) the summation of the single-particle states l in Eq. (2.10) occurs outside the squared absolute value which is a consequence of the random phases of the tunneling matrix elements (see Appendix A).

2.1.3 Tunneling Current and Master Equation

Knowing the *tunneling in* and *tunneling out* rates the non-equilibrium tunneling current through one of the tunneling barriers r is given by

$$I^r(t) = -e \sum_{s,s'} \left[\Gamma^{L+}_{s'\to s} P_{s'}(t) - \Gamma^{L-}_{s\to s'} P_s(t)\right] \qquad (2.11)$$

with $P_s(t)$ being the occupation probability of the quantum dot state $|s\rangle$ at time t [5]. In the steady state the current does not depend on time and as a consequence of charge conservation the current flowing through the left barrier into (out of) the quantum dot is equal to the current flowing out of (into) the dot through the right barrier

$$I^L = I^R = I = -e \sum_{s,s'} \left[\Gamma^{L+}_{s'\to s} P_{s'} - \Gamma^{L-}_{s\to s'} P_s\right]. \qquad (2.12)$$

The steady-state probabilities P_s are determined by the steady-state master equation

$$0 = \frac{d}{dt} P_s = \sum_{s'} \left[\Gamma_{s'\to s} P_{s'} - \Gamma_{s\to s'} P_s\right] = 0 \qquad (2.13)$$

where the probabilities obey the normalization condition $\sum_s P_s = 1$. Notice that the transition rates in (2.13), $\Gamma_{s'\to s} = \sum_r \left(\Gamma^{r,+}_{s'\to s} + \Gamma^{r,-}_{s'\to s}\right)$, are the transition rates (2.6). The first term on the right hand side of (2.13) describes the gain of probability P_s by transitions with final state $|s\rangle$, while the second term describes the loss by transitions out of the initial state $|s\rangle$. In all following investigations only the steady-state current is considered.

2.1.4 Coulomb Blockade

The main difference of the transport properties of quantum dots compared to higher dimensional nanostructures such as quantum wires or wells is that even the introduction of a single electron is sufficient to drastically change the transport properties due to the charging energy associated with this extra electron [7]. Considering only many-particle ground states for a moment, the energy needed to add a further electron to the quantum dot increases with the number of electrons already occupying the quantum dot since the additional electron has to overcome the Coulomb interaction of more and more electrons. Throughout this thesis the transport channel energy which corresponds to the transition between the ith $(\mathcal{N}+1)$-particle state and the jth $\mathcal{N}$-particle state is denoted by $\mu(\mathcal{N}+1,i;\mathcal{N},j) = E_i^{\mathcal{N}+1} - E_j^{\mathcal{N}}$. With the ground state energy $E_0^{\mathcal{N}}$ the ground state-ground state transport channel energy is given by $\mu(\mathcal{N}+1,0;\mathcal{N},0) = E_0^{\mathcal{N}+1} - E_0^{\mathcal{N}}$. This energy increases with increasing number of electrons $\mathcal{N}$

$$\mu(\mathcal{N}+1,0;\mathcal{N},0) > \mu(\mathcal{N},0;\mathcal{N}-1,0) \tag{2.14}$$

as schematically shown in Fig. 2.3. The energy difference between two successive channels, called addition energy, can easily exceed thermal energy kT at experimentally realizable temperatures [7]. Therefore a gap in the electronic structure of the dot can appear at the Fermi energy of the contacts and hence transport through the quantum dot can be blocked. In the situation depicted in Fig. 2.3, where the quantum dot is occupied by $\mathcal{N}$ electrons, no reservoir electron has

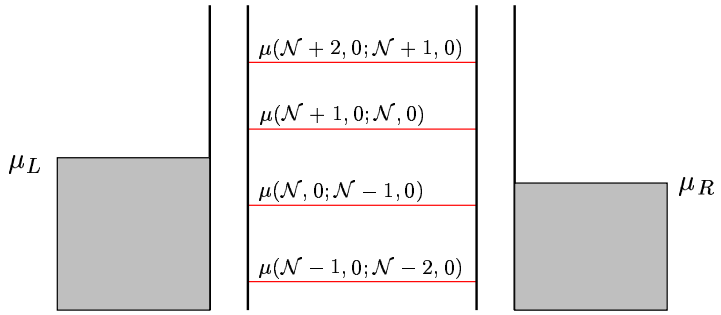

Figure 2.3: Energy profile of a quantum dot in the Coulomb blockade regime. The highest ground state channel below the highest electrochemical potential determines how many electrons occupy the quantum dot. Since no transport channel lies inbetween the left and right electrochemical potential the quantum dot is blocked for transport.

enough energy to charge the quantum dot by another electron since the only possible channel to do so is above both electrochemical potentials. On the other hand no quantum dot electron is able to tunnel out of the dot since the corresponding channel is below both electrochemical potentials such that this transition is

Pauli-blocked. Therefore the quantum dot of Fig. 2.3 is blocked for transport and the number of electrons in the quantum dot is fixed. As the reason for this blocking is the Coulomb interaction together with the quantization of charge this effect is called Coulomb blockade.

2.1.5 Charging Diagram

Due to the previous discussion of the sequential tunneling rates it is clear that the tunneling current is expected to change whenever a transport channel with a non-zero tunneling rate becomes resonant with one of the two electrochemical potentials in the contacts. In most transport experiments two parameters are available allowing to change the relative position of the two electrochemical potentials and the transport channels. Applying a transport voltage $V_{SD} = V_L - V_R$ between the contacts one electrochemical potential is raised whereas the other potential is lowered as compared to the transport channels. The ratio between the raising and the lowering depends on the involved barrier capacities [26]. A second parameter arises from applying a voltage V_G to some nearby gate electrode which couples only electrostatically to the quantum dot. This electrostatic coupling allows to change the discrete energy spectrum and in the simplest case leads to a constant shift $e\alpha V_D$ of the energy levels in the quantum dot where α depends on the capacitance of the gate electrode. Therefore, by applying a

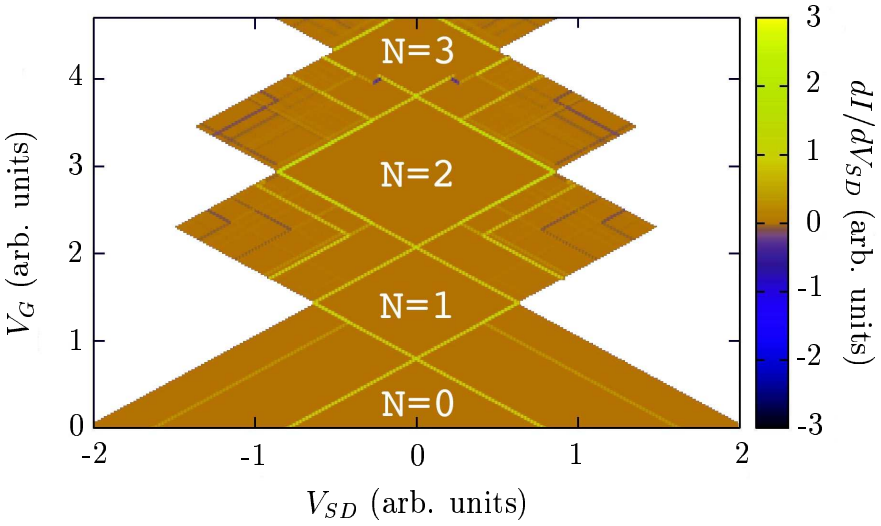

Figure 2.4: Example of a charging diagram calculated for a spherical quantum dot occupied with up to four electrons in the sequential tunneling approximation (all units arbitrarily). The dot is Coulomb blocked in the rhombuses around zero transport voltage V_{SD}. The white area at the right and left border corresponds to higher particle fluctuation not included in this calculation.

gate voltage the transport channels can be shifted with respect to the electrochemical potentials of the two reservoirs. The change of the tunneling current, more precisely the differential conductance dI/dV_{SD}, plotted as function of the transport voltage V_{SD} and gate voltage V_G is commonly called charging diagram [14]. An example of a calculated charging diagram is shown in Fig. 2.4 and in the following the main features found in such diagrams are briefly reviewed. A more complete guideline for their interpretation is given e.g. by WEIS and coworkers [14, 27]. In the central regions of Fig. 2.4 the quantum dot is Coulomb blocked and transport is not possible. The Coulomb blockade (CB) region is limited by resonance lines corresponding to transitions between ground states. At those lines the electrochemical potential of either source or drain is in resonance with a ground state channel. For higher transport voltages the CB-regime is followed by the single electron tunneling regime (SET) where dot states with $\mathcal{N}$ and $\mathcal{N}+1$ electrons coexist. In the SET-regime additional resonance lines exist being parallel to the ground state resonances with positive or negative slope. Resonance lines with positive slopes correspond to transport channels in resonance with the drain electrochemical potential, which are energetically below the ground state channel. Lines with negative slopes are due to channels aligned with the electrochemical potential of the source reservoir, having higher energies than the ground state channel. Resonances in the SET-regime starting at the border of the CB-regime correspond to transitions between a ground state and some excited state whereas channels corresponding to transitions between two excited states lead to resonance lines starting within the SET-regime.

2.2 Multi-channel Transport at Finite Temperatures

Looking at the sequential tunneling rate (2.6) a tunneling process is only possible if the reservoir energy of the tunneling electron exactly matches the energy of a transport channel. Therefore, at zero temperature the tunneling current suddenly changes whenever one of the electrochemical potentials in the connecting reservoirs is in resonance with a transport channel. For example in a linear transport experiment, i.e., where the current is measured as function of the gate voltage V_G by applying a small constant transport voltage V_{SD}, current can only flow as long as there is a transport channel in between the electrochemical potentials of source and drain reservoir (see Fig. 2.5). Hence a peak in the current is found as function of the gate voltage V_G at the energetic position of the transport channel. It is somehow intuitive that this peak gets broadened at finite temperature due

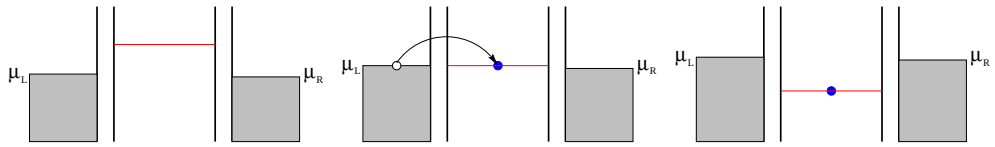

Figure 2.5: **Left:** The electrochemical potentials are below the transport channel so that no transition is possible. **Middle:** Electrochemical potentials are at resonance with the transport channel and current can flow. **Right:** Although the *tunneling in* process is possible the conductance is again zero. The reason is that there are no empty states available in the reservoirs at the channel energy, hence the *tunneling out* process is Pauli-blocked.

to the thermal smearing of the Fermi-distribution with its maximum still at the channel energy. In the following it will be shown that this intuitive picture is in general only true if not more than one channel participates in transport. Whenever more than one channel contributes the position of e.g. the linear transport resonances can be shifted at finite temperatures. This effect is discussed for the case of degenerate quantum dot states for which a transparent analytical solution exists. In that case more than one transport channel exists at a certain energy and consequently more than one channel contributes to the tunneling current.

2.2.1 Degenerate Quantum Dot States

Consider transport through a quantum dot with n transport channels with the same energy. The channels correspond to transitions between an $\mathcal{N}$-particle ground state $|0\rangle$ and one of an n-fold degenerate $(\mathcal{N}+1)$-particle ground states $|i\rangle, i \in \{1, ..., n\}$ with energy difference $E(\mathcal{N}+1) - E(\mathcal{N}) = \epsilon$. For simplicity it is assumed that the many-particle wave-functions are well described by single Slater

determinants leading to simple spectral weights being either 1 or 0. Furthermore it is assumed that the tunneling rates of both barriers are equal, which leads to following transition rates

$$\Gamma_{0\to i} = \Gamma\left[f^s(\epsilon) + f^d(\epsilon)\right] \tag{2.15}$$
$$\Gamma_{i\to 0} = \Gamma\left[2 - f^s(\epsilon) - f^d(\epsilon)\right]. \tag{2.16}$$

For simplicity a constant reservoir density of states has been assumed so that $\Gamma = \frac{2\pi}{\hbar} D|T|^2$ with the tunneling matrix element T. Since the transition rates are independent of the $(\mathcal{N}+1)$-particle states the occupation probability of all $(\mathcal{N}+1)$-particle states are equal so that the normalization condition is $P_i = (1-P_0)/n$. Using this relation the steady-state master equation (2.13) can be solved analytically leading to the steady-state current

$$I = -e\Gamma \frac{n\left(f^s(\epsilon) - f^d(\epsilon)\right)}{2 + (n-1)\left(f^s(\epsilon) + f^d(\epsilon)\right)}. \tag{2.17}$$

Linear Transport

For vanishing transport voltage the conductance G evaluates to

$$G = \left.\frac{dI}{dV_{SD}}\right|_{V_{SD}=0} = -e\Gamma \frac{n\beta\left(f(\epsilon)\right)^2 e^{\beta(\epsilon-\mu)}}{1 + (n-1)f(\epsilon)} \tag{2.18}$$

with $\beta = kT^{-1}$. An interesting and hardly addressed detail is revealed by looking at the maximum of the conductance as a function of the electrochemical potential which is given by

$$\mu^{peak} = \epsilon - \frac{\ln n}{2} kT. \tag{2.19}$$

Hence the peak position does depend on the actual temperature and the degeneracy as shown in Fig. 2.6. Only for zero temperature or for the non-degenerate case ($n = 1$) the peak position is equals to the energy difference between the $\mathcal{N}+1$ and $\mathcal{N}$ particle state. In case of a degenerate transport channel the linear conductance peak shifts to lower energies. This shift as function of temperature is linear with a slope depending logarithmically on the degeneracy. In principle it should therefore be possible to probe the degeneracy by measuring the slope of the temperature dependence of some linear conductance peak position. The reason for this shift is that the occupation of degenerate channels is governed by the fact that only one additional electron can occupy the quantum dot at a time. While *tunneling in* became easier due to the n available transport channels, an electron already in the dot still has only one channel to get out again. Hence, the *tunneling-out* process forms a bottleneck for the tunneling current: to compensate this effect it is possible to enhance the factor $\left(1 - f^d(\epsilon)\right)$ occurring in

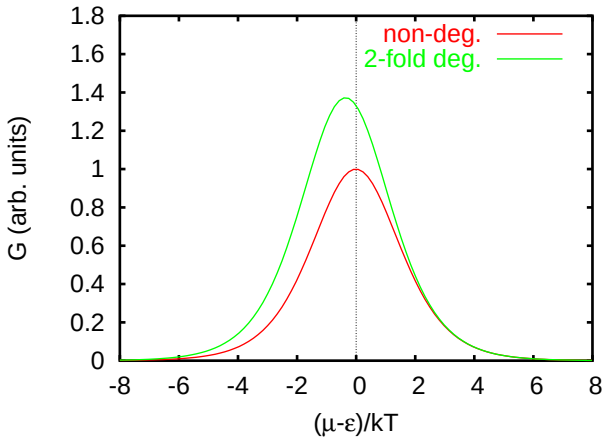

Figure 2.6: Linear conductance G (shown in arbitrary units) as a function of the energy difference between the transport channel energy ϵ and the electrochemical potential of the reservoirs μ through a non-degenerate and two-fold degenerate transport channel at finite temperature. Compared to the non-degenerate case the conductance peak is shifted to lower energies in the degenerate case.

the *tunneling out* rate (2.16) by moving the transport channel slightly above the electrochemical potentials in the reservoirs. Although the *tunneling-in* rate decreases at the same time, the total current is increased. Therefore the maximum current does flow slightly before the electrochemical potentials are in resonance with the transport channel.

Non-linear Transport

In case of non-linear transport, i.e., when the current is measured as a function of the applied transport voltage V_{SD}, degenerate transport channels can also lead to a shift of the corresponding resonance which has been experimentally observed for a 2-fold spin-degenerate localized impurity state in a quantum well region of resonant tunneling diodes by Deshpande et al. [28] and by König [29] and theoretically explained by Bonet et al. [30]. In Fig. 2.7 the current through a non-degenerate and 2-fold degenerate transport channel is shown as a function of the transport voltage for different temperatures. While in the non-degenerate case all current traces cross at half the current step height the crossing occurs above half the step height for the 2-fold degenerate case. In the differential conductance this would lead to a shift of the resonance to lower energies with increasing temperature. In the case of high transport voltages where all drain reservoir states are unoccupied a compact analytical expression for the peak shift

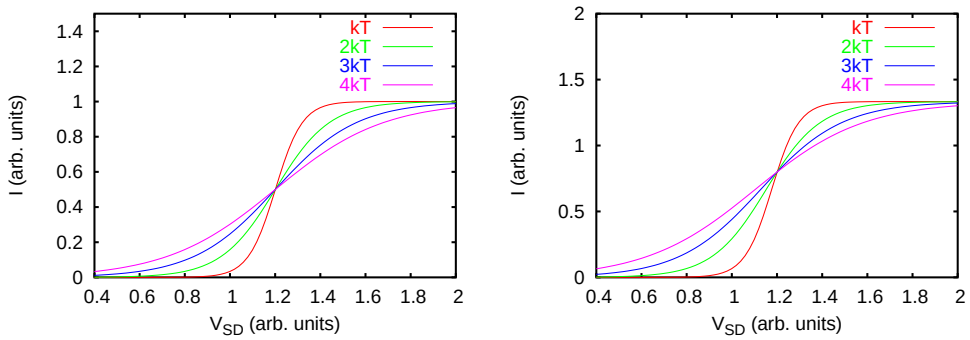

Figure 2.7: Non-linear transport through a non-degenerate (left graph) and 2-fold degenerate (right graph) transport channel for different temperatures (all units are arbitrary). Compared to the non-degenerate case the crossing point of the current traces is shifted above the half step height. In a differential conductance plot this would result in a shift of the resonance to lower energies for increasing temperature.

in the differential conductance exists and reads

$$\mu_s^{peak} = \epsilon - \ln\left(\frac{n+1}{2}\right) kT. \tag{2.20}$$

2.3 Correlation Effects and Spectral Weights

In this section the influence of correlations in the QD states on transport is discussed. Such correlations can change the spectral weights (2.10) [17] which govern the amplitude of a transport resonance in a similar way to the oscillator strength in optical transitions. Moreover, they provide selection rules for the availability of certain transport channels. A quite obvious selection rule due to the spectral weights results from spin quantization. Since the incoming (outgoing) electron carries a total spin $S = 1/2$, with the two possible polarizations $S_z = \pm 1/2$, two states $|s\rangle$ and $|s'\rangle$ involved in a transitions have to fulfill the spin selection rules

$$S^{s'} = S^s \pm \frac{1}{2} \qquad \text{and} \qquad S_z^{s'} = S_z^s \pm \frac{1}{2}. \tag{2.21}$$

Looking at the matrix elements occurring in the spectral weights (2.10) as the overlap of the product of the $\mathcal{N}$-particle *bra* state and some single particle state l with the $(\mathcal{N}+1)$-particle *ket* state, spectral weights might be interpreted as a measure of how well a single electron fits in the $\mathcal{N}$-particle state to give the $(\mathcal{N}+1)$ state. For the simplest case where the many-particle states can be described by a single Slater determinant, as it is e.g. the case for constant-interaction models, the sum over all those matrix elements is one if the *bra* and *ket* Slater determinants differ by one occupation number. Otherwise the spectral weight is zero.

If the many-particle states are not well described by a single Slater determinant but rather by a superposition of such determinants, i.e., the electrons in the quantum dot are correlated, the spectral weights get modified [17]. It is found that the sum over all matrix elements occurring in the spectral weight (2.10) is generally smaller than one. This can be seen in Fig. 2.8 where the calculated spectral weights of two spherical quantum dots with different relative dielectric constants, hence different interaction strength, are shown. It is found that the biggest spectral weights are generally decreased for the case of strong interactions as compared to the weakly interacting case. On the other hand some very small spectral weights are found for the strongly interacting case which are not present in the situation of weakly interacting electrons. To gain a better understanding of the correlation dependence of the spectral weights it is useful to express the spectral weight (2.10) in terms of single-particle state occupation numbers. This can be achieved by expressing the $\mathcal{N}$-particle *bra* state as a linear combination

$$\langle s| = \sum_{\boldsymbol{j}} a^*_{\boldsymbol{j}} \langle 0| c_{j_{\mathcal{N}_s}} c_{j_{\mathcal{N}_s-1}} \cdots c_{j_1} \tag{2.22}$$

with the summation running over all possible Slater determinants $\boldsymbol{j}$ (where j_i denotes the single-particle orbital i occupied in Slater determinant $\boldsymbol{j}$). Inserting

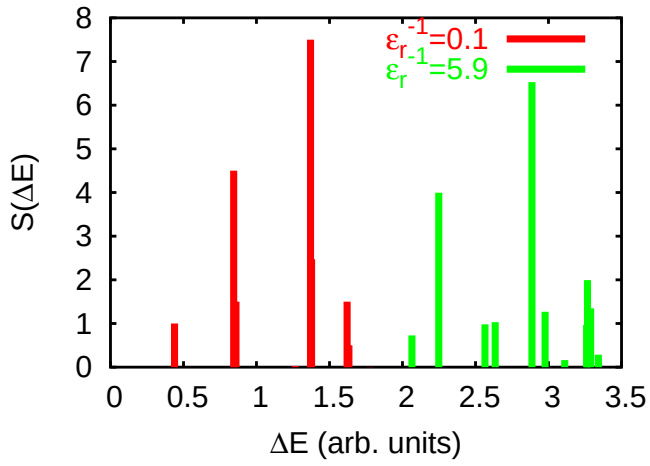

Figure 2.8: Spectral weights of two spherical quantum dot with different relative dielectric constants ϵ_r, hence with two different interaction strengths, as function of the channel energy. The weights between the single-particle ground state and the first 100 2-particle states are shown. For degenerate channel energies the spectral weights are summed up so that weights bigger than one are possible.

this expression into (2.10) leads to

$$S^r_{ss'} = |T^r|^2 \sum_l \left| \sum_{\boldsymbol{j}} a^*_{\boldsymbol{j}} \langle 0 | c_{j_{\mathcal{N}_s}} c_{j_{\mathcal{N}_s-1}} \cdots c_{j_1} c_l | s' \rangle \right|^2 . \tag{2.23}$$

Using the anti-commutator relation $[c_i, c_j]_+ = 0$ the annihilator c_l can be moved to the very left and operate on the vacuum state $\langle 0|$ such that

$$\sum_l \left| \sum_{\boldsymbol{j}} a^*_{\boldsymbol{j}} \langle l | c_{j_{\mathcal{N}_s}} c_{j_{\mathcal{N}_s-1}} \cdots c_{j_1} | s' \rangle \right|^2 \tag{2.24}$$

where the phase factor $(-1)^{\mathcal{N}_s}$ appearing after anti-commuting can be neglected owing to the absolute value. Writing this expression as

$$\sum_l \sum_{\boldsymbol{j},\boldsymbol{k}} a_{\boldsymbol{k}} a^*_{\boldsymbol{j}} \langle s' | c^+_{k_1} c^+_{k_2} \cdots c^+_{k_{\mathcal{N}_s}} | l \rangle \langle l | c_{j_{\mathcal{N}_s}} c_{j_{\mathcal{N}_s-1}} \cdots c_{j_1} | s' \rangle \tag{2.25}$$

the sum over single particle states l can be dropped, since $\sum_l |l\rangle\langle l|$ is the unity operator. Hence expression (2.25) reads

$$\sum_{\boldsymbol{j},\boldsymbol{k}} a_{\boldsymbol{k}} a^*_{\boldsymbol{j}} \langle s' | c^+_{k_1} c^+_{k_2} \cdots c^+_{k_{\mathcal{N}_s}} c_{j_{\mathcal{N}_s}} c_{j_{\mathcal{N}_s-1}} \cdots c_{j_1} | s' \rangle . \tag{2.26}$$

Since every configuration $\boldsymbol{j}$ occurs in expansion (2.22) only once, $\boldsymbol{k}$ has to be equal to $\boldsymbol{j}$ so that the matrix element does not vanish. Next to that the operators can be reordered without sign change such that the corresponding creator and annihilator are next to each other

$$\sum_{\boldsymbol{j}} |a_{\boldsymbol{j}}|^2 \langle s'| c^+_{j_1} c_{j_1} c^+_{j_2} c_{j_2} \cdots c^+_{j_{\mathcal{N}_s}} c_{j_{\mathcal{N}_s}} |s'\rangle. \tag{2.27}$$

By introducing the number operator $\hat{n}_j = c^+_j c_j$ this expression reads

$$S^r_{ss'} = |T^r|^2 \sum_{\boldsymbol{j}} |a_{\boldsymbol{j}}|^2 \langle s'| \prod_{i=1}^{\mathcal{N}_s} \hat{n}_{j_i} |s'\rangle \tag{2.28}$$

When a second electron tunnels into a QD already occupied by one electron this expression is especially simple. The state $|s\rangle$ is a single-particle state so that

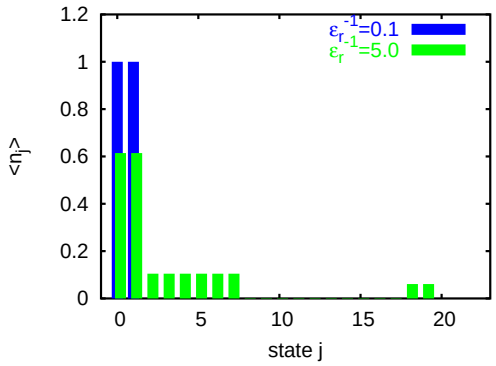

Figure 2.9: Occupation probability of single-particle orbitals ordered by energy for the 2-particle ground states in a spherical quantum dot shown for two different interaction strengths. Strong Coulomb interaction leads to a distribution of the occupation numbers over several single-particle orbitals. The spectral weight of a transition between this 2-particle state and a single-particle states is proportional to the occupation probability of the single-particle state in the shown 2-particle state. For a transition involving the single-particle ground state the spectral weight is proportional to the occupation probability of the state $j = 0$ (first bar to the left) in the 2-particle state which decreases for increasing interaction strength.

(2.22) has only one term with the electron operator c_s. Therefore the spectral weight reads

$$S^r_{ss'} = |T^r|^2 \langle s'| \hat{n}_s |s'\rangle. \tag{2.29}$$

Now suppose the first electron is occupying the single-particle ground state. The spectral weight in the transition rate between this state and the 2-particle ground

state is nothing else but the occupation probability of the single-particle ground state in the two-particle ground state (see Fig. 2.9). For the case of vanishing interaction all occupation numbers are either zero or one, leading to spectral weights of also zero or one. In case of correlations in the quantum dot states the electrons get "distributed" over the single-particle states as can be seen in Fig. 2.9. This leads generally to a suppression of allowed transport channels with increasing correlations.

2.3.1 Ground State Channel Blocking in Non-linear Transport

Prominent correlation effects in transport are for example occurrences of negative differential conductances in the non-linear transport regime [20] or blocking of ground state transitions in linear conductance due to spin selection rules [18, 19]. In the following another mechanism is described leading to a complete disappearance of the ground state-ground state resonance in non-linear transport through a spherical quantum dot. Coulomb interaction within the quantum dot is fully taken into account by the method of exact diagonalization. The detailed discussion of this method and also of the electronic properties of spherical quantum dots is not needed for the following considerations and hence postponed to Chapter 3. As an example the charging diagram of a spherical quantum dot in the 2-3-particle SET-regime is studied (see Fig. 2.10). The two resonance lines intersecting at

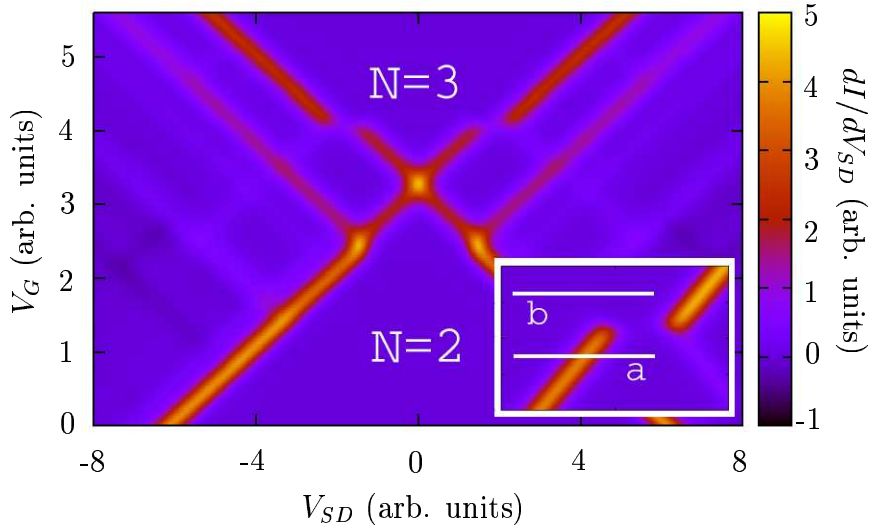

Figure 2.10: Charging diagram for a spherical quantum dot occupied by 2 and 3 electrons shown in arbitrary units. The parameters of the quantum dot are R =100 nm, ξ = 120, ϵ_r =6.67, and m^*/m_e = 0.0239 with Coulomb interaction taken fully into account by an exact diagonalization procedure (for a detailed description of the quantum dot parameter see Chapter 3). **Inset:** Enlarged part of the charging diagram with the vanishing ground state-ground state resonance along e.g. trace b. Below the threshold gate-voltage the ground state-ground state resonance still occurs (e.g. along trace a).

zero transport voltage correspond to the transition between the 2- and 3-particle ground states. Notice that this transition line completely vanishes for gate voltages above a certain threshold (see also trace b in the inset of Fig. 2.10) and transport is only possible at higher source-drain voltages via a different channel

involving an excited state. It turns out that at the voltages applied in the proximity of the vanishing resonance line only two 2-particle states and three 3-particle states are of relevance. The 2-particle ground state with total spin $S = 0$ ($|2, 0\rangle$) and the first excited state with $S = 1$ ($|2, 1\rangle$) on one hand and the 3-particle ground and the first two excited states with $S = 1/2$ ($|3, 0\rangle$), $S = 3/2$ ($|3, 1\rangle$), and $S = 1/2$ ($|3, 2\rangle$) on the other hand. The six possible transport channels de-

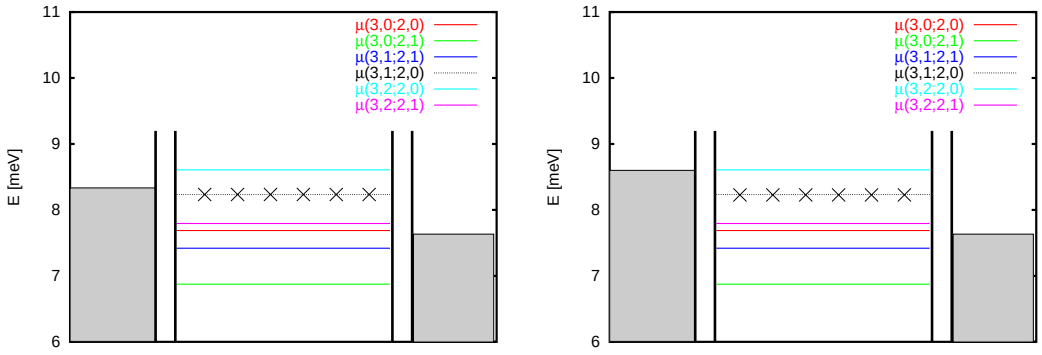

Figure 2.11: **Left:** For a transport window below the threshold gate-voltage (e.g. trace a in Fig. (2.10)) only the ground state-ground state channel $\mu(3, 0; 2, 0)$ can contribute to the current. The channel $\mu(3, 1; 2, 0)$ is spin-blocked and cannot contribute. **Right:** Above the threshold (e.g. trace b in Fig. (2.10)) the top most channel ($\mu(3, 2; 2, 0)$) does participate. From this channel a cascade to the 3-particle first excited state is possible. From this state no open channel is within the transport window and hence the dot is totally blocked for further transport.

noted by $\mu(3, i; 2, j)$ corresponding to the transition between the 3-particle state i and the 2-particle state j are shown in Fig. 2.11. The channel corresponding to the transition between the 2-particle ground state and the 3-particle first excited state, $\mu(3, 1; 2, 0)$, is blocked due to the spin-selection rules. For gate-voltages below the threshold the ground state resonance is observed when the electrochemical potential in the drain reservoir is in resonance with $\mu(3, 0; 2, 0)$. In this situation depicted on the left hand side of Fig. 2.11 only transitions between the ground states are possible. All other channels are either energetically blocked or involve transitions between two excited states. The situation above the threshold is different (right hand side of Fig. 2.11). In this situation a transition cascade is possible which ends in in the first excited state of 3 electrons occupying the dot (see Fig. 2.12). From this state no transition is available allowing an electron to leave the dot. The channel $\mu(3, 1; 2, 1)$ lies energetically below both electrochemical potentials so that this channel is Pauli-blocked. The only other channel $\mu(3, 1; 2, 0)$ containing the first excited 3-particle state is spin-blocked and hence not available. Therefore at such a gate-voltage sooner or later the quantum dot will end up in the first excited 3-particle state which leads to a complete block-

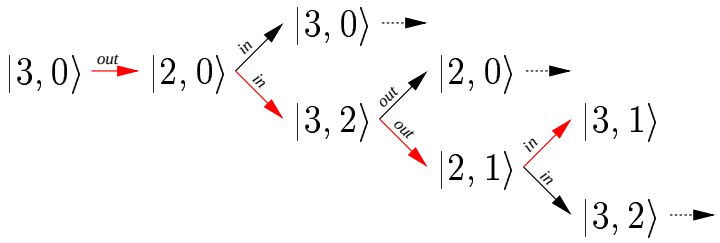

Figure 2.12: All possible transitions starting with the 3-particle ground state for the situation shown on the right hand side of Fig. 2.11. The cascade shown in red ends in the first excited state for 3-particles. From this state only the channel leading to the 2-particle ground state is energetically possible but this channel is blocked due to spin selection rules.

ing of the dot for transport. Paying closer attention to the charging diagram of Fig. 2.10 one might notice that the threshold voltage is below the point where the electrochemical potentials of source and drain become simultaneously resonant with $\mu(3,2;2,0)$ and $\mu(3,0;2,0)$. The reason for this behavior is finite temperature where there is a (small) probability to use the channel $\mu(3,2;2,0)$ already below that resonance. As soon as this channel is used the transition cascade which ends in the first excited 3-particle state, shown in Fig. 2.12, is possible. Whether this transition cascade leads to a blocking depends on how strongly the channel $\mu(3,1;2,1)$ is suppressed compared to the initial transition $\mu(3,2;2,0)$. If it is easier to get in than it is to get out this cascade leads to a blocking. This is the case if, roughly speaking, the source electrochemical potential is closer to channel $\mu(3,2;2,0)$ than the drain potential to the escape channel $\mu(3,1;2,1)$. In the other situation when it is more difficult to enter the cascade than to leave it, no blocking is possible. The threshold occurs roughly where the energetic distance of the entrance channel to the source electrochemical potential is equal to the energetic difference of the escape channel to the drain potential.

A similar blocking mechanism with a spin-blocked transition involved has been found by Weinmann et al. [19, 31] in a two dimensional square-shaped quantum dot. In that work Coulomb interaction in the quantum dot has been treated within the pocket state approximation [32]. Different to the case discussed within this work Weinmann found a transition cascade which ends in a four particle state within the 3-4 single-electron tunneling regime.

Although the spin selection rule connected to the "escape" channel $\mu(3,1;2,0)$ also plays a key role in the here discussed example, the blocking effect still survives if the spectral weight of this "escape" channel is not zero but small. This is true as long as the effective rate to reach the blocking state through the cascade is still much higher than the rate of the "escape" channel. Since channels with small spectral weights are very likely to occur in correlated systems this effect is most probably not restricted to spin-blocked channels. This has been checked

by "artificially" including a non-zero spectral weight for the $\mu(3,1;2,0)$ channel where an effective blocking has still been found for a sufficiently small spectral weight.

Chapter 3

Colloidal Semiconductor Nanocrystals

As discussed in Chapter 2 transport in the weak coupling regime reflects the electronic structure of the isolated quantum dot. In the following the energy levels and wave-functions of a spherical quantum dot is studied in detail. Experimentally spherical quantum dots are realized by colloidal semiconductor nanocrystals. Such nanocrystals are three dimensional structures lying between the molecular and solid-state regime with the unique feature of properties controlled by size and shape. Consisting out of a few hundred up to thousands of atoms their typical sizes range from 2 to 20 nm in diameter. The most reliable and reproducible methods for producing large amounts of uniformly sized semiconductor nanocrystals involve growth in solution from molecular precursor [33]. Next to spherically shaped crystals it recently became possible to fabricate quantum cubes, rods, and quantum wires as long as a few micrometers [34]. Especially rod-shaped nanocrystals recently attracted considerable interest due to their different electronic and optical properties as compared to the spherical crystals [35]. Apart from a fundamental interest in the physics of such mesoscopic structures, nanocrystals are promising candidates for future applications in the field of nanotechnology. Due to the controllable optical and electronic properties possible applications range from light-emitting diodes [36, 37, 38, 39, 40], solar cells [41], and lasers [42, 43], to biological fluorescence marking [44, 45]. Furthermore the large level spacing and the extremely small capacitance of these quantized semiconductor dots make them suitable candidates as active centers in room-temperature single-electron transistors [46]. Even a very small difference of the gate voltage in the order of a tenth of a volt can switch the current from off to on.

To probe the electronic structure of semiconductor nanocrystals, size selective optical techniques, such as photoluminescence excitation spectroscopy (PLE) [47] has been used, mapping the size dependence of dipole-allowed transitions. Another class of experiments is based on tunneling transport yielding complementary information of the electronic structure. While optical spectra show allowed tran-

sitions between valence band (VB) and conduction band (CB) states, tunneling transport allows to separately probe CB and VB states. In addition, spectroscopy of either the single-particle or the few-particle states is possible by controlling the ratio of the drain and source tunneling rates. In case of probing the few-particle states single-electron charging effects are observed in those experiments.

At the beginning of this chapter two transport experiments performed on spherical nanocrystals are reviewed in more detail. The first experiment is the so-called Scanning Tunneling Spectroscopy (STS) which allows to probe the discretized energy levels of the quantum dot. The second experiment allows the direct mapping of the local tunneling density of states of the nanocrystal and is called wave-function mapping. The main part of this chapter is then dedicated to the calculation of the energy spectrum of the isolated quantum dot within a rather simple particle-in-a-sphere model. It will be shown that the STS data can be at least qualitatively understood by the obtained energy levels. To gain, on the other hand, an understanding of the wave-function mapping data one has to take into account the electric field induced by the applied transport voltage leading to a quantum confined Stark effect.

3.1 Transport Experiments

One of the major obstacles in nanometer-scale electron transport through semiconductor nanocrystals is the realization of reliable interfaces between nanocrystals and macroscopic electronic circuits. The many different approaches to address this problem can be broadly divided into two categories, one that employs Scanning Tunneling Microscopy and the other that aims at defining a nanometer-sized tunnel gap through various novel fabrication methods [46, 48]. The latter method has the advantage of improved junction stability and therefore, at least in theory, can provide better energy resolution. On the other hand STM proves to be a versatile tool for fundamental studies of single-electron transport through nanocrystals.

Tunneling transport experiments by means of an STM has been, for example, successfully performed on CdSe [49, 50, 51, 52, 53, 54], CdS [51], InAs [55, 56, 57] and composite core/shell crystals like InAs/ZnSe [58]. The nanocrystals immobilized by some organic linker molecules on a conducting surface [59] can be localized by the STM in topography mode. Afterwards the tip is positioned above the dot, thus forming a tip-dot-substrate double barrier tunnel junction (DBTJ). In a typical experiment the tunneling current is measured as a function of the applied tip-substrate voltage. On top of it STM offers the possibility to tune the properties of the DBTJ by changing the tip-dot distance [52, 57].

In the following two specific Scanning Tunneling Microscopy transport experiments on InAs and InAs/ZnSe nanocrystals are reviewed in greater detail.

3.1.1 Scanning Tunneling Spectroscopy

A sketch of the experimental setup in an STS experiment on colloidal InAs nanocrystal quantum dots is shown in Fig. 3.1. To obtain a tunnel spectrum an STM tip is positioned above a single nanocrystal attached to a gold substrate via hexanedithiol molecules. Keeping the tip-crystal distance constant the differ-

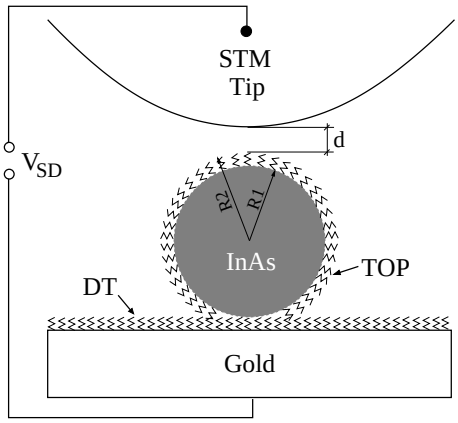

Figure 3.1: Scanning Tunneling Spectroscopy of a single InAs nanocrystal. The InAs nanocrystal with a typical radius of a few nanometers is linked to a gold substrate by 1,6-hexanedithiol molecules (HDT). Trioctylphosphin (TOP) molecules form a ligand shell around the nanocrystal. At 4.2K the tunnel current is measured as a function of the applied voltage V_{SD} between tip and substrate.

ential conductance as a function of applied voltage V_{SD} shows an extended gap around zero transport voltage followed on both sides by a series of sharp peaks (Fig. 3.2) [51, 55, 56]. The strongly asymmetric differential conductance with respect to the gap center indicates strongly different tunneling barriers. In the experiment the STM tip was retracted from the nanocrystal such that the applied transport voltage mainly dropped across the tip-crystal barrier. Therefore the electrochemical potential in the gold substrate stays more or less constant with respect to the transport channels whereas the electrochemical potential in the tip is moved up and done by applying a transport voltage. Assuming that the equilibrium electrochemical potential is somewhere in the nanocrystal's band gap tunneling through CB states becomes possible by rising the electrochemical potential in the STM tip as compared to the transport channels of the nanocrystal. On the other hand lowering the tip potential will eventually allow tunneling through the lower lying VB states. In the STS data shown in Fig. 3.2 the polarization of the transport voltage was chosen such that tunneling through CB states occurs for positive transport voltages. The rest of this chapter will focus on the STS data for positive voltages only and hence on tunneling through CB states. Paying closer attention to the spectra for positive voltages of Fig. 3.2 one can

clearly distinguish between two groups of peaks separated by an extended gap. The first group always consists of two peaks whereas the second group consists of up to six peaks.

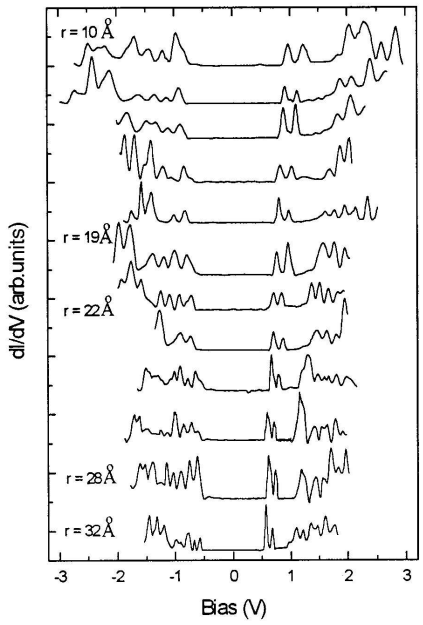

Figure 3.2: Differential conductance of InAs nanocrystals of various radii as a function of the applied tip-substrate voltage measured by MILLO et al. [55]. Due to asymmetric tunneling barriers capacitances the peaks at positive voltages are associated with transport through conduction band states.

3.1.2 Wave-function Mapping

Wave-function mapping in semiconductor quantum dots has recently attracted much interest since it serves as the ultimate tool to study the electronic structure of those dots [60, 61, 62, 63]. Knowing the actual shape of the electronic density of states contributes to a better understanding of the QD's electronic structure. This knowledge is crucial with respect to the possible importance of semiconductor QDs as the ultimate building blocks of optoelectronic and nanoelectronic devices. Next to various experimental techniques available for different dot types, recent STM measurements also allow an imaging of electronic density of states in colloidal nanocrystals [61]. The experimental setup is similar to the STS experiment shown in Fig. 3.1 but the measurement is performed differently. Other than in the STS experiment a topographic image was measured in [61] at a transport voltage above the observed peak structure, $V_{SD} = 2.1$ V (see Fig. 3.3), and simultaneously the tunneling current. At each point along the topography scan the

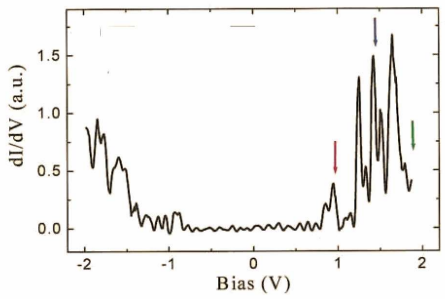

Figure 3.3: Differential conductance as function of the tip-substrate voltage of an InAs/ZnSe core-shell nanocrystal measured by MILLO et al. [61]. The arrows indicate the voltages at which the current was measured in the wave-function mapping experiment (Fig. 3.4).

STM feedback circuit was disconnected momentarily, and the current was measured at three different voltages: $V_{SD} = 0.9$ V, $V_{SD} = 1.4$ V, and $V_{SD} = 1.9$ V as indicated in Fig. 3.4 (Notice that in Fig. 3.4 the transport voltage is labeled as V_B.). Therefore, the topographic and current images are all measured with the same constant local tip-QD separation. The main factor determining the current is thus the local density of state in the quantum dot integrated over the energies within the applied transport window. Interestingly the observed lateral

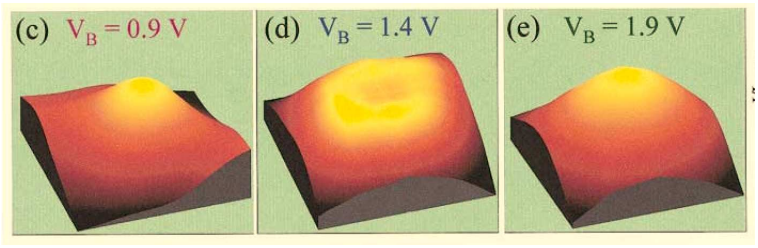

Figure 3.4: Lateral current distribution for three different tip-substrate voltages indicated in the STS data of Fig. 3.3 measured by MILLO et al. [61]. While there is a global maximum in the crystal center for voltages associated with the second and last conductance peak ($V_B = 0.9V$ and $V_B = 1.9V$, respectively) a local minimum occurs for the fifth peak ($V_B = 1.4V$).

current distributions show different symmetries for different transport voltages. While for the lowest and highest voltages a current distribution with a spherical symmetry is found, the symmetry of the $V_{SD} = 1.4$ V is toroidal. In principal the symmetry might be broken due to a geometrical deviation from the spherical shape, but since the exact geometry is not known, in Section 3.3 focus is put on a less speculative reason for the broken symmetry.

3.2 Electronic Quantum Dot States

Theoretical models based on effective mass approximation in various degrees of complexities [64, 65], as well as tight-binding [66, 67] and pseudo-potential calculations [68] have been performed to obtain the discrete CB and VB states. In the early work a simple parabolic band approximation was used [69, 70] which turned out to be a useful approach in order to gain a qualitative understanding. For a quantitative agreement with experimental data non-parabolicity effects of the conduction band have to be taken into account [64, 65, 71]. Such non-parabolic band-structure effects are retained by the multi-band effective mass approximation proposed by PIDGEON & BROWN [72]. CHEPIC and co-workers [71] could show that the non-parabolicity of the conduction band can also be dealt within a single-band approximation by introducing an energy-dependent electron mass [65]. Non-parabolicity strongly effects the electronic structure of narrow gap semiconductors such as InAs [73, 74].

In the following sections the calculation of single and many particle CB states within a single band envelope wave-function approximation is described. It will be shown that this rather simple model, also called particle-in-a-sphere model, is able to qualitatively describe the STS data reviewed in the last section. In order to achieve quantitative agreement with experiments the model is modified by an energy-dependent effective mass accounting for non-parabolicity effects of the conduction band.

3.2.1 Single-particle States

The particle-in-a-sphere model of the CB electrons is a single-band envelope wave-function approximation where the confinement due to the finite crystal size is modeled by a spherical potential well with finite depth [70]. Within this approximation it is assumed that the influence of the quasi periodic atomic background potential can still be captured by an effective electron mass. Considering only a single electron occupying the nanocrystal, Schrödinger's equation for the envelope wave-function of a finite spherical quantum well with radius R_1 reads

$$\left[-\frac{\hbar^2}{2m^*}\nabla^2 + V\Theta(r-R_1)\right]\psi(r,\theta,\phi) = E\psi(r,\theta,\phi). \tag{3.1}$$

Introducing the dimensionless radius $x = r/R_1$ one finds that the only independent parameter is the potential well strength ξ

$$\left[-\nabla_x^2 + \xi\Theta(x-1)\right]\tilde{\psi}(x,\theta,\phi) = \tilde{E}\tilde{\psi}(x,\theta,\phi) \tag{3.2}$$

$$E = \frac{\hbar^2}{2m^*R_1^2}\tilde{E} \tag{3.3}$$

$$\xi = \frac{2m^*R_1^2V}{\hbar^2}. \tag{3.4}$$

Here, the subscript on the nabla-operator indicates that the radial coordinate is replaced by the dimensionless radius x. Owing to the spherical symmetry the solution to this Schrödinger equation separates in spherical coordinates where the angular part is solved by spherical harmonics

$$\tilde{\psi}(x,\theta,\phi) = R_{nl}(x)Y_{lm}(\theta,\phi) \tag{3.5}$$

with the principal quantum number n, the angular momentum quantum numbers l and m. The radial Schrödinger equation is solved by spherical Bessel functions inside the well and by spherical Hankel functions of the first kind outside the well [75]

$$R_{nl}^{(i)}(x) = Aj_l\left(\sqrt{\tilde{E}}\,x\right) \tag{3.6}$$

$$R_{nl}^{(o)}(x) = Bh_l^{(1)}\left(i\sqrt{\xi-\tilde{E}}\,x\right). \tag{3.7}$$

The usual continuity conditions at the potential step lead to a transcendental equation for the bound state energy levels

$$\begin{aligned}\sqrt{\tilde{E}}\,h_l^{(1)}\left(i\sqrt{\xi-\tilde{E}}\right)\left[lj_{l-1}\left(\sqrt{\tilde{E}}\right)-(l+1)j_{l+1}\left(\sqrt{\tilde{E}}\right)\right] = \\ i\sqrt{\xi-\tilde{E}}\,j_l\left(\sqrt{\tilde{E}}\right)\left[lh_{l-1}^{(1)}\left(i\sqrt{\xi-\tilde{E}}\right)-(l+1)h_{l+1}^{(1)}\left(i\sqrt{\xi-\tilde{E}}\right)\right]\end{aligned} \tag{3.8}$$

being solely determined by the dimensionless potential well strength ξ. The dimensionless energies solving the transcendental equation are further on called $\tilde{E}_{nl}(\xi)$ where l is the order of the Bessel- and Hankel function and n enumerates the roots the transcendental equation. The normalized coefficients A and B are also determined by the continuity conditions and evaluate to

$$\begin{aligned}A_{nl}(\xi) = \Bigg[&\int_0^1 \left|j_l\left(\sqrt{\tilde{E}_{nl}}x\right)\right|^2 x^2dx \\ &+ \left|\frac{j_l\left(\sqrt{\tilde{E}_{nl}}\right)}{h_l^{(1)}\left(i\sqrt{\xi-\tilde{E}_{nl}}\right)}\right|^2 \int_1^\infty \left|h_l^{(1)}\left(i\sqrt{\xi-\tilde{E}_{nl}}x\right)\right|^2 x^2dx\Bigg]^{-\frac{1}{2}}\end{aligned} \tag{3.9}$$

$$B_{nl}(\xi) = A_{nl}(\xi)\frac{j_l\left(\sqrt{\tilde{E}_{nl}}\right)}{h_l^{(1)}\left(i\sqrt{\xi-\tilde{E}_{nl}}\right)}. \tag{3.10}$$

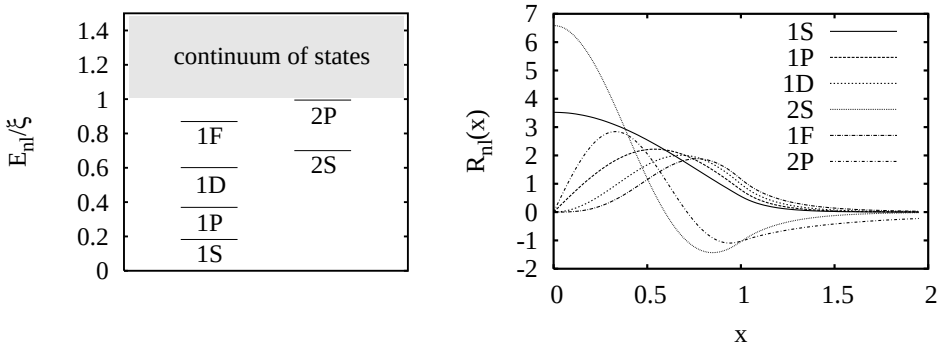

Figure 3.5: On the left hand side the single-particle energy levels for a potential well strength $\xi = 40$ are shown. Due to the finite well depth only a finite number of states are bound followed by a continuum of states. On the right hand side the radial part of the corresponding wave-functions are plotted with the first number of the wave-function label indicating the principal quantum number followed by the angular momentum $S, P, D, ...$ in the notation as used in atomic physics. The wave-function penetration into the potential step at $x = 1$ can be clearly seen.

3.2.2 Energy-dependent Effective Mass

Calculating the single-particle ground state energy for a dot radius of 3.2 nm and using the effective mass of InAs it turns out that such a strong confinement leads to a size quantization comparable to the bulk energy gap of InAs. Hence, for narrow band semi-conductors such as InAs, non-parabolicity effects of the CB have to be taken into account which is done in this work by using an energy-dependent effective mass approach with

$$m^*(E) = m^*(0)[1 + E/E_g] \tag{3.11}$$

where $m^*(0)$ is the bottom CB effective mass and E_g the bulk energy gap [76]. The validity of this approach has been approved by Bryant [77] for a dot radius of 3.2 nm by comparision to a 8 band calculation including CB-VB coupling. Due to the energy-dependent effective mass, Schrödinger's equation has to be

Model	$E_{1P} - E_{1S}$
infinite well	1607 meV
finite well (depth = 3eV)	1044 meV
finite well and energy-dependent mass	319 meV

Table 3.1: Comparison of $1S$-$1P$ excitation for a 3.2 nm InAs nanocrystal obtained by the different models. The experimentally observed energy of about 310 meV [56] compares well with the energy-dependent mass approach.

solved self-consistently until the obtained energy matches the used effective mass.

The $1S$-$1P$ excitation energy using the energy-dependent mass is in good agreement with the experimentally obtained value (see Tab. 3.1). This concept of an energy-dependent mass cannot by generalized to a many-particle Hamiltonian in a straightforward manner. The reason is that the single-particle energy is not longer a meaningful quantity such that a constant effective mass is used for the following few particle calculations.

3.2.3 Few-particle States

In the usual STS experiment the nanocrystals can be charged by more than one electron. Therefore the so far described particle-in-a-sphere model has to be extended to a many-particle model including Coulomb interaction. Written for N electrons the new Hamiltonian reads

$$\hat{H} = \sum_{i=1}^{N} \left(-\frac{\hbar^2 \nabla_{r_i}^2}{2m^*} + V(r_i) \right) + \sum_{i<j} \frac{e^2}{4\pi\epsilon_0 \epsilon_r r_{ij}} \tag{3.12}$$

where the shortcut r_{ij} is introduced for $|\boldsymbol{r}_i - \boldsymbol{r}_j|$ and with ϵ_r being the relative dielectric constant. For convenience this Hamiltonian can be written again in dimensionless quantities

$$\hat{H} = \frac{\hbar^2}{2m^* R_1^2} \left[\sum_{i=1}^{N} \left(-\nabla_{x_i}^2 + \xi\Theta(x_i - 1) \right) + \frac{m^* R_1 e^2}{2\pi\epsilon_0 \epsilon_r \hbar^2} \sum_{i<j} \frac{1}{x_{ij}} \right] \tag{3.13}$$

where the transformation of $\nabla_r^2 = R_1^{-2} \nabla_x^2$ has been used.

Neglecting Coulomb interaction leads to a Schrödinger equation solved by a simple product of N single-particle wave-functions

$$|\varphi_1(\boldsymbol{r}_1)\rangle \otimes |\varphi_2(\boldsymbol{r}_2)\rangle \otimes \cdots \otimes |\varphi_N(\boldsymbol{r}_N)\rangle = |\varphi_1(\boldsymbol{r}_1) \cdots \varphi_N(\boldsymbol{r}_N)\rangle. \tag{3.14}$$

Here the single-particle wave-functions also include the spin degree of freedom and they are therefore called spin-orbitals in the following. Due to the fact that identical particles cannot be distinguished in quantum mechanics, the product state needs to be symmetrized with respect to the particle permutations. Therefore, a many-particle state of a non-interacting system is completely described by the occupied spin-orbitals without any information about which particle occupies which state. In the following such a state of non-interacting particles is called a configuration. A fermionic many-particle state has to be anti-symmetric. Such an anti-symmetric state can be expressed as a so called Slater determinant:

$$|\varphi(\boldsymbol{r_1}, ..., \boldsymbol{r_N})^{(-)}\rangle = \frac{1}{\sqrt{N!}} \begin{vmatrix} |\varphi_1(\boldsymbol{r_1})\rangle & |\varphi_1(\boldsymbol{r_2})\rangle & \cdots & |\varphi_1(\boldsymbol{r_N})\rangle \\ |\varphi_2(\boldsymbol{r_1})\rangle & |\varphi_2(\boldsymbol{r_2})\rangle & \cdots & |\varphi_2(\boldsymbol{r_N})\rangle \\ \cdot & \cdot & \cdot & \cdot \\ \cdot & \cdot & \cdot & \cdot \\ \cdot & \cdot & \cdot & \cdot \\ |\varphi_N(\boldsymbol{r_1})\rangle & |\varphi_N(\boldsymbol{r_2})\rangle & \cdots & |\varphi_N(\boldsymbol{r_N})\rangle \end{vmatrix} \tag{3.15}$$

where φ_i are the single-particle spin-orbitals with the full set of quantum numbers i. In order to distinguish between spin-orbitals and Slater determinants the latter are marked by a minus sign in the superscript $|\varphi^{(-)}\rangle$.

3.2.4 Exact Diagonalization

Since it is possible to expand any wave-function in a complete basis the desired few-electron wave-function describing a system with Coulomb interaction can be written as

$$|\Psi_j(\boldsymbol{r_1}, ..., \boldsymbol{r_N})\rangle = \sum_i a_i^{(j)} |\varphi_i(\boldsymbol{r_1}, ..., \boldsymbol{r_N})^{(-)}\rangle \tag{3.16}$$

where the summation index i stands for a certain configuration. Inserting this expansion in a many-particle Schrödinger equation leads to a matrix eigenvalue equation where the eigenvalues are the desired total energies

$$\sum_i \left\langle \varphi_k^{(-)} \middle| \hat{H} \middle| \varphi_i^{(-)} \right\rangle a_i^{(j)} = E_j \, a_k^{(j)}. \tag{3.17}$$

The eigenvectors $\boldsymbol{a}^{(j)}$ are the expansion coefficients of the searched many-particle wave-function in the occupation number representation. The main task in this approach is to calculate the matrix elements of the many-particle Hamiltonian in the chosen basis and to diagonalize the obtained matrix. Approximations enter this approach due to the computational necessity to keep the basis size limited. One possibility to define a suitable finite basis set is to order the basis states according to their energy, e.g., in the absence of Coulomb interaction, and impose a certain energy cut-off on the basis state. More generally, if $\hat{\mathcal{H}}$ is the Hamiltonian to which the chosen basis states are eigenstates, the ordering of the basis states can be formulated as

$$\hat{\mathcal{H}} |\varphi_i^{(-)}\rangle = \mathcal{E}_i |\varphi_i^{(-)}\rangle \qquad \text{with} \qquad \mathcal{E}_i \leq \mathcal{E}_{i+1}. \tag{3.18}$$

Generally it is assumed that the contribution of a basis state $|\varphi_i^{(-)}\rangle$ decreases for increasing energy such that one can limit the basis size by introducing a cut-off energy. An indication of the accuracy of the calculated many-particle energies using a particular basis can be obtained by successively increasing the cut-off energy and following the change in the obtained low lying energies.

Beyond that the basis size can be strongly reduced by using present symmetries. For example the many-particle Hamiltonian (3.13) is invariant with respect to spatial and spin rotations, i.e., it commutes with the total angular momentum operator and the total spin operator. Therefore the Hamiltonian can be diagonalized in a subspace to given quantum numbers of $\hat{L}_z$, $\hat{L}^2$, $\hat{S}_z$, and $\hat{S}^2$. This can be done easily for $\hat{L}_z$ and $\hat{S}_z$ since the Slater determinants are already eigenstates

to those operators. Different to that the Slater determinants are generally not eigenstates to $\hat{L}^2$ and $\hat{S}^2$ which leads to the necessity to change to the corresponding basis. For the results presented in this work only the $\hat{L}_z$ and $\hat{S}_z$ symmetry was used.

Since the chosen basis already solves the non-interacting Schrödinger equation only the Coulomb operator matrix elements have to be evaluated which is subject of the following section.

3.2.5 Coulomb Matrix Elements

The most convenient way to deal with matrix elements using many particle Slater determinants is to write the operators in second quantization. The reason for this is that the fermionic annihilation or creation operators operating on a Slater determinant lead again to a Slater determinant with one less or one more particle, respectively. A two particle operator, such as Coulomb interaction, reads in second quantization

$$\hat{G} = \sum_{i<j} g(i,j) = \frac{1}{2} \sum_{i,j,k,l} \langle ij|g(1,2)|lk\rangle \, a_i^+ a_j^+ a_k a_l. \tag{3.19}$$

Diagonal Matrix Elements

The diagonal matrix elements of (3.19) in the Slater determinant basis are

$$\left\langle \varphi^{(-)} \right| \hat{G} \left| \varphi^{(-)} \right\rangle = \frac{1}{2} \sum_{i,j,k,l} \langle ij|g(1,2)|lk\rangle \left\langle \varphi^{(-)} \right| a_i^+ a_j^+ a_k a_l \left| \varphi^{(-)} \right\rangle . \tag{3.20}$$

There are two possibilities for the last matrix element on the right hand side of (3.20) to be non-zero, either $(i = k, j = l)$ or $(i = l, j = k)$. Therefore the diagonal matrix elements are

$$\left\langle \varphi^{(-)} \right| \hat{G} \left| \varphi^{(-)} \right\rangle = \frac{1}{2} \sum_{i,j}^{N} \left[\langle ij|g(1,2)|ij\rangle - \langle ij|g(1,2)|ji\rangle \right] . \tag{3.21}$$

The first term is called direct term, the second term has its origin in the anti-symmetric nature of the fermionic many-particle state and is called exchange term.

One different Spin-orbital

If the *bra* and *ket* state differ by one spin-orbital

$$\begin{aligned} \left\langle \varphi^{(-)} \right| \hat{G} \left| \psi^{(-)} \right\rangle &= \frac{1}{2} \sum_{i,j,k,l} \langle ij|g(1,2)|lk\rangle \\ \times \quad {}^{(-)}\langle \varphi_1 \cdots \varphi_u \cdots \varphi | \, a_i^+ a_j^+ a_k a_l \, | \psi_1 \cdots \psi_v \cdots \psi \rangle^{(-)} & \end{aligned} \tag{3.22}$$

with $\varphi_u \notin\{\psi_1, ..., \psi_N\}$ and $\psi_v \notin\{\varphi_1, ..., \varphi_N\}$, there are two cases were the second matrix element on the right is equals 1, $(l = \psi_v, i = \varphi_u, k = j)$ and $(k = \psi_v, j = \varphi_u, i = l)$ and two other cases,$(l = \psi_v, j = \varphi_u, k = i)$ and $(k = \psi_v, i = \varphi_u, j = l)$, were the matrix element is -1. In all other cases the matrix element vanishes. Therefore, the matrix element (3.22) is given by

$$\begin{aligned}\left\langle \varphi^{(-)} \right| \hat{G} \left| \psi^{(-)} \right\rangle &= (-1)^{u+v} \sum_{k\in\{\varphi_{\alpha\neq u}\}}^{N} [\langle k\varphi_u | g(1,2) | k\psi_u \rangle \\ &\quad - \langle k\varphi_u | g(1,2) | \psi_v k \rangle] . \end{aligned} \tag{3.23}$$

Two different Spin-orbitals

If the *bra* and *ket* state differ by two spin-orbitals

$$\left\langle \varphi^{(-)} \right| \hat{G} \left| \psi^{(-)} \right\rangle = \frac{1}{2} \sum_{i,j,k,l} \langle ij | g(1,2) | lk \rangle \tag{3.24}$$

$$^{(-)}\langle \varphi_1 \cdots \varphi_{u_1} \cdots \varphi_{u_2} \cdots \varphi_N | \, a_i^+ a_j^+ a_k a_l \, | \psi_1 \cdots \psi_{v_1} \cdots \psi_{v_2} \cdots \psi_N \rangle^{(-)}$$

with $\varphi_{u_1}, \varphi_{u_2} \notin\{\psi_1, ..., \psi_N\}$ and $\psi_{v_1}, \psi_{v_2} \notin\{\varphi_1, ..., \varphi_N\}$, there are again four possibilities where the matrix element is non zero. For the case where $(l = \psi_{v_1}, k = \psi_{v_2}, i = \varphi_{u_1}, j = \varphi_{u_2})$ or $(l = \psi_{v_2}, k = \psi_{v_1}, i = \varphi_{u_2}, j = \varphi_{u_1})$ the matrix element is $+1$, and where $(l = \psi_{v_1}, k = \psi_{v_2}, i = \varphi_{u_2}, j = \varphi_{u_1})$ or $(l = \psi_{v_2}, k = \psi_{v_1}, i = \varphi_{u_1}, j = \varphi_{u_2})$ the matrix element is -1. This leads to

$$\begin{aligned}\left\langle \varphi^{(-)} \right| \hat{G} \left| \psi^{(-)} \right\rangle &= (-1)^{u_1+u_2+v_1+v_2} (\langle \varphi_{u_1}\varphi_{u_2} | g(1,2) | \psi_{v_1}\psi_{v_2} \rangle \\ &\quad - \langle \varphi_{u_1}\varphi_{u_2} | g(1,2) | \psi_{v_2}\psi_{v_1} \rangle) . \end{aligned} \tag{3.25}$$

Coulomb Matrix Elements

In the system considered the spin-orbitals can be written as a product of spherical harmonics, a radial part, and the spin function

$$\varphi_{nlmm_s}(x, \theta, \phi) = R_{nl}(x) Y_l^m(\theta, \phi) \sigma_{m_s} \tag{3.26}$$

with the spin quantum number m_s. The basic quantity needed, in order to calculate the Coulomb matrix elements, is $\langle ij | 1/x_{12} | kl \rangle$. By expanding the Coulomb operator in spherical harmonics the angular degrees of freedom can be integrate analytically

$$\frac{1}{x_{12}} = \sum_{l=0}^{\infty} \frac{4\pi}{2l+1} \frac{x_<^l}{x_>^{l+1}} \sum_{m=-l}^{l} (-1)^m Y_l^{-m}(\theta_1, \phi_1) Y_l^m(\theta_2, \phi_2) \tag{3.27}$$

with $x_<$ ($x_>$) being the smaller (larger) of x_1 and x_2. Inserting (3.27) into $\langle ij|1/x_{12}|kl\rangle$ leads to

$$\left\langle ij \left| \frac{1}{x_{12}} \right| kl \right\rangle = \delta_{m_{s_i},m_{s_k}} \delta_{m_{s_j},m_{s_l}} \sum_{l=0}^{\infty} \frac{4\pi}{2l+1} \left\langle \tilde{R}_{n_i l_i} \tilde{R}_{n_j l_j} \right| \frac{x_<^l}{x_>^{l+1}} \left| \tilde{R}_{n_k l_k} \tilde{R}_{n_l l_l} \right\rangle \times \sum_{m=-l}^{l} (-1)^m \left\langle Y_{l_i}^{m_i} \right| Y_l^{-m} \left| Y_{l_k}^{m_k} \right\rangle \left\langle Y_{l_j}^{m_j} \right| Y_l^m \left| Y_{l_l}^{m_l} \right\rangle . \quad (3.28)$$

Now the integration over the spherical harmonics can be carried out analytically and yields [78]

$$\left\langle Y_{l_j}^{m_j} \right| Y_l^m \left| Y_{l_l}^{m_l} \right\rangle = \sqrt{\frac{2l+1}{4\pi}} (-1)^{m_j} \times \sqrt{(2l_j+1)(2l_l+1)} \begin{pmatrix} l_j & l & l_l \\ 0 & 0 & 0 \end{pmatrix} \begin{pmatrix} l_j & l & l_l \\ -m_j & m & m_l \end{pmatrix} . \quad (3.29)$$

The arguments of a 3j-symbol have to satisfy $m_1 + m_2 + m_3 = 0$ otherwise the value of the 3j-symbol is zero. This condition is already fulfilled for the first 3j-symbol but requires $m = m_j - m_l$ for the second 3j-symbol. Therefore the last equation can be written as

$$\left\langle Y_{l_j}^{m_j} \right| Y_l^m \left| Y_{l_l}^{m_l} \right\rangle = \delta_{m_j - m_l, m} \left\langle Y_{l_j}^{m_j} \right| Y_l^{m_j - m_l} \left| Y_{l_l}^{m_l} \right\rangle . \quad (3.30)$$

On the other hand this means that the summation over m has at most one non-zero term. Thus this summation can be dropped and all m's can be replaced by $m_j - m_l$ as long as this value is bigger as or equal to $-l$ and smaller as or equal to l. However this condition is anyway fulfilled due to another condition on the arguments of the 3j-symbols: The coefficients have to fulfill $j_i \geq |m_i|$ which means $l \geq |m_j - m_l|$ for the second 3j-symbol. Introducing the coefficients

$$\begin{aligned} c^l(l_l, m_l; l_j, m_j) &= \sqrt{\frac{4\pi}{2l+1}} \left\langle Y_{l_j}^{m_j} \right| Y_l^{m_j - m_l} \left| Y_{l_l}^{m_l} \right\rangle \\ &= (-1)^{m_j} \sqrt{(2l_j+1)(2l_l+1)} \\ &\times \begin{pmatrix} l_j & l & l_l \\ 0 & 0 & 0 \end{pmatrix} \begin{pmatrix} l_j & l & l_l \\ -m_j & m_j - m_l & m_l \end{pmatrix} \end{aligned} \quad (3.31)$$

with the symmetry relation $c^l(l, m; l', m') = (-1)^{m-m'} c^l(l', m'; l, m)$ one can show that

$$\begin{aligned} c^l(l_i, m_i; l_k, m_k) &= (-1)^{m_k - m_i} \sqrt{\frac{4\pi}{2l+1}} \\ &\times \left\langle Y_{l_i}^{m_i} \right| Y_l^{m_i - m_k} \left| Y_{l_k}^{m_k} \right\rangle . \end{aligned} \quad (3.32)$$

The radial integral is called Slater integral and is usually abbreviated by R^l so that the desired matrix element reads

$$\left\langle ij \left| \frac{1}{x_{ij}} \right| kl \right\rangle = \delta_{m_{s_i},m_{s_k}} \delta_{m_{s_j},m_{s_l}} \delta_{m_i+m_j,m_k+m_l} \times \sum_{l=0}^{\infty} c^l(l_i m_i; l_k m_k) c^l(l_l m_l; l_j m_j) R^l(ij;kl). \tag{3.33}$$

The c^l's can be either calculated or found tabulated in SLATER'S book [78]. Fortunately, only few l-values in the last summation occur since the the coefficients $c^l(l,m;l',m')$ can be non-zero only if the triangle relations for both 3j-symbols are fulfilled,

$$l' + l \geq l \quad \Leftrightarrow \quad l \geq l - l' \tag{3.34}$$

$$l + l \geq l' \quad \Leftrightarrow \quad l \geq l' - l \tag{3.35}$$

$$l + l' \geq l \quad \Leftrightarrow \quad l \leq l + l' \tag{3.36}$$

Relation (3.34) and (3.35) can be combined to $l \geq |l - l'|$ and since this relation has to be fulfilled for both c^l's in Eq. (3.33) the only l-values which can lead to non-zero terms are

$$\max(|l_i - l_k|, |l_l - l_j|) \leq l \leq \min(l_i + l_k, l_l + l_j). \tag{3.37}$$

The left over double integral in the radial coordinates

$$\begin{aligned} R^l(ab;cd) &= \int_0^\infty \int_0^\infty \frac{x_<^l}{x_>^{l+1}} x_1^2 x_2^2 \tilde{R}_a^*(x_1) \tilde{R}_b^*(x_2) \tilde{R}_c(x_1) \tilde{R}_d(x_2) dx_1 dx_2 \\ &= \int_0^\infty \tilde{R}_a^*(x) \tilde{R}_c(x) \left[x^{-l+1} \int_0^x y^{l+2} \tilde{R}_b^*(y) \tilde{R}_d(y) dy \right. \\ &\quad \left. + x^{l+2} \int_x^\infty y^{-l+1} \tilde{R}_b^*(y) \tilde{R}_d(y) dy \right] dx \end{aligned} \tag{3.38}$$

has to be calculated numerically.

3.2.6 Shell-tunneling and Shell-filling Spectroscopy

The number of channels contributing to transport generally increases with increasing transport voltage (see Chapter 2). Especially for tip-substrate voltages far beyond the single-electron tunneling regime, where particle fluctuations between zero and up to eight electrons are possible, the number of transport channels will be tremendous. On the other hand how many channels significantly affect the tunneling current depends on the ratio between the tunneling rates through the two barriers. Especially if the tunneling rates differ strongly the number

of important channels can be dramatically reduced [52]. In the so called shell-tunneling regime, where the *tunneling in* rate is much smaller than the *tunneling out* rate ($\Gamma_{in} \ll \Gamma_{out}$), the probability of the nanocrystal being empty is almost unity independent of the applied transport voltage. Therefore only transitions between the unoccupied dot and the various single-particle states, calculated in Section 3.2.1, contribute considerably to the tunneling current. KATZ et al. [57] and also BAKKERS et al. [52, 53] could show that the single-particle spectrum is indeed measured and charging does not occur when the STM tip is retracted from the nanocrystal. Since for positive voltages electrons tunnel from the STM tip to the nanocrystal, a retraction of the tip results in a reduction of the *tunneling in* rate as compared to the *tunneling out* rate.

The opposite regime where $\Gamma_{in} \gg \Gamma_{out}$ is called shell-filling regime. In this regime the probability of finding the maximum possible number of electrons in the dot is almost unity such that signatures of excited states are strongly suppressed [52]. Therefore the few-particle ground state-ground state channels dominate the tunneling current and the corresponding channel energies are discussed in the following section. From the experimental findings obtained by varying the tip-crystal distance it can be concluded that the STS data shown in Fig. 3.2 fall into shell-filling regime.

Charging Energy

An InAs nanocrystal with a radius of about 3 nm is a quantum dot in the strong confinement regime, i.e., the confinement energy dominates as compared to the Coulomb energy. In this regime the first two channels available by applying a transport voltage correspond to ground state-ground state transitions as will be pointed out in the following. Starting with an unoccupied dot at zero transport voltage it is clear that the first channel available for transport belongs to the transition between the empty dot and the single-particle ground state. Denoting the transport channels between the ith excitation of the $(N+1)$-particle state and the jth excitation of the N-particle state by $\mu(N+1, i; N, j)$ this channel is called $\mu(1, 0; 0, 0)$, where the ground state being the 0th excitation. The next possible transport channel available is either the transition between the empty dot state and the first excited state for one electron in the dot ($\mu(1, 1; 0, 0)$) or the ground state-ground state transition between one and two electrons ($\mu(2, 0; 1, 0)$). Since the single-particle ground state is 2-fold degenerate due to the electron spin, the ground state-ground state channel is expected to have the lower energy since the confining energy dominates compared to the Coulomb energy in the strong confinement regime (see Fig. 3.6). Beyond that in the shell-filling regime, where the *tunneling out* process forms a bottleneck for the current, an additional channel which allows a higher particle fluctuation leads to a considerable increase of the tunneling current and therefore to a strong resonance in the differential conductance. Hence the first two differential conductance peaks at positive

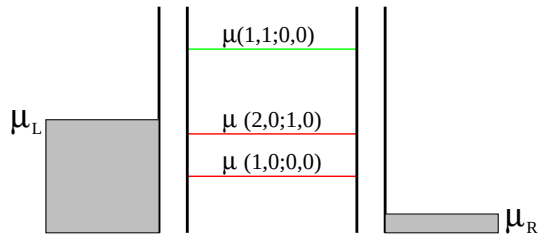

Figure 3.6: The three lowest transport channels available in a 3.2 nm InAs nanocrystal. The first and second transport channel correspond to the first two ground state-ground state transitions.

voltages in Fig. 3.2 correspond to the ground state-ground state transitions between the empty-single and single-double occupied quantum dot, respectively. The energy difference between those peaks is given by the ground states energies $E_0(N=2)-2E_0(N=1)$. Calculating this charging energy for an InAs nanocrystal of radius $R_1 = 3.2$ nm using the bulk dielectric constant $\epsilon_{InAs} = 15.15$ leads approximately 50 meV [1] which is about half the experimentally observed value [56]. There are different possible reasons for the discrepancy between the measured and theoretically obtained charging energy. On one hand the electronic wave-functions leak out of the nanocrystal considerably due to the finite potential well depth (see Fig. 3.5). Outside the nanocrystal the relative dielectric constant is one and hence Coulomb interaction is enhanced. Also the nanocrystal surface becomes polarized due to the electrons already occupying the dot. Hence an entering electron has to pay additional energy by overcoming the interaction with those polarization charges [79]. In order to account for those effects one needs to replace the Coulomb operator by the proper Green's function. On the other hand mirror charges induced in the nearby metallic reservoirs generally lead to a screening of the Coulomb interaction and hence to a reduction of the charging energy [80]. Whether the proper Green's function together with the mirror charges would lead to a better value for the charging energy will be investigated in future work.

Within this work the relative dielectric constant is used as a fitting parameter to compensate for the neglected polarization charge and screening effects. The experimentally observed charging energy of about 100 meV for a 3.2 nm InAs nanocrystal (see Fig. 3.2) is obtained for a relative dielectric constant of about $\epsilon_r = 7.6$.

[1] In this calculation the potential well depth has been chosen to be 5 eV which is approximately the work function of InAs bulk material. The effective mass used is $0.0545 m_e$; this value has been obtained self-consistently for the single-particle ground state using the energy dependent mass (3.11).

Ground State Channels

In Fig. 3.7 the ground state channel energies for up to eight electrons are shown.[2] Qualitatively those transport channels reflect the experimentally observed reso-

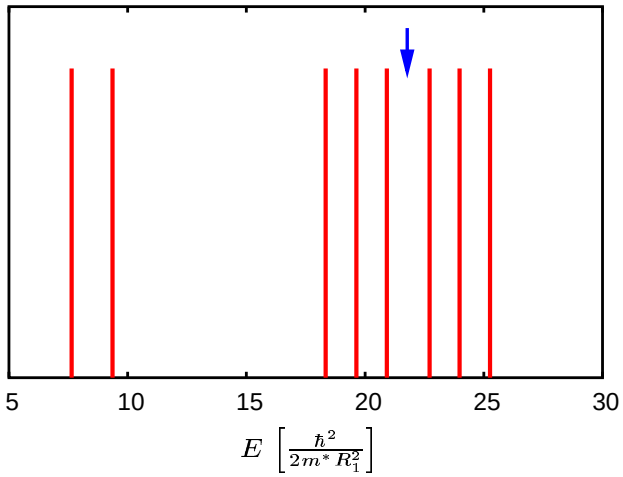

Figure 3.7: Ground state channel energies for up to eight electrons. The quantum dot parameters are $R_1 = 3.2$ nm, $\xi = 56.84$, $m^*/m_e = 0.0705$, and $\epsilon_r = 7.62$. The gap indicated by the arrow is due to Hund's rule slightly enhanced as compared to the other gaps within this group of six transport channels.

nance sequence in the differential conductance shown in Fig. 3.2. The six peaks corresponding to the filling of the 1P-shell fall into two equal peak groups separated by an slightly extended gap (indicated by the arrow in Fig. 3.7). The reason for this gap is that exchange energy is saved by aligning spins following Hund's rule. Notice that Hund's rule cannot be observed in the STS data shown in Fig. 3.2. The reason might be the electric field induced by the tip-substrate voltage. It will be shown in the subsequent sections that such an external field strongly influences the electronic structure.

3.2.7 Excitation Spectra

An interesting effect of the strong confinement regime is related to the excitation energies as a function of the number of electrons occupying the quantum dot. In Fig. 3.8 the lowest excitations conserving the total spin are shown for a

[2]The ground state-ground state channel energies are calculated using the relative dielectric constant of $\epsilon_r = 7.6$, the effective mass $m^*/m_e = 0.0705$ which has been obtained self-consistently for the single-particle 1P-state using the energy-dependent mass (3.11). This effective mass is chosen since at least for the higher particle numbers most electrons occupy the 1P-levels.

spherical quantum dot, where it is found that the lowest excitation energy gener-

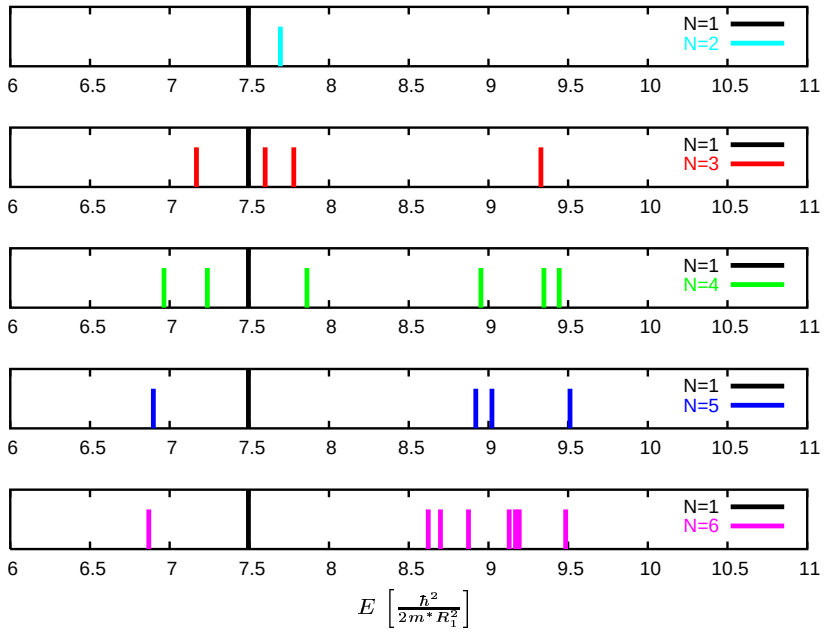

Figure 3.8: Calculated ground state excitation spectra for the low lying excitations in a spherical quantum dot for different number of electrons. Only excitations conserving the total spin are shown which corresponds to the selection rule in the resonant inelastic light scattering experiment performed by Brocke et al. [81, 82]. The parameters of the quantum dot are $\xi = 40$, $R = 10$ nm, $m^* = 0.0293 m_e$, and $\epsilon_r = 8.33$. For increasing number of electrons occupying the quantum dot the lowest excitation is shifted to lower energies.

ally decreases with increasing number of electrons. A qualitative understanding of this excitation energy reduction with increasing number of electrons can be gained by first order perturbation theory in the Coulomb operator $\hat{V}_c$. In the non-degenerate case the first order energy correction is given by

$$E^{(1)} = \left\langle \varphi^{(-)} \right| \hat{V}_c \left| \varphi^{(-)} \right\rangle = \frac{1}{2} \sum_{i,j}^{N} \left[\left\langle ij|\hat{V}_c(1,2)|ij \right\rangle - \left\langle ij|\hat{V}_c(1,2)|ji \right\rangle \right] \qquad (3.39)$$

which is the sum over the Coulomb operator expectation values of all possible anti-symmetric electron pair states. Calculating the energy correction (3.39) of the ground and first excited states for up to 6 electrons in the quantum dot only the matrix elements in Tab. 3.2 occur. Notice that the Coulomb interaction is strongest if both electrons occupy a s-type orbital and generally decreases if one or both electrons occupy a p-type orbital. This can be understood by the larger

Matrix element	opposite spin	parallel spin
$\langle 1S\ 1S\|\hat{V}_c\|1S\ 1S\rangle$	2.0227	-
$\langle 1S\ 1P_m\|\hat{V}_c\|1S\ 1P_m\rangle$	1.8214	1.4202
$\langle 1P_m\ 1P_m\|\hat{V}_c\|1P_m\ 1P_m\rangle$	1.8675	-
$\langle 1P_{\mp 1}\ 1P_{\pm 1}\|\hat{V}_c\|1P_{\mp 1}\ 1P_{\pm 1}\rangle$	1.7468	1.5054
$\langle 1P_0\ 1P_{\pm 1}\|\hat{V}_c\|1P_0\ 1P_{\pm 1}\rangle$	1.6261	1.5054

Table 3.2: Matrix elements of anti-symmetric two-particle states occuring in the first order energy correction of the ground and first excited state of up to 6 electrons. The energies are given in units of $\hbar/2m^*R_1^2$ where the same parameters as in Fig. 3.8 have been used.

spatial extension of the p-orbitals compared to the s-orbitals which is typical for the strong confinement regime [83].

The lowest excitation for up to six electrons is obtained by transferring an s-electron to a p-state. On one hand this excitation cost the energy difference between the single-particle s- and p-state but on the other hand the Coulomb energy between this "transfered" electron and all others gets generally reduced. First of all, the contribution of the two s-electrons to the few-electron ground state is in the excited state replaced by an energetically lower s-p contribution (compare first and second row in Tab. 3.2). Second, all s-p terms contributing to the ground state in which the "transfered" electron is involved are in the excited state replaced by p-p terms which have on average a smaller contribution to the energy (three last rows of Tab. 3.2). While the number s-s interaction terms is one for all ground states between two and six electrons, the number of s-p interaction terms increases with increasing number of electrons. Therefore the number of s-p contribution getting replaced by the energetically lower p-p contributions increases with increasing occupation. This is the reason for the reduction of the lowest excitation energy with increasing number of electrons occupying the quantum dot. Most states shown in Fig. 3.8 are degenerate which requires a diagonalization in the degenerate subspace. This leads to a more complex perturbative analysis which does not lead to further insights.

In principal this reduction of the lowest excitation energy can be observed in the single-electron tunneling regime found in a charging diagram. Unfortunately charging diagrams cannot be obtained using an ordinary STM due to the lack of a gate electrode. Nevertheless the reduction of the lowest excitation energies has been recently measured by Brocke et al. [81, 82] using resonant inelastic light scattering on self-organized InGaAs quantum dots [84, 85]. Although the geometric shape of self-organized quantum dots is not spherical but rather pyramidal the energy reduction of the lowest excitation seems to be a rather general effect of quantum dots in the strong confinement regime. The same effect was

found in the calculated excitation spectra of a two-dimensional quantum dot with harmonic confinement potential [82].

3.3 Quantum Confined Stark Effect

While the experimental data obtained in an STS experiment could be understood by the introduced particle-in-a-sphere model a discrepancy occurs in the interpretation of the wave-function mapping experiment: It was found that tunneling through a p-type orbital can lead to a non-spherical symmetry of the electronic density (Fig. 3.4). The particle-in-a-sphere model introduced reveals completely degenerate $1P$-states due to the spherical symmetry of the confining potential. This implies a spherically symmetric local density of states (LDOS) due to the superposition of degenerate transport channels. Since this was not observed the spherical symmetry was broken in the experiment. In the following section it is shown that the tip-induced electrostatic field results in a lifting of the $1P$ degeneracy in such a way that agreement with experiment is achieved [86, 87].

The quantum confined Stark effect presented in the following sections is calculated for InAs nanocrystals which is in contrast to the wave-function mapping experiment which was performed on InAs/ZnSe core-shell systems. Those compound nanocrystals still obey a spherical symmetry such that the results presented will still hold qualitatively. Quantitatively the electric field strength inside the quantum dot might change due to the different dielectric constants and also the wave-functions will change and energy levels will shift due to the different effective masses and band gaps in InAs and ZnSe.

3.3.1 Tip-induced Electrostatic Field

In the STS setup of Fig. 3.1 with voltages up to $V_{SD} \approx 2$ V [61, 56] applied on a tip-substrate distance of a few nanometers, the nanocrystal is exposed to a considerable electric field. While an STM tip has to terminate in a single atom in order to achieve atomic resolution, the macroscopic tip size is usually about one order in magnitude larger than the nanocrystals studied here [88]. In contrast to a macroscopic metallic tip, a single terminating atom is not able to substantially focus the electric field. Therefore a homogeneous field between tip and substrate is assumed in absence of the QD. Since the considered InAs nanocrystals are surrounded by ligands with a quite different relative dielectric constant compared to InAs, the QD is modeled as a jacketed dielectric sphere (Fig. 3.9). Extending the text book calculation of the electric potential ϕ_{InAs} inside a dielectric sphere placed in a homogeneous field $\mathcal{E}_{hom}$ [89] to such a structure leads (in spherical coordinates) to:

$$\phi_1(r,\theta) = \frac{9\epsilon_2 \mathcal{E}_{hom} r\cos\theta}{2\epsilon_2^2 + \epsilon_1\epsilon_2 + 4\epsilon_2 + 2\epsilon_1 + 2(\frac{R_1}{R_2})^3[\epsilon_1\epsilon_2 + \epsilon_2 - \epsilon_1 - \epsilon_2^2]} \tag{3.40}$$

with $\epsilon_1 = 15.15$ [90] and $\epsilon_2 = 2.1$ [91] being the relative dielectric constants of InAs and the ligands, respectively. R_1 is the InAs core radius and R_2 the

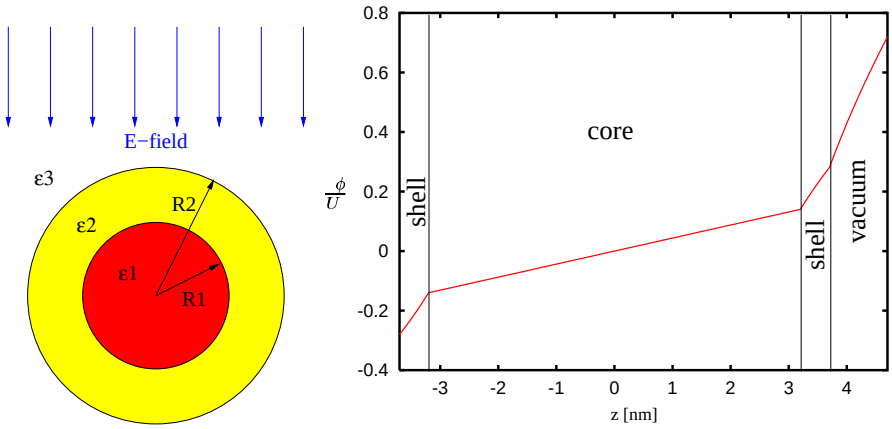

Figure 3.9: **Left:** Sketch of the dielectric core shell sphere exposed to a homogeneous electric field. **Right:** Electrostatic potential through the center of sphere along the field direction calculated for a 3.2 nm InAs nanocrystal.

total radius including the ligand shell (see Fig. 3.1 and 3.9). As in the case of a dielectric sphere without a shell [89] the core potential ϕ_{InAs} is still the potential of a homogeneous field. The field $\mathcal{E}_{hom}$ occurring in (3.40) is not directly accessible. It is obtained by equating the voltage V_{SD} with the potential drop between tip and substrate of the inhomogeneous field outside the QD. Furthermore the knowledge of the total potential drop between tip and substrate also allows for the direct calculation of the lever arm needed to find the actual energies from the measured transport voltages (see right hand side of Fig. 3.9).

3.3.2 Single-particle Calculation

The single-particle Hamiltonian including the tip-induced electrostatic field reads

$$\hat{H} = -\nabla_x^2 + \xi\Theta(x-1) + \frac{2m^* R_1^3 e}{\hbar^2}\,\mathcal{E}\;x\;\cos\theta. \tag{3.41}$$

Since a homogeneous electric field along the z-axis does not destroy the azimuthal symmetry m is still a good quantum number. Mathematically this can be seen most conveniently by expressing the Hamiltonian using the angular momentum operator

$$\hat{H} = \frac{1}{x^2}\left[\frac{\hat{L}^2}{\hbar^2} - \frac{\partial}{\partial x}\left(x^2\frac{\partial}{\partial x}\right)\right] + \xi\Theta(x-1) + \frac{2m^* R_1^3 e}{\hbar^2}\,\mathcal{E}x\cos\theta \tag{3.42}$$

with

$$\hat{L}^2 = -\hbar^2 \left[\frac{1}{\sin\theta} \frac{\partial}{\partial\theta} (\sin\theta \frac{\partial}{\partial\theta}) + \frac{1}{\sin^2\theta} \frac{\partial^2}{\partial\phi^2} \right] \tag{3.43}$$

$$\hat{L}_z = -i\hbar \frac{\partial}{\partial\phi} \tag{3.44}$$

$$\left[\hat{L}^2, \hat{L}_z \right] = 0. \tag{3.45}$$

Starting from this Hamiltonian it can be easily seen that

$$\left[\hat{H}, \hat{L}_z \right] = 0 \qquad \text{and} \qquad \left[\hat{H}, \hat{L}^2 \right] \neq 0 \tag{3.46}$$

where $\hat{L}^2$ does not commute with $\hat{H}$ due to the θ-dependent electrostatic potential.

Matrix Elements

Looking at the matrix elements of the electric field operator in the basis of the single-particle states (3.5) it turns out that the angular degrees of freedom can be again integrated analytically,

$$\begin{aligned} \langle \psi_i | \cos\theta x | \psi_j \rangle \;=\; & \delta_{m_i,m_j} \sqrt{\frac{(2l_i+1)(2l_j+1)(l_i-m_i)!(l_j-m_i)!}{(l_i+m_i)!(l_j+m_i)!}} \\ & \frac{(l_j+m_i)!}{(2l_i+1)(2l_j+1)(l_j-m_i)!} \\ & \left[\delta_{l_i-1,l_j}(l_i+m_i) + \delta_{l_i+1,l_j}(l_i-m_i+1) \right] \\ & \int_0^\infty x^3 \tilde{R}^*_{n_i l_i}(x) \tilde{R}_{n_j l_j}(x) dx. \end{aligned} \tag{3.47}$$

Those matrix elements are non-zero only if $m_i = m_j$ and $|l_i - l_j| = 1$. The remaining radial integration can be calculated numerically without any problems.

Perturbation Theory

Ordinary perturbation theory yields for the energy

$$E \approx E^0_{nlm\sigma} + \sum_{n',l';l'=l\pm1} \frac{|\langle nlm\sigma | \mathcal{E}\, u\, cos\theta | n'l'm\sigma \rangle|^2}{E_{nl} - E_{n'l'}}. \tag{3.48}$$

Notice that the 1st order correction vanishes since the electric field couples only states with $l' = l \pm 1$ (3.47). Hence, in contrast to the hydrogen atom there is no first order Stark effect. The linear Stark effect in hydrogen is caused by the degeneracy between states with different angular momenta (for example the first excited states 2s and 2p). Although the $1S$ state also shows a Stark effect focus is put here on the first excited $1P$ state, with regard to the experimental results obtained by Millo et al. [61].

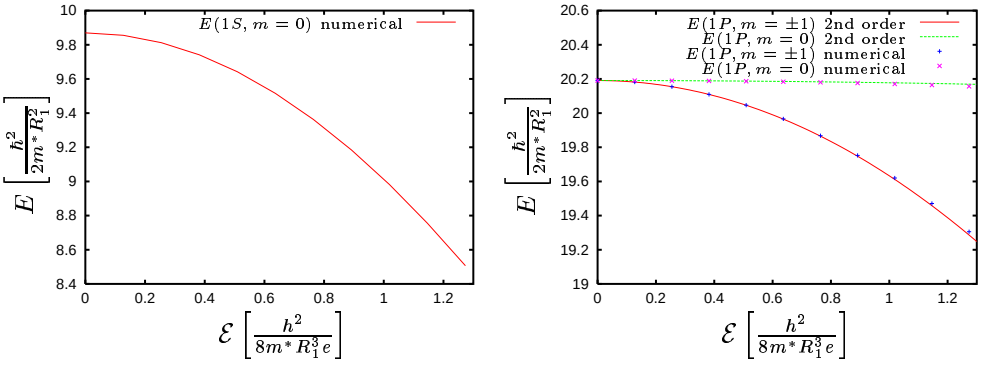

Figure 3.10: Quantum confined Stark effect for the ground (left graph) and first excited $1P$-states (right graph). The Stark effect partly lifts the degeneracy of the $1P$-states. In the right graph the perturbative results calculated for an infinite quantum well are compared to the results of the exact diagonalization.

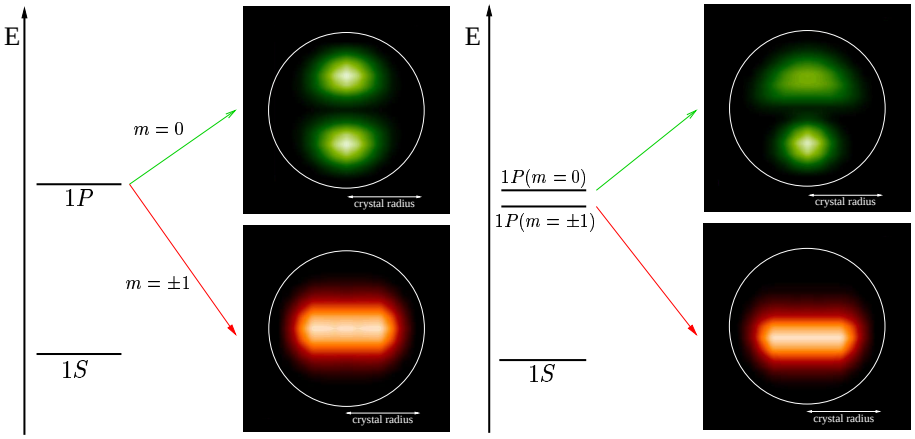

Figure 3.11: Electronic density of the $1P$ envelope wave-functions calculated within a particle-in-a-sphere model. The densities illustrate qualitatively the different Stark effect on the $1P$ state, although they were calculated in an infinite spherical well and neglecting the non-parabolicity of the conduction band. Top and bottom show the $1P(m = 0)$ and $1P(m = \pm 1)$ densities. Without electric field all $1P$-states are degenerate as shown on the left hand side. Applying electric field of 0.18 V/nm the degeneracy is lifted in such a way that the toroidal $1P(m = \pm 1)$ states are energetically lowered (right hand side).

The $1P$ degeneracy is lifted by the quadratic Stark effect (see Fig. 3.10), so that the energy of the $1P(m = \pm 1)$ wave-functions oriented perpendicular to the field (bottom right in Fig. 3.11) are lowered compared to the $1P(m = 0)$ wave-function oriented along the field (top right in Fig. 3.11). This behavior can be qualitatively understood by looking at the electronic densities. In an electric field energy is gained by moving the electronic densities opposite to the field direction. The $1P(m \pm 1)$ densities shown in the bottom row of Fig. 3.11 can move quite freely in that direction with only a small increase in confinement energy. Hence a strong dipole moment is induced leading to a pronounced Stark effect. On the other hand the cost in potential energy for the $1P(m = 0)$ density when moving into the same direction is much higher due to the close confinement potential step. This leads to a smaller induced dipole moment as can be seen in the top row of Fig. 3.11, and therefore to a smaller quadratic Stark effect.

Consequences for the Experiment

Calculating the $1P$-state splitting for a 3.2 nm InAs nanocrystal shows that the degeneracy is lifted by about 15 meV which should be experimentally observable (see Fig. 3.12). Therefore the third and fourth electron entering the nanocrystal

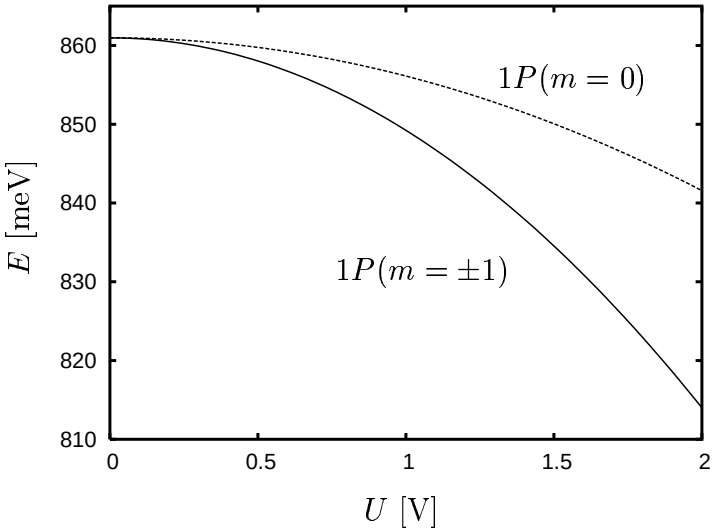

Figure 3.12: Stark splitting of the $1P_e$ level in a 3.2 nm radius InAs nanocrystal as a function of the applied tip-substrate voltage. For calculating the QD potential the ligand shell was taken to be $R_2 - R_1 = 0.5$ nm thick whereas the tip-shell distance was taken as another $d = 0.5$ nm (see Fig. 3.1). 3 eV was used for the depth of the confining potential and to get the energy-dependent mass, the InAs bulk energy gap $E_g = 0.42$ eV [90] and the effective mass $m^*(0)/m_e = 0.0239$ [90] were used.

will occupy the energetically lower $1P(m = \pm 1)$ state with a toroidal symmetry.

The more subtle case of the fifth electron will be discussed in detail in the following section.

3.3.3 Few-particle Calculations: Stark versus Exchange

The many-particle Hamiltonian (3.13) extended by the electric field operator reads

$$\begin{aligned}\hat{H} &= -\sum_{i=1}^{N}\left[\nabla_{x_i}^2 + \xi\Theta(x_i-1) + \frac{2m^*R_1^3 e}{\hbar^2}\,\mathcal{E}\,x_i\,\cos\theta_i\right] \\ &\quad + \frac{m^*R_1 e^2}{2\pi\epsilon_0\epsilon_r\hbar^2}\sum_{i<j}\frac{1}{x_{ij}}. \end{aligned} \tag{3.49}$$

Writing the electric field operator in second quantization

$$H_{\mathcal{E}} = \frac{\hbar^2}{2m^*a^2}\frac{2m^*a^3e\mathcal{E}}{\hbar^2}\sum_{ij}\langle i|\cos\theta x\,|j\rangle\, a_i^+ a_j \tag{3.50}$$

the Slater determinant matrix elements can be calculated similarly as the Coulomb matrix elements. For the diagonal matrix elements one obtains

$$\left\langle\psi^{(-)}\right| H_{\mathcal{E}}\left|\psi^{(-)}\right\rangle = \frac{\hbar^2}{2m^*a^2}\frac{2m^*a^3e\mathcal{E}}{\hbar^2}\sum_{i}\langle i|\cos\theta x\,|i\rangle\,. \tag{3.51}$$

In case the *bra* and *ket* configurations differ by one spin-orbital, the electron operators a_i^+ and a_j occuring in (3.50) have to operate on the corresponding spin-orbital in the *bra* and *ket* configuration, respectively. Otherwise the term is zero due to the orthogonality of the spin-orbitals. If φ_u and ψ_v are the two different spin-orbitals in the *bra* and *ket* state, the matrix elements evaluate to

$$\left\langle\psi^{(-)}\right| H_{\mathcal{E}}\left|\varphi^{(-)}\right\rangle = (-1)^{u+v}\frac{\hbar^2}{2m^*a^2}\frac{2m^*a^3e\mathcal{E}}{\hbar^2}\langle\varphi_u|\,cos\theta x\,|\psi_v\rangle\,. \tag{3.52}$$

Knowing all matrix elements the Hamilton matrix including both Coulomb interaction and the influence of the tip-induced electric field can be calculated and Schrödinger's equation can be again solved by the exact diagonalization procedure.

Five Electrons Ground State

An interesting situation arises for the fifth electron tunneling through the nanocrystal, since a competition between Stark energy on one hand and exchange energy on the other hand arises. Depending on how strong the splitting of the $1P$ states is, two different ground states are possible. For a small splitting the configuration with all three p-type orbitals, $1P(m=\pm1)$ and $1P(m=0)$, occupied each

by one electron with their spins aligned will be favored (see configuration A in Fig. 3.13c). In this configuration the fifth electron has to pay some Stark energy but gains exchange energy. On the other hand if the splitting becomes too big it is energetically more favorable for the fifth electron to occupy also a $1P(m \pm 1)$ state, thereby saving Stark energy. Due to the necessary spin flip, however, it has to pay exchange energy (see configuration B in Fig. 3.13c). This competition between Stark and exchange energy leads to a ground state crossing with increasing electric field strength (see Fig. 3.14). The interesting point is that this crossing

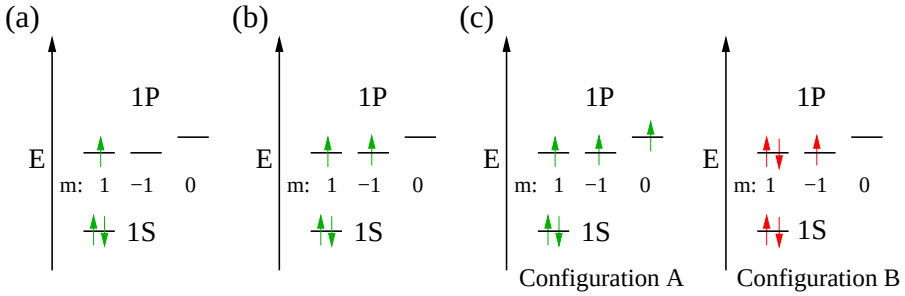

Figure 3.13: (a) Leading ground state configuration for three electrons. (b) Ground state configuration according to Hund's rule for 4 electrons occupying the nanocrystal. (c) Two possible ground state configurations for five electrons.

also corresponds to a change in the LDOS symmetry from spherical to toroidal by increasing the electric field. In contrast to the 3- and 4-electron channel the LDOS symmetry of the 5-electron channel can be controlled by the electric field applied to the nanocrystal.

Unfortunately, the electric field strength applied to the nanocrystal is determined by the resonance condition for tunneling. Therefore, it is experimentally not straightforward to switch the LDOS symmetry forth and back between toroidal and spherical in a wave-function mapping experiment. For a 3.2 nm InAs nanocrystal the 5-electron channel is available at a tip-substrate voltage of about 1.5 V leading to an electric field of about 0.1 V/nm. As indicated by the vertical arrow in Fig. 3.14 the LDOS symmetry of the ground state is still spherical at this field strength. On the other hand the STS peak positions depend on the QD radius such that the question is stressed how the LDOS symmetry of the 5-electron ground state changes with the nanocrystal radius.

In order to answer the question how the ground state symmetry depends on the crystal size the scaling behavior of the Coulomb operator versus the electrostatic potential in (3.49) with respect to the dot radius is studied. Whereas it is clear that the Coulomb operator scales with R_1^{-1} the scaling of the electrostatic potential is not easily foreseen. As shown in Eq. (3.40) the electrostatic potential $\Phi_e \propto \mathcal{E}_{hom}(R_1) \cdot R_1$ scales linearly with the dot radius and electric field strength. This field also depends on the dot size, but in a different way than in a parallel

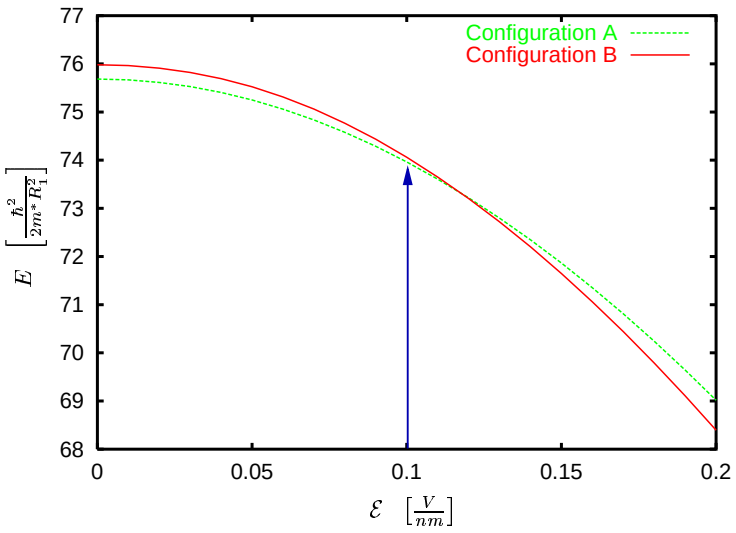

Figure 3.14: Ground and first excited state energies of five electrons versus the electric field strength inside a 3.2 nm radius InAs nanocrystal. The found ground state crossing corresponds to a change in the LDOS symmetry. For a 3.2 nm dot the 5-electron channel is available at a tip-substrate voltage of about 1.5 V leading to an electric field strength indicated by the vertical arrow.

plate capacitor: It scales roughly with $\mathcal{E}_{hom} \propto V_{SD}(R_1) \cdot R_1^{-0.4}$. The reason for this peculiar scaling behavior is mainly caused by the fact that the tip-crystal distance is kept constant while varying the crystal size. Last but not least the applied tip-substrate voltage V_{SD} depends on the energy needed to add a further electron to the crystal which is again a function of the dot radius. In an infinite potential well the single-particle energy levels scale with R_1^{-2} but due to the finiteness of the studied potential well and the fact that the effective mass increases with increasing energy, leads to a scaling of roughly $V_{SD} \propto R_1^{-1}$. Putting all together it is found that the electrostatic potential scales with $\Phi_e \propto R_1^{-0.4}$. Therefore, the LDOS symmetry changes from spherical to toroidal with increasing crystal radius, since Stark energy becomes in bigger crystals more important than exchange energy.

Especially the scaling of the electrostatic potential is not straightforward and therefore it is necessary to check this result by a full calculation. To this end, the charging energy needed to add the fifth electron to the QD has to be calculated in the first step. In the second step the tip-substrate voltage needed to open this 5-electron channel has to be calculated. This voltage is found by multiplying the charging energy by the pre-factor obtained from the electrostatic potential drop along z-direction (see Fig. 3.9). Knowing the applied tip-substrate voltage, the electric field strength in the QD can be calculated by Eq. (3.40) in the last step. Since the charging energy calculated in the first step also depends on the electric

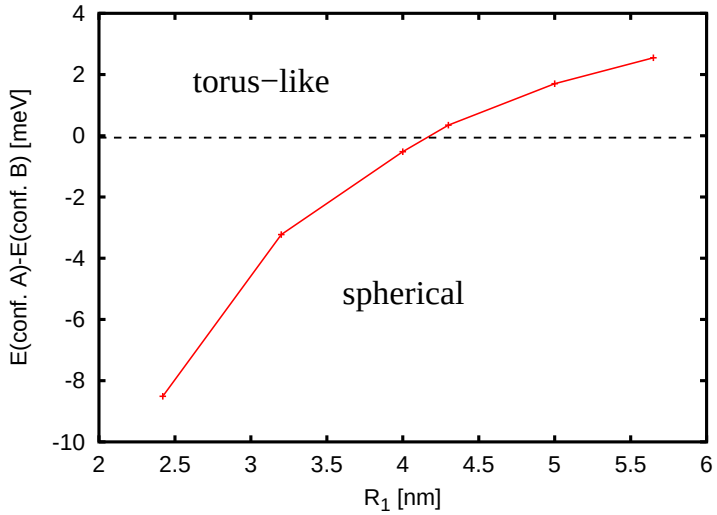

Figure 3.15: The energy difference between the 5-electron ground state and first excited state is shown as a function of nanocrystal radius. For an energy difference greater than zero, configuration B shown in Fig. 3.13c is the new ground state which has a toroidal LDOS symmetry.

field, the whole cycle is repeated until self-consistency is obtained. Now knowing the electric field strength the ground state configuration for the considered QD size and therefore the LDOS symmetry can be determined by going back into Fig. 3.14. This calculation has been done for six InAs crystals with radii between about 2 and 6 nm and the energy difference between configuration A and B versus the dot radius is shown in Fig. 3.15. In this plot a number smaller than zero corresponds to a spherical and a number bigger than zero to a toroidal ground state symmetry. As already predicted by the scaling considerations it is found that the LDOS symmetry changes from spherical to toroidal by increasing the crystal radius. Using the material constants for InAs this transition occurs at a dot radius of about 4 nm. In Fig. 3.16 the electronic density integrated along the z-axis is shown right before and right after the ground state crossing occurs.

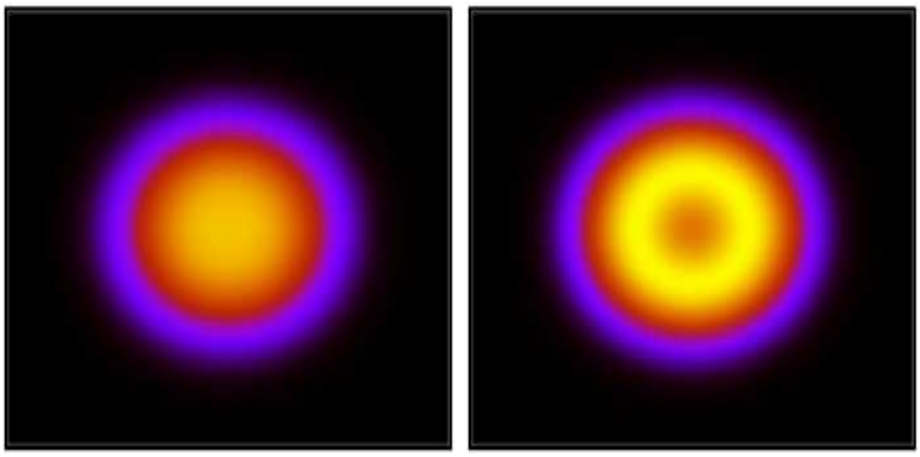

Figure 3.16: Five-particle density integrated along the tip direction for a radius of 4 (left hand side) and 4.3 nm (right hand side), just before and after the crossing, respectively. The qualitative change of the symmetry from spherical to toroidal can be clearly seen.

Chapter 4

Co-tunneling Effects in Charge Transport

According to the results obtained by the master equation approach with transition rates obtained by Fermi's Golden Rule described in Chapter 2, transport through a quantum dot can be understood as sequential processes of single electrons tunneling through either the left or right barrier. This leads for example to the consequence that zero-temperature transport is only possible if one or more transport channels are energetically inbetween the electrochemical potentials of the source and drain reservoir. Otherwise the quantum dot is completely blocked for transport. In contrast to that one might also look at the barrier-dot-barrier structure as a single, more extended, tunneling barrier connecting directly the left and right reservoir. From this point of view one would conclude that in principle tunneling from the left to the right reservoir should be possible for any energy. Although the tunneling rate of such a process is expected to be small due to the extended barrier, it might play a dominant role whenever sequential tunneling is suppressed. And indeed calculating the second order contribution to the Golden Rule rate [5] reveals off-resonant tunneling which is commonly called co-tunneling. It turns out that co-tunneling is the dominant transport process whenever sequential tunneling is suppressed by the Coulomb blockade and leads to a current leakage which might be of importance for single electron devices such as, e.g., the single electron transistor.

It seems to be plausible to treat co-tunneling similar to the sequential case described in Chapter 2 where the tunneling rates, calculated using Fermi's Golden Rule, are used to set up a "classical" master equation. Averin et al. [11, 12] have calculated the co-tunneling rates using Fermi's Golden Rule and found two different co-tunneling processes. In the case of elastic co-tunneling the energies of the initial and final dot state are equal, whereas for inelastic co-tunneling those energies differ. While the Golden Rule approach proved to give good results deep within the Coulomb blockade regime problems occur in the vicinity of the first order resonances [5]. Schoeller et al. [10] were able to derive a formally

exact kinetic equation of the reduced dot density operator for the non-equilibrium situation which can be systematically set up in perturbative orders in the tunnel coupling. They could show that this kinetic equation reveals in lowest order the result of the Fermi's Golden Rule rates together with the master equation reviewed in Chapter 2. Other than that, the next higher order differs from Fermi's Golden Rule in 2nd order which leads especially in the vicinity of the first order resonances to new results [92, 93].

Electron co-tunneling has received considerable attention over the last decade and various experiments have been performed mostly on metallic and large semiconductor quantum dots with essentially continuous excitation energies. Inelastic co-tunneling in normal-metal junctions was first experimentally observed by GEERLIGS et al. [13] and elastic co-tunneling by HANNA et al. [94]. GLATTLI et al. [95, 96] as well as PASQUIER et al. [97, 98] observed co-tunneling within the Coulomb blockade regime in a 2-D electron island formed by a lateral confined 2-D electron gas of a GaAs/GaAlAs heterostructure by means of Schottky gates. An advantage of this kind of devices is the tunability of the tunneling barriers. It allowed the authors to show that the current within the Coulomb blockade regime shows a quadratic dependence on the tunnel barrier conductance indicating a second order process. Non-linear transport measurements deep inside the Coulomb blockade regime revealed a cubic dependence of the tunnel current on the applied voltage which was in agreement with earlier results on metallic dots. A linear current voltage characteristic, existing for higher temperatures was measured in smaller silicon based dots [99, 100] with higher charging energy. Most recently co-tunneling was measured in the strong confinement regime [101], i.e., in dots where the excitation energies are in the order of the charging energy. Transport measurements in such dots, formed from a deep etched rectangular heterostructure, show a clear transition between elastic and inelastic co-tunneling.

In the first part of this chapter the perturbative approach to electron tunneling through quantum dots is reviewed in detail. It is shown how the kinetic equation of the reduced dot density matrix is derived and a systematic perturbative approximation is obtained. After explicitly showing how this formalism leads in lowest order to the Golden Rule results of Chapter 2, the co-tunneling contributions are explicitly discussed. In the second part results of the steady state tunneling current including co-tunneling are presented for an experimentally relevant system [101] of a quantum dot containing two states with finite Coulomb interaction. It is found that in such a system co-tunneling leads to a complex signature of the quantum dot's excitation spectrum even within the Coulomb blockade regime.

4.1 Real-time Transport Theory

In the following section the Real-time Transport Theory (RTT) developed by SCHOELLER et al. [10, 102] is reviewed with respect to the quantum dot system considered in this work. This transport theory is based on a real-time diagrammatic approach which is formulated for the non-equilibrium situation. As in the usual perturbation theory, the basic idea is to integrate out all reservoir degrees of freedom and set up a formally exact kinetic equation for the reduced density matrix of the dot. The kernel of this integro-differential equation can be written as a sum of diagrams and can be calculated in a systematic perturbation expansion in the tunnel coupling. Similar to the calculation of the reduced density matrix any expectation value can be calculated, where the tunneling current is of major interest in this chapter.

4.1.1 Hamiltonian

The Hamiltonian considered is again the Hamiltonian (2.1) of Section 2.1.1. Since the time-evolution operator will play a key role in the subsequent considerations an useful unitary transformation is introduced which allows to write the time-evolution operator in a very compact form. Applying the unitary transformation

$$U(t,t_0) = e^{i\frac{e}{\hbar}\left(\sum_r V_r \hat{N}_r + V_D \hat{N}\right)(t-t_0)} \tag{4.1}$$

to the time-evolution operator of some Hamiltonian $\hat{H}$ leads to

$$U(t,t_0) T_D \left\{ e^{-\frac{i}{\hbar}\hat{H}(t-t')} \right\} U^+(t,t_0) = T_D e^{-\frac{i}{\hbar}\int_{t'}^{t} dt'' \hat{H}(t'')}. \tag{4.2}$$

Here, Dyson's time-ordering operator T_D orders according to the mnemonic rule "later goes to left" without any sign changes. The "new" Hamiltonian $\bar{H}$ appearing in the exponent of the transformed time-evolution operator is given by the transformation $\bar{H} = U^+ H U - i\hbar U^+ \left(\frac{\partial}{\partial t} U\right)$ (see Appendix B). Following the steps of Appendix B.1 this leads for the Hamiltonian (2.1) to

$$\begin{aligned}
\bar{H}(t) &= \bar{H}_R + \bar{H}_R + \bar{H}_T(t) && (4.3)\\
\bar{H}_R &= \sum_{\boldsymbol{k},r} \epsilon_{\boldsymbol{k}r} a^+_{\boldsymbol{k}r} a_{\boldsymbol{k}r} && (4.4)\\
\bar{H}_D &= \sum_{s} E_s \hat{P}_{ss} && (4.5)\\
\bar{H}_T(t) &= \sum_{\boldsymbol{k},l,r} \bar{T}^r_{\boldsymbol{k}l}(t) a^+_{\boldsymbol{k}r} c_l + (h.c.) && (4.6)
\end{aligned}$$

with the transformed tunneling matrix element

$$\bar{T}^r_{\boldsymbol{k}l}(t) = T^r_{\boldsymbol{k}l} e^{-i\frac{e}{\hbar}(V_D - V_r)(t-t_0)}. \tag{4.7}$$

4.1.2 Formalism and Diagrams

Due to the tunnel coupling of the quantum dot to two electronic reservoirs, which are assumed to be each in thermal equilibrium at the same temperature but with different electrochemical potentials, the quantum dot system will be driven out of equilibrium. In order to treat this non-equilibrium problem, the basic idea is to introduce an additional "artifically" time-dependence of the tunnel Hamiltonian in such a way that the coupling does vanish for times $t < t_0$:

$$\begin{aligned} \bar{H}(t) &= \bar{H}_R + \bar{H}_D + \bar{H}_T(t) \\ \Rightarrow \tilde{H}(t) &= \bar{H}_R + \bar{H}_D + \tilde{H}_T(t) \quad \text{and} \quad \tilde{H}_T(t) = 0 \text{ for } t < t_0. \end{aligned} \tag{4.8}$$

Therefore, the total density operator factorizes into a reservoir and a dot part for times prior to t_0

$$\hat{\rho}(t) = \hat{\rho} = \hat{P}_0 \cdot \hat{\rho}_R^{eq} \qquad \text{for} \quad t < t_0 \tag{4.9}$$

with the grand canonical reservoir density operators $\hat{\rho}_r^{eq} = e^{-\beta(\bar{H}_R - \sum_r \mu_r \hat{N}_r)}/Z$ (Z being the product of the partition sums of the left and right reservoir) and the initial dot density operator $\hat{P}_0$. Now, by utilizing the time-evolution operator in the interaction picture $U_I(t,t_0) = T_D e^{-\frac{i}{\hbar}\int_{t_0}^{t} dt' \bar{H}_T^I(t')}$ (see Appendix D) the density operator can be obtained at any time later than t_0

$$\hat{\rho}_I(t) = U_I(t,t_0)\hat{\rho}_I(t_0)U_I^+(t,t_0) \tag{4.10}$$

with the subscript $_I$ indicating that the operators are written in the interaction picture. The main advantage of the time-evolution operator is that this operator can be systematically expanded in orders of the perturbation in a straightforward manner. Knowing the total density operator the quantum statistical expectation value of some operator $\hat{A}(t)$ can be written as

$$\begin{aligned} \langle \hat{A} \rangle(t) &= Tr\left(\hat{\rho}_I(t)\hat{A}_I(t)\right) \\ &= Tr\left(\hat{P}_I(t_0)\hat{\rho}_R^{eq}U_I^+(t,t_0)\hat{A}_I(t)U_I(t,t_0)\right) \end{aligned} \tag{4.11}$$

where the invariance of the trace under even permutations has been used. Choosing t_0 as the point in time where the states in the Schrödinger picture and interaction picture coincide the dot density operator can be written as $\hat{P}_I(t_0) = \hat{P}_0$.

Reduced Density Operator

A similar expression as (4.11) can be derived for the reduced dot density operator $\hat{P}(t) = Tr_R[\hat{\rho}(t)]$ and its matrix elements,

$$P_{ss'}(t) = \langle s | \hat{P}(t) | s' \rangle. \tag{4.12}$$

Here, Tr_R denotes the trace over the reservoir degrees of freedom only. A matrix element of the reduced density operator can be written as

$$\begin{aligned} P_{ss'}(t) &= \langle s\,|Tr_R\left[\hat{\rho}(t)\right]|\,s'\rangle \\ &= \sum_{s_1}\langle s|s_1\rangle\langle s_1|Tr_R\left[\hat{\rho}(t)\right]|s'\rangle \\ &= \sum_{s_1}\langle s_1|Tr_R\left[\hat{\rho}(t)\right]|s'\rangle\langle s|s_1\rangle \\ &= \sum_{s_1}\langle s_1|Tr_R\left[\hat{\rho}(t)\right]\hat{P}_{s's}|s_1\rangle \\ P_{ss'}(t) &= Tr\left[\hat{\rho}(t)\hat{P}_{s's}\right] \end{aligned} \tag{4.13}$$

which means that a matrix element of the reduced density operator is the quantum statistical expectation value of the projector $\hat{P}_{s's}$. Therefore the same mathematical transformations as for the operator $\hat{A}$ can be applied leading to

$$P_{ss'}(t) = Tr\left(\hat{P}_0\hat{\rho}_R^{eq}U_I^+(t,t_0)\hat{P}_{s's}^I(t)U_I(t,t_0)\right). \tag{4.14}$$

For the sake of simplicity, in the following focus will be put on the explicit expression for the reduced density matrix. Anyway, obtaining the corresponding expression for an arbitrary quantum statistical expectation value is straightforward due to the similarity of Eq. (4.11) and (4.14).

Keldysh Contour

Looking at Eq. (4.14) it is found that the trace contains two time-evolution operators

$$\begin{aligned} &U_I^+(t,t_0)\hat{P}_{s's}^I(t)U_I(t,t_0) = \\ &\quad \tilde{T}_D\left\{e^{-\frac{i}{\hbar}\int_t^{t_0}dt'\bar{H}_T^I(t')}\right\}\hat{P}_{s's}^I(t)T_D\left\{e^{-\frac{i}{\hbar}\int_{t_0}^{t}dt'\bar{H}_T^I(t')}\right\} \end{aligned} \tag{4.15}$$

where $\tilde{T}_D$ is the time-ordering operator which orders the other way round as compared to T_D since this operator originates from the adjoint time-evolution operator. For a systematic perturbative expansion it is useful to rewrite this expression such that only one exponential occurs. This can be achieved by introducing the so called Keldysh integration contour and the Keldysh time-ordering operator T_K (see Appendix E) such that

$$U_I^+(t,t_0)\hat{P}_{s's}^I(t)U_I(t,t_0) = \; T_K\left\{e^{-\frac{i}{\hbar}\int_K dt'\bar{H}_T^I(t')}\hat{P}_{s's}^I(t)\right\}. \tag{4.16}$$

The integration contour is an integration forward in time from t_0 to t followed by the corresponding integration backward in time $\int_K = \int_{t_0}^{t} + \int_t^{t_0}$. The Keldysh

time-ordering operator T_K orders in such a way that the operator with the later time along the Keldysh contour appears to the left without any sign change. Returning to (4.14) the reduced density matrix can be written as

$$P_{ss'}(t) = Tr\left(\hat{P}_0\hat{\rho}_R^{eq}T_K\left\{e^{-\frac{i}{\hbar}\int_K dt'\bar{H}_T^I(t')}\hat{P}_{s's}^I(t)\right\}\right) = \sum_{k,\bar{s},k',\bar{s}'}\langle k\bar{s}|\hat{P}_0|k'\bar{s}'\rangle\langle k'\bar{s}'|\hat{\rho}_R^{eq}T_K\left\{e^{-\frac{i}{\hbar}\int_K dt'\bar{H}_T^I(t')}\hat{P}_{s's}^I(t)\right\}|k\bar{s}\rangle \tag{4.17}$$

and with $\langle k\bar{s}|\hat{P}_0|k'\bar{s}'\rangle = \delta_{kk'}P^0_{\bar{s}\bar{s}'}$ this is found to be

$$P_{ss'}(t) = Tr\left(\hat{P}_0\hat{\rho}_R^{eq}T_K\left\{e^{-\frac{i}{\hbar}\int_K dt'\hat{H}_T^I(t')}\hat{P}_{s's}^I(t)\right\}\right) = \sum_{\bar{s},\bar{s}'}P^0_{\bar{s}\bar{s}'}\langle\bar{s}'|Tr_R\left(\hat{\rho}_R^{eq}T_K\left\{e^{-\frac{i}{\hbar}\int_K dt'\bar{H}_T^I(t')}\hat{P}_{s's}^I(t)\right\}\right)|\bar{s}\rangle. \tag{4.18}$$

Expanding the Keldysh ordered time-evolution operator the matrix elements of the reduced dot density operator read

$$P_{ss'}(t) = \sum_{\bar{s}\bar{s}'}P^0_{\bar{s}\bar{s}'}\sum_{m=0}^{\infty}\frac{1}{m!}\left(-\frac{i}{\hbar}\right)^m\int_K dt_1\cdots\int_K dt_m \langle\bar{s}'\left|Tr_R\left(\hat{\rho}_R^{eq}T_K\left[\bar{H}_T^I(t_1)\cdots\bar{H}_T^I(t_m)\hat{P}_{s's}^I(t)\right]\right)\right|\bar{s}\rangle. \tag{4.19}$$

The next task is to insert the explicit tunnel Hamiltonian and to perform the trace over each term in the expansion. As shown in Appendix F the reservoir operator can be separated from all other operators without catching a phase factor,

$$\begin{aligned}&\langle\bar{s}'|Tr_R\left(\hat{\rho}_R^{eq}T_K\left[\bar{H}_T^I(t_1)\cdots\bar{H}_T^I(t_m)\hat{P}_{s's}^I(t)\right]\right)|\bar{s}\rangle = \\ &\sum_{\boldsymbol{k}_1,\boldsymbol{k}_2,\ldots}\sum_{l_1,l_2,\ldots}\sum_{r_1,r_2,\ldots}\bar{T}^{r_1}_{\boldsymbol{k}_1l_1}(t_1)\bar{T}^{*,r_2}_{\boldsymbol{k}_2l_2}(t_2)\cdots \\ &Tr_R\left(\hat{\rho}_R^{eq}T_K\left[a^+_{\boldsymbol{k}_1r_1}(t_1)a_{\boldsymbol{k}_2r_2}(t_2)a^+_{\boldsymbol{k}_3r_2}(t_3)a_{\boldsymbol{k}_4r_4}(t_4)\cdots\right]\right) \\ &\langle\bar{s}'|T_K\left[c_{l_1}(t_1)c^+_{l_2}(t_2)c_{l_3}(t_3)c^+_{l_4}(t_4)\cdots\hat{P}^I_{ss'}(t)\cdots\right]|\bar{s}\rangle \\ &+\textit{all other terms.}\end{aligned} \tag{4.20}$$

All other terms not explicitly written in Eq. (4.20) lead to the same contribution as the first term since it is summed over all indices and integrated over all times t_i. Therefore it is sufficient to treat this first term only and multiply at the end with the number of occuring terms. Since the number of creation and annihilation operators need to be equal in order to get a non-zero trace, the reader might convenience himself that there are altogether $\binom{m}{\frac{m}{2}}$ non-vanishing terms. At this point the first steps towards a diagrammatic language can be introduced. The

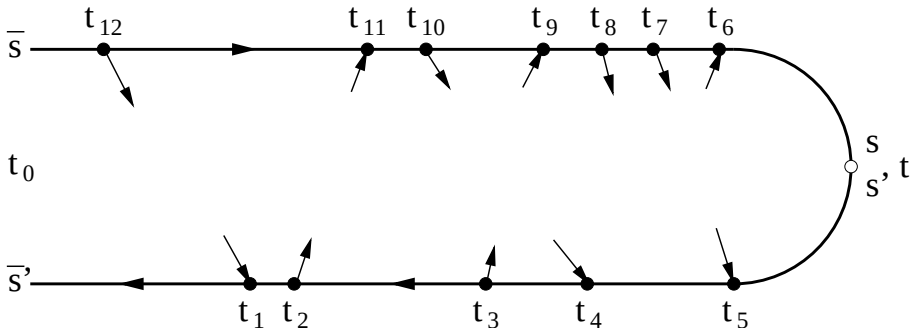

Figure 4.1: The directed line stands for the Keldysh time-integration contour running from t_0 to t and back. At the actual value of each integration variable t_i an internal vertex (black dot) is drawn. Notice that since every time t_i is integrated along the whole Keldysh contour the vertices will eventually occur in any possible order along the contour.

integration along the Keldysh contour is symbolized by a directed time line with internal vertices at the actual integration times t_i (see Fig. 4.1). In case the operator $\hat{A}$ of Eq. (4.11) contains a reservoir electron operator $a^{(+)}_{\boldsymbol{k}r}$, as it is e.g. the case for the current operator, an additional external vertex is drawn at time t. A directed line is attached to each vertex where a incoming line symbolizes an annihilation reservoir operator and an outgoing line a creation reservoir operator at the corresponding vertex time. Since the reservoir Hamiltonian is quadratic in the electron operators Wick's theorem holds and the corresponding operators are contracted in pairs. Due to the fact that the Keldysh time-ordering operator does not induce any sign changes, it can be for the following assumed that the lead operators are already time-ordered without loss of generality. Therefore

$$\begin{aligned} & Tr_R\left(\hat{\rho}_R^{eq} a^+_{\boldsymbol{k}_1 r_1}(t_1) a_{\boldsymbol{k}_2 r_2}(t_2) a^+_{\boldsymbol{k}_3 r_2}(t_3) a_{\boldsymbol{k}_4 r_4}(t_4) \cdots\right) \\ &= a^+_{\boldsymbol{k}_1 r_1}(t_1) a_{\boldsymbol{k}_2 r_2}(t_2) a^+_{\boldsymbol{k}_3 r_2}(t_3) a_{\boldsymbol{k}_4 r_4}(t_4) \cdots \\ &\quad + a^+_{\boldsymbol{k}_1 r_1}(t_1) a_{\boldsymbol{k}_2 r_2}(t_2) a^+_{\boldsymbol{k}_3 r_2}(t_3) a_{\boldsymbol{k}_4 r_4}(t_4) \cdots + \cdots \\ &= \{\text{total pairing}\} \end{aligned} \tag{4.21}$$

where the contractions are given by the equilibrium distribution functions

$$\begin{aligned} a_{\boldsymbol{k}_1 r_1}(t_1) a^+_{\boldsymbol{k}_2 r_2}(t_2) &= Tr_R\left(\hat{\rho}_R^{eq} T_K\left[a_{\boldsymbol{k}_1 r_1}(t_1) a^+_{\boldsymbol{k}_2 r_2}(t_2)\right]\right) \\ &= \delta_{\boldsymbol{k}_1 \boldsymbol{k}_2}\delta_{r_1 r_2} e^{\frac{i}{\hbar}\epsilon(\boldsymbol{k}_1)(t_2 - t_1)}\left[1 - f_{r_1}(\epsilon(\boldsymbol{k}_1))\right] \qquad (4.22) \\ a^+_{\boldsymbol{k}_1 r_1}(t_1) a_{\boldsymbol{k}_2 r_2}(t_2) &= Tr_R\left(\hat{\rho}_R^{eq} T_K\left[a^+_{\boldsymbol{k}_1 r_1}(t_1) a_{\boldsymbol{k}_2 r_2}(t_2)\right]\right) \\ &= \delta_{\boldsymbol{k}_1 \boldsymbol{k}_2}\delta_{r_1 r_2} e^{\frac{i}{\hbar}\epsilon(\boldsymbol{k}_1)(t_1 - t_2)} f_{r_1}(\epsilon(\boldsymbol{k}_1)). \qquad (4.23) \end{aligned}$$

In the diagrammatic language Wick's theorem is realized by connecting pairs of vertices (internal or external) with an outgoing and incoming line attached to it,

respectively, with directed reservoir lines and sum over all $\frac{m!}{2}$ possibilities to do so (see Fig. 4.2). The fact that operators which are contracted need to be next to each other might lead to a phase factor due to the fermionic statistic. In the diagrammatic language a minus sign occurs whenever two reservoir lines cross each other. In such a case one needs an odd number of transpositions to bring those electron operators next to each other, hence collecting a minus sign. For the

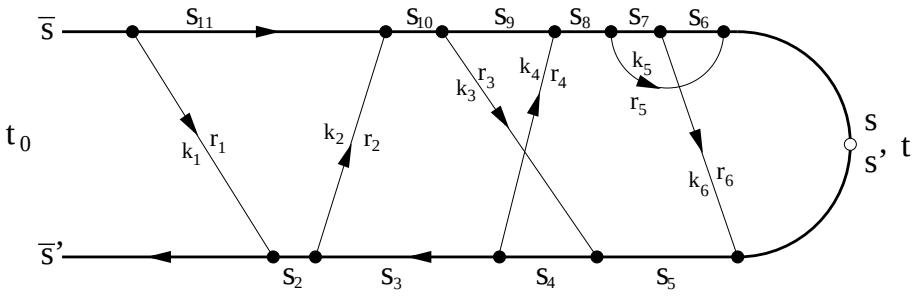

Figure 4.2: Example of the time evolution from time t_0 to t of the reduced density operator. The upper and lower line represent the forward and backward time branch, respectively. The directed lines connecting always two vertices represent tunneling events where the dot state changes.

electrons in the quantum dot Wick's theorem does not hold since the Coulomb interaction is quartic in the dot electron operators. Therefore the product of those operators needs to be treated explicitly. Looking at that part of Eq. (4.20) containing the dot electron operators

$$\langle \bar{s}'|T_K\left[c_{l_1}(t_1)c^+_{l_2}(t_2)c_{l_3}(t_3)c^+_{l_4}(t_4)\cdots \hat{P}^I_{ss'}(t)\cdots\right]|\bar{s}\rangle \tag{4.24}$$

and focusing on some sequence of two dot electron operators following each other due to the Keldysh time ordering it is found

$$\begin{aligned} c^+_{l_2}(t_2)c_{l_3}(t_3) &= U^+_0(t_2,t_0)c^+_{l_2}U_0(t_2,t_0)U^+_0(t_3,t_0)c_{l_3}(t_3)U_0(t_3,t_0) \\ &= \sum_{s_2,s_3,s_4,s_5} U^+_0(t_1,t_0)|s_2\rangle\langle s_2|c^+_{l_2}|s_3\rangle\langle s_3|U_0(t_2,t_3)|s_4\rangle \\ &\quad \times\langle s_4|c_{l_3}|s_5\rangle\langle s_5|U_0(t_3,t_0). \end{aligned} \tag{4.25}$$

The first matrix element on the right hand side of this equation is the spectral amplitude of the transition from the dot state s_3 to s_2 and can be assigned to the vertex at t_2. Similar the last matrix element is the spectral amplitude of the other vertex at t_3. The middle matrix element is simply the free propagation of a dot state between time t_3 and t_2 which can be evaluated to

$$\langle s_3\,|U_0(t_2,t_3)|\,s_4\rangle = \delta_{s_3s_4}e^{-\frac{i}{\hbar}E_{s_3}(t_2-t_3)}. \tag{4.26}$$

In the diagrammatic language this means that a certain dot state $|s_i\rangle$ and the propagator matrix element $\langle s_i|U_0(t_1,t_2)|s_i\rangle$ is assigned to each time segment connecting two vertices. Introducing the shortcuts

$$T^r_{\boldsymbol{k}ss'} = \sum_l T^r_{\boldsymbol{k}l}\langle s\,|c_l|\,s'\rangle \tag{4.27}$$

$$\begin{aligned}\gamma^{r,\pm}_{s_1s_1',s_2s_2'}(t_1,t_2) &= \sum_{\boldsymbol{k}} T^{*,r}_{\boldsymbol{k}s_1's_1}T^r_{\boldsymbol{k}s_2s_2'}e^{-\frac{i}{\hbar}(\epsilon(\boldsymbol{k})+e(V_r-V_D))(t_1-t_2)} \\ &\times\begin{cases} f_r\left(\epsilon(\boldsymbol{k})\right) & \text{for } t_1 <_K t_2, \\ \left[1-f_r\left(\epsilon(\boldsymbol{k})\right)\right] & \text{for } t_1 >_K t_2, \end{cases}\end{aligned} \tag{4.28}$$

the diagrammatic rules can be formulated in a rather compact way. In Eq. (4.28) $-$ corresponds to $t_1 >_K t_2$ and $+$ corresponds to $t_1 <_K t_2$, where the lesser (greater) symbol $<_K$ ($>_K$) along the Keldysh contour has been introduced.

Diagrammatic Rules

To obtain the mth order contribution draw the Keldysh integration contour running form t_0 to t and back and place arbitrarily m vertices onto it. Connect pairs of vertices with directed reservoir lines and assign to each line a wave vector $\boldsymbol{k}_i$ and a reservoir index r_i. To every time segment connecting two vertices assign a quantum dot state s_i and to each vertex a tunneling time t_i.

1. Each occurring reservoir line running from vertex 1 to vertex 2 gives rise to $\gamma^{r,\pm}_{s_2s_2',s_1s_1'}(t_2,t_1)$. r is the index of the reservoir, $+$ corresponds to $t_1 >_K t_2$ and $-$ corresponds to $t_1 <_K t_2$. $s_{1,2}$ ($s'_{1,2}$) are the outgoing (incoming) dot states at each vertex. At vertex 1 where the line starts a particle has to be annihilated on the dot. To each vertex at most one reservoir line can be attached.

2. Each element of the Keldysh contour running from vertex 1 to vertex 2 gives rise to $\langle s_2\,|U_0(t_2,t_1)|\,s_1\rangle$ where s_1 is the outgoing dot state at vertex 1 and s_2 the incoming dot state at vertex 2.

3. The pre-factor is given by $(-1)^c\left(-\frac{i}{\hbar}\right)^m\frac{1}{m!}$ where m is the number of internal vertices and c the number of crossings of fermionic reservoir lines.

Now integrate over all vertices times t_i along the Keldysh contour, sum over all reservoir indices r_i and dot states s_i. The mth-order contribution is than given by the sum over all possible ways to connect $m/2$ pairs of vertices with directed reservoir lines.

4.1.3 Kinetic Equation

Formulating the diagrammatic rules as described in the last sections there are $\binom{m}{\frac{m}{2}}\frac{m}{2}!$ diagrams ($\binom{m}{\frac{m}{2}}$ from the product of the m tunnel Hamiltonians of Eq. (4.20) and $\frac{m}{2}!$ diagrams from the contractions) all leading to the same contribution since it is summed over all indices and integrated over all times t_i. The integration along the Keldysh contour has the disadvantage that the integrands change whenever the time order along the contour changes. From a practical point of view it would be better to find a formulation with diagrams having a unique mathematical expression. This can be achieved by restricting the time-integrals such that the integrands do not change, paying the price of getting a larger total number of diagrams. Looking at the diagrammatic rules one finds that this is achieved by keeping the absolute time ordering, i.e., the time order-

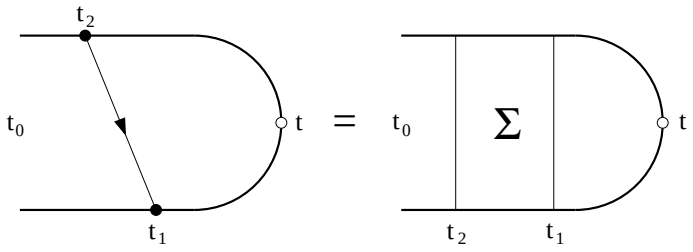

Figure 4.3: The 2nd order diagram in $\bar{H}_T$ written by using a kernel. Where in the left diagram over both times t_1 and t_2 is integrated along the whole Keldysh contour, in the right diagram a more restricted integral, $\int_{t_0}^{t} dt_2 \int_{t_2}^{t} dt_1$, occurs. The price payed for this simplification is a kernel consisting of a larger sum of diagrams.

ing independent of the time branch, of all vertices but leaving each vertex on its corresponding time branch. The restricted time-integration limits are of the form $\int_{t_0}^{t} dt_m \int_{t_m}^{t} dt_{m-1}$.... For the 2nd order the contribution of the diagram shown on the left hand side of Fig. 4.3 is given by the eight 2nd order diagrams shown in Fig. 4.4 with the restricted time integration $\int_{t_0}^{t} dt_2 \int_{t_2}^{t} dt_1$ plus the propagator segments containing no reservoir lines, running from time t_0 to t_2 and from t_1 to t. Such a sum as shown in Fig. 4.4 is further on called kernel. Notice that in contrast to the Keldysh integrals the new integrals are always integrated forward in time leading to an additional minus sign for every vertex on the lower time branch. Therefore the phase factor $(-1)^b$ has to be added to the third diagrammatic rule, with b being the number of vertices on the lower time branch. Expressing a diagram of arbitrary order by such a kernel leads to a further kernel pre-factor $\frac{m}{2}!$. The reason is that for an arbitrary mth order diagram there exist $\frac{m}{2}!$ transformations which leave the diagram unchanged. Those transformations are found by simply interchanging the internal vertices (which can be done since all internal vertices are integrated along the whole Keldysh contour). Each of this

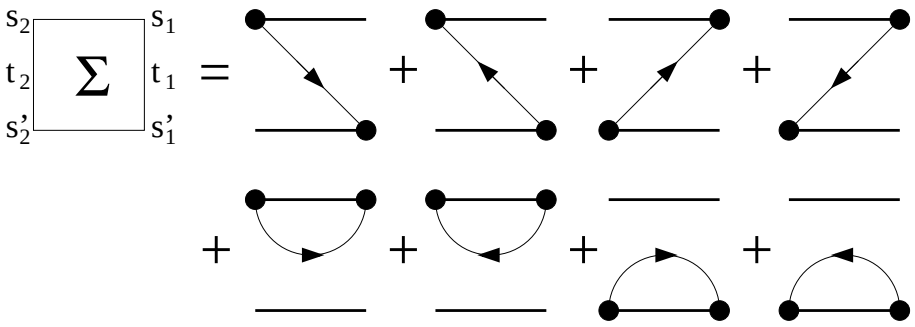

Figure 4.4: Kernel $\Sigma_{s_1 s_1' s_2 s_2'}(t_1, t_2)$ for the 2nd order diagram in $\bar{H}_T$. In kernel diagrams the time integration is restricted such that the absolute time ordering, i.e., the time ordering irrespective on which time branch the vertices are, is left unchanged.

diagram is represented by the same kernel leading to the additional pre-factor $\frac{m}{2}!$. The diagrammatic rules for the kernel diagrams therefore read:

Diagrammatic Rules for the Kernel Diagrams

To obtain the mth order contribution to the kernel $\Sigma_{s_1 s_1' s_2 s'2}(t_1, t_2)$ draw two time branches running form t_2 to t_1 and back and place arbitrarily m vertices onto it, where the vertices with the smallest and largest times, regardless on which time-branch they are, have the times t_2 and t_1, respectively. Connect pairs of vertices with directed reservoir lines and assign to each line a wave vector $\boldsymbol{k}_i$ and a reservoir index r_i. To every time segment connecting two vertices assign a quantum dot state s_i and to each vertex a tunneling time t_i.

1. Each occurring reservoir line running from vertex 1 to vertex 2 gives rise to $\gamma^{r,\pm}_{s_2 s_2', s_1 s_1'}(t_2, t_1)$. r is the index of the reservoir, $+$ corresponds to $t_1 >_K t_2$ and $-$ corresponds to $t_1 <_K t_2$. $s_{1,2}$ ($s'_{1,2}$) are the outgoing (incoming) dot states at each vertex. At vertex 1 where the line starts a particle has to be annihilated on the dot. To each vertex at most one reservoir line can be attached.

2. Each element of the Keldysh contour running from vertex 1 to vertex 2 gives rise to $\langle s_2 | U_0(t_2, t_1) | s_1 \rangle$ where s_1 is the outgoing dot state at vertex 1 and s_2 the incoming dot state at vertex 2.

3. The pre-factor is given by $(-1)^{b+c} \left(-\frac{i}{\hbar}\right)^m$ where m is the number of internal vertices, b the number of vertices on the lower time branch, and c the number of crossings of fermionic reservoir lines.

Now integrate over all vertex times t_i without changing their time ordering, regardless on which time branch they are ($\int_{t_0}^{t} dt_m \int_{t_m}^{t} dt_{m-1} ...$) and sum over all

reservoir indices r_i and dot states s_i. The mth order contribution is than given by the sum over all topologically different diagrams. Topologically different diagrams are diagrams which cannot be transformed into each other by moving the vertices along their time branches under following conditions: First, the vertices have to keeping their time order regardless on which time branch they are, second, vertices are not allowed to change their time-branch, and third, all reservoir lines have to be attached to their original vertices with the original direction.

Dyson like Equation

If the diagrams included in the kernel are restricted to irreducible diagrams, i.e., diagrams where it is not possible to draw any vertical line without crossing a reservoir line, but any number of reservoir lines occur in this kernel, the sum off all possible diagrams is given by the diagrammatic sequence shown in Fig. 4.5. Such a summation of sequences of kernels with free parts in between, containing no reservoir lines, can be performed by an iteration in the style of a Dyson equation. The corresponding algebraic expression for the reduced dot density

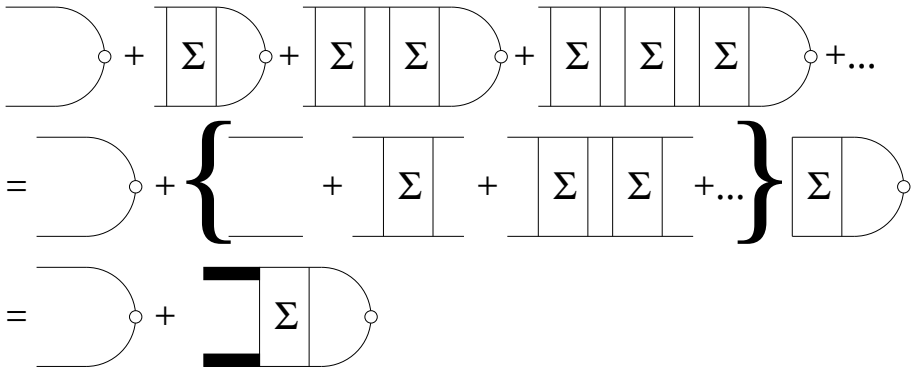

Figure 4.5: Dyson like equation. The expression within the brackets is again the reduced density matrix element at an earlier time.

matrix therefore reads

$$\begin{aligned} P_{ss'}(t) &= \sum_{\bar{s}\bar{s}'} \Pi_{ss'\bar{s}\bar{s}'}(t,t_0) P_{\bar{s}\bar{s}'}(t_0) \\ &+ \sum_{s_2 s_2'} \int_{t_0}^{t} dt_1 \int_{t_0}^{t_1} dt_2 \Pi_{ss'ss'}(t,t_1) \Sigma_{ss's_2s_2'}(t_1,t_2) P_{s_2s_2'}(t_2) \end{aligned} \tag{4.29}$$

with the propagator of the free segments

$$\Pi_{s_1 s_1' s_2 s_2'}(t_1,t_2) = \langle s_1 | U_0(t_1,t_2) | s_2 \rangle \langle s_2' | U_0(t_2,t_1) | s_1' \rangle. \tag{4.30}$$

Differentiating with respect to time t leads to the kinetic equation of the reduced density matrix

$$\frac{d}{dt}P_{ss'}(t) + \frac{i}{\hbar}\left(E_s - E_{s'}\right)P_{ss'}(t) = \sum_{s_2 s_2'}\int_{t_0}^{t} dt' \Sigma_{ss's_2s_2'}(t,t')P_{s_2s_2'}(t'). \tag{4.31}$$

The second term on the left hand side describes the time evolution of the reduced density operator without coupling to the reservoir. The right hand side is due to the coupling where it can be seen that the reduced density matrix depends on the density matrix at all times prior to t, hence the "full" kinetic equation is of a non-Markovian form. Notice that Eq. (4.31) is a formally exact equation although in order to solve this equation one usually has to approximate the kernel by calculating it in some finite order.

4.1.4 Mirror Symmetry

A useful symmetry of the kernel diagrams for the following considerations is the so called mirror symmetry. Moving in an arbitrary diagram (calling it diagram a) every vertex on the other time branch keeping its time and reversing all reservoir lines one gets a diagram (in the following called diagram a_m) which is the

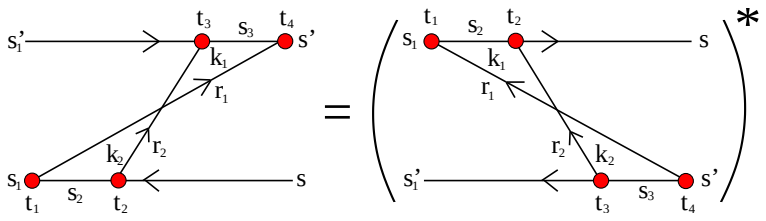

Figure 4.6: Some co-tunneling diagram and its mirror symmetric counterpart having all vertices on the opposite time branch and reversed reservoir lines.

complex conjugate to the original diagram. This is illustrated in Fig. 4.6 and can algebraically be written as

$$\Sigma^{(a)}_{s's s_1' s_1}(t_4,t_1) = \left(\Sigma^{(a_m)}_{ss's_1s_1'}(t_4,t_1)\right)^*. \tag{4.32}$$

The reason for this symmetry is that the tunneling and time lines of any vertex still have the same indices but with different direction. Looking at the diagrammatic rules one finds that the reversed direction only leads to a sign change in the occurring phases. Furthermore the direction of the reservoir lines with respect to the Keldysh contour is still the same and hence the mirror diagram leads to the complex conjugate result as compared to the original one. This relation reduces the number of diagrams needed for some finite order by a factor of two.

4.1.5 Current

Introducing the current operator between the quantum dot and the reservoir r,

$$\hat{I}_r = e\frac{d}{dt}\hat{N}_r = \frac{ie}{\hbar}\left[\hat{H}, \hat{N}_r\right]. \tag{4.33}$$

the desired current expectation value can be calculated. Using the commutators [C.4], [C.6] and [C.14] expression (4.33) yields

$$\hat{I}_r = \frac{ie}{\hbar}\sum_{\boldsymbol{k},l} T^r_{\boldsymbol{k}l} a^+_{\boldsymbol{k}r} c_l - \frac{ie}{\hbar}\sum_{\boldsymbol{k},l} T^{r,*}_{\boldsymbol{k}l} c^+_l a_{\boldsymbol{k}r}. \tag{4.34}$$

Transforming this operator with the unitary transformation (4.1) leads to

$$\bar{I}_r = \frac{ie}{\hbar}\sum_{\boldsymbol{k},l} \bar{T}^r_{\boldsymbol{k}l}(t) a^+_{\boldsymbol{k}r} c_l + (h.c.).$$

Therefore, the current operator has the same structure as the tunnel Hamiltonian. This means for the diagrams that the current operator is described by an external vertex with a reservoir line connected to it. Since the current operator is taken at time t, this vertex is the right most one. Again considering a sequence of kernels as shown in Fig. 4.7 an iteration in style of a Dyson equation can be

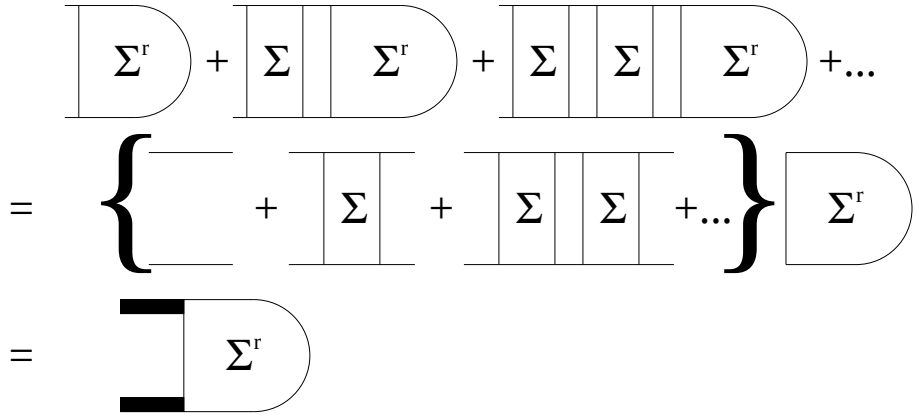

Figure 4.7: Dyson like equation for the expectation value of the current operator. The expression within the brackets is again the reduced density matrix element at an earlier time.

again calculated. The corresponding algebraic expression is

$$\langle I_r\rangle(t) = -e\sum_{ss_1s'_1}\int_{t_0}^{t} dt' \Sigma^r_{sss_1s'_1}(t,t') P_{s_1s'_1}(t') \tag{4.35}$$

where the kernel $\Sigma^r_{sss_1s'_1}(t,t')$ is that part of $\Sigma_{sss_1s'_1}(t,t')$ where the reservoir line attached to the right most vertex (which is the external one) corresponds to reservoir r and where this reservoir line is an outgoing (incoming) line if the right most vertex lies on the upper (lower) time branch.

4.1.6 Stationary Density Matrix and Current

The stationary non-equilibrium state of the quantum dot system is given by

$$P^{st}_{ss'} = \lim_{t_0\to-\infty} P_{ss'}(0). \tag{4.36}$$

Choosing an adiabatic switching on of the tunnel Hamiltonian

$$H_T(t) = \lim_{\nu\to 0} e^{\nu t} H_T \tag{4.37}$$

the kinetic equation for the stationary non-equilibrium state (4.31) reads

$$\frac{i}{\hbar}\left(E_s - E'_s\right) P^{st}_{ss'} = \sum_{s_1 s'_1} P^{st}_{s_1 s'_1} \int_{-\infty}^{0} dt' \Sigma_{ss's_1 s'_1}(0,t') \tag{4.38}$$

and the stationary current (4.35) is given by

$$\langle I^{st}_r \rangle = -e \sum_{ss_1 s'_1} P^{st}_{s_1 s'_1} \int_{-\infty}^{0} dt' \Sigma^r_{sss_1 s'_1}(0,t'). \tag{4.39}$$

The only task left, is to calculate the time-integral over a proper approximation of the kernel $\Sigma_{s_1 s'_1 s_2 s'_2}(t,t')$. The system of linear equations for the reduced density matrix (4.38) and the current (4.39) can then be solved by standard numerical tools.

4.1.7 Sequential Tunneling

In the sequential tunneling approximation for the case of a diagonal reduced density matrix the RTT leads to the same result as the master equation approach together with transitions calculated by Fermi's Golden Rule (see Chapter 2). To show this explicitly the kernel of Eq. (4.38) in the sequential tunneling approximation is needed. The occurring diagrams are shown in Fig. 4.4 where two of them are explicitly shown in Fig. 4.8. Applying the diagrammatic rules the mathematical expression

$$\int_{-\infty}^{0} dt' \Sigma^{(C1)}_{ss,s_1 s_1}(0,t') = \frac{1}{\hbar}\sum_r \sum_{\boldsymbol{k}} |T^r_{\boldsymbol{k}s_1 s}|^2 f_r(\epsilon_{\boldsymbol{k}}) \frac{i}{E_{s_1} - E_s - e(V_D - V_r) + \epsilon_{\boldsymbol{k}} + i0^+} \tag{4.40}$$

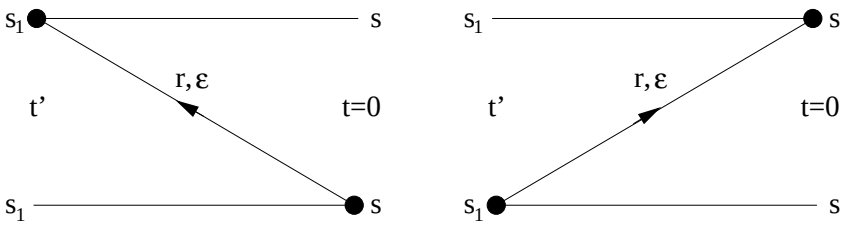

Figure 4.8: Two diagrams entering the kernel in the sequential tunneling approximation for the diagonal reduced density matrix. The left diagram is further on called $C1$ and the right one $C2$. Notice that $C2$ is the mirror symmetric diagram of $C1$.

is found for diagram $C1$, where the time integration has already been performed by the usage of the general expression

$$\int_{-\infty}^{0} dt_1 \int_{t1}^{0} dt_2 \cdots \int_{t_{m-2}}^{0} dt_{m-1} e^{-ix_1 t_1} e^{-ix_2 t_2} \cdots e^{-ix_{m-1} t_{m-1}} e^{\nu(t_1 \cdots t_{m-1})}$$
$$= i^{m-1} \frac{1}{x_1 + i\nu} \frac{1}{x_1 + x_2 + i\nu} \cdots \frac{1}{x_1 + x_2 + \cdots + x_{m-1} + i\nu}. \qquad (4.41)$$

Similarly one finds for the diagram $C2$

$$\int_{-\infty}^{0} dt' \Sigma^{(C2)}_{ss,s_1 s_1}(0,t') =$$
$$\frac{1}{\hbar} \sum_r \sum_{\boldsymbol{k}} |T^r_{\boldsymbol{k}s_1 s}|^2 f_r(\epsilon_{\boldsymbol{k}}) \frac{i}{E_s - E_{s_1} + e(V_D - V_r) - \epsilon_{\boldsymbol{k}} + i0^+} \qquad (4.42)$$

which is the complex conjugate of diagram $C1$ since those two diagrams are mirror symmetric with respect to each other. Hence, the sum of those diagrams entering the kernel is twice the real part of diagram $C1$ or $C2$. Since there is a continuum of states in the electronic reservoirs the sum over $\boldsymbol{k}$ is replaced by an integration such that Dirac's identity $\frac{1}{x+i0^+} = \mathcal{P}\frac{1}{x} - i\pi\delta(x)$ can be used for the integrand with $\mathcal{P}$ denoting the principal value. In the sum of diagram $C1$ and $C2$ only the term with the delta-function occurs such that

$$\int_{-\infty}^{0} dt' \left(\Sigma^{(C1)}_{ss,s_1 s_1}(0,t') + \Sigma^{(C2)}_{ss,s_1 s_1}(0,t') \right) =$$
$$\frac{2\pi}{\hbar} \sum_r \sum_{\boldsymbol{k}} |T^r_{\boldsymbol{k}s_1 s}|^2 f_r(\epsilon_{\boldsymbol{k}}) \delta(E_s - E_{s_1} + e(V_D - V_r) - \epsilon_{\boldsymbol{k}}). \qquad (4.43)$$

Together with Eq. (4.27) the Golden Rule transition rate

$$\Gamma^{r+}_{s_1 \to s} = \frac{2\pi}{\hbar} \sum_{\boldsymbol{k},l,j} T^{*,r}_{\boldsymbol{k}l} T^r_{\boldsymbol{k}j} \langle s|c^+_l|s_1\rangle \langle s_1|c_j|s\rangle$$
$$f_r(\epsilon_{\boldsymbol{k}}) \delta(E_s - E_{s_1} + e(V_D - V_r) - \epsilon_{\boldsymbol{k}}). \qquad (4.44)$$

is found. Similarly all other rates can be obtained by summing the three left over pairs of diagrams. Therefore, the kinetic equation in the sequential tunneling approximation is exactly the classical master equation used in the first chapter with rates obtained by Fermi's Golden Rule.

4.1.8 Diagrammatic Rules in Energy Space

With relation (4.41) the time integrals occurring in the stationary state can easily be calculated for diagrams of any order. Hence the rules for the kernel diagrams can also be formulated in energy space. For this purpose the new shortcut

$$\bar{\gamma}^{r,\pm}_{s_1 s_1', s_2 s_2'} = \sum_{\boldsymbol{k}} T^{*,r}_{\boldsymbol{k} s_1' s_1} T^{r}_{\boldsymbol{k} s_2 s_2'} \begin{cases} f_r(\epsilon) & \text{for } +, \\ [1 - f_r(\epsilon)] & \text{for } - \end{cases}$$

is introduced.

1. Draw all topologically different diagrams with fixed ordering of the vertices along the real axis, i.e., irrespective on which branch they are. The vertices are connected by reservoir lines as in time space. In addition to the energy E_s assigned to the propagators, assign an energy $\epsilon + e(V_r - V_D)$ to each reservoir line.

2. Write for each segment derived from $t_j \leq t \leq t_{j+1}$ a resolvent $1/[\Delta E_j + i0^+]$ where ΔE_j is the difference of the left going minus the right going energies (including the energies of the reservoir lines)

3. For each reservoir line running from t_1 to t_2 write $\bar{\gamma}^{r,\pm}_{s_2 s_2', s_1 s_1'}$. r is the index of the reservoir, $+$ corresponds to $t_1 >_K t_2$ and $-$ corresponds to $t_1 <_K t_2$. $s_{1,2}$ ($s'_{1,2}$) are the outgoing (incoming) dot states at each vertex.

4. The pre-factor is given by $(-1)^{b+c}\left(-\frac{i}{\hbar}\right)$ where b is the number of vertices on the lower part of the Keldysh contour and c the number of crossings of fermionic reservoir lines.

5. Sum over all reservoir indices and quantum dot states.

4.2 Co-tunneling

4.2.1 Diagrams

It turns out that there are 128 topologically different irreducible 4th-order diagrams contributing to the kernel $\sum_{s_1 s_1' s_2 s_2'}(t, t')$. One possibility to obtain all topologically different diagrams is to draw all diagrams which cannot be transformed into each other by arbitrarily moving the four vertices on their time branch and keeping the reservoir lines attached and directed as in the original diagram. It turns out that there are 10 such diagrams which are shown in Fig. 4.9. All

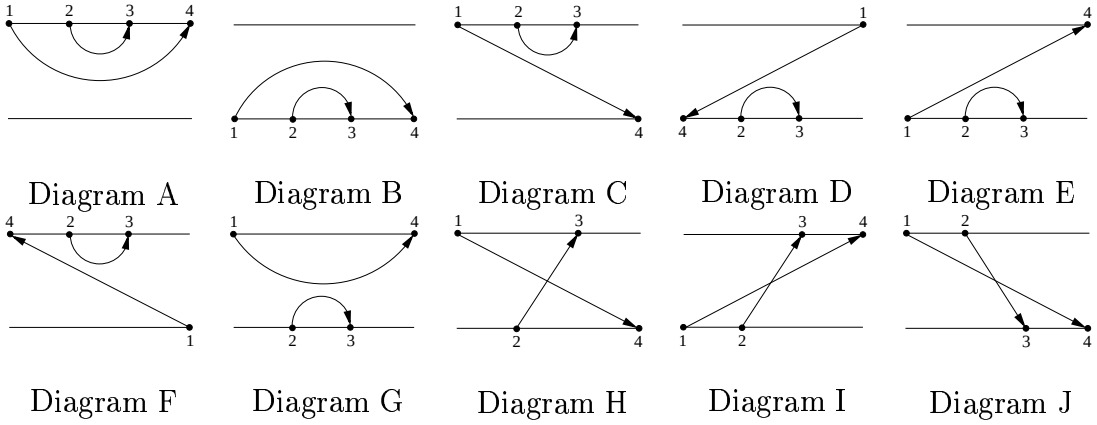

Figure 4.9: Shown are the 10 co-tunneling diagrams which cannot be transformed into each other by arbitrarily moving the four vertices on their time branch and keeping the reservoir lines attached and directed as in the original diagram.

topologically different diagrams are then found by realizing any possible time order of the four vertices along their time branch, as long as the diagrams are still irreducible. Reducible fourth order diagrams are already accounted for by the second order diagrams due to the Dyson like sequence (see Fig. 4.5). Generally each diagram of Fig. 4.9 can lead to 4! topologically different diagrams with the time ordering shown in Tab. 4.1. where some combinations are actually

1234	2134	1243	4231	1324	2143
2341	1342	2431	2314	3241	1432
3412	3421	4312	3142	2413	4321
4123	4213	3124	1423	4132	3214

Table 4.1: All possible time orderings of the four vertices occurring in co-tunneling diagrams. The time orderings shown in red color are reducible diagrams and already included within the Dyson sequence of the 2nd order.

reducible diagrams. Therefore every topologically different diagram has 16 co-tunneling contributions where some have to be subtracted, since diagram A,B,I

and J are invariant under interchanging reservoir lines. Therefore, 128 different co-tunneling diagrams enter the kernel. This number further on reduces to 64 due to the earlier discussed mirror symmetry.

4.2.2 Example of a Co-tunneling Contribution

As an example of a co-tunneling contribution the mathematically expression of the left hand diagram shown in Fig. 4.6 is in the following explicitly treated starting form the diagrammatic rules in time space. This diagram for example enters Eq. (4.38) of the stationary reduced density matrix. According to the diagrammatic rules it is found,

$$\int_{-\infty}^{0} dt_1 \Sigma^{(a)}_{s's s'_1 s_1}(0,t_1) = -\lim_{\nu\to 0^+} \frac{1}{\hbar^4} \sum_{s_2 s_3} \sum_{\boldsymbol{k}_1 \boldsymbol{k}_2} \sum_{r_1 r_2} \int_{-\infty}^{0} dt_1 \int_{t_1}^{0} dt_2 \int_{t_2}^{0} dt_3 \qquad (4.45)$$
$$\gamma^{r_1,+}_{s's_3 s_1 s_2}(0,t_1) \gamma^{r_2,+}_{s_3 s'_1 s_2 s}(t_3,t_2) e^{-\frac{i}{\hbar}E_{s_2}(t_1-t_2)} e^{-\frac{i}{\hbar}E_s t_2} e^{\frac{i}{\hbar}E_{s_3} t_3} e^{-\frac{i}{\hbar}E_{s'_1}(t_3-t_1)} e^{\nu(t_1+t_2+t_3)}.$$

Inserting (4.28) and (4.7) in order to write down the explicit time dependence of the integrand leads to

$$\begin{aligned}
\int_{-\infty}^{0} dt_1 \Sigma^{(a)}_{s's s'_1 s_1}(0,t_1) &= -\lim_{\nu\to 0^+} \frac{1}{\hbar^4} \sum_{s_2 s_3} \sum_{\boldsymbol{k}_1 \boldsymbol{k}_2} \sum_{r_1 r_2} \bar{T}^{r_1,*}_{\boldsymbol{k}_1 s_3 s'} \bar{T}^{r_1}_{\boldsymbol{k}_1 s_1 s_2} \bar{T}^{r_2,*}_{\boldsymbol{k}_2 s'_1 s_3} \bar{T}^{r_2}_{\boldsymbol{k}_2 s_2 s} \\
& f_{r_1}(\epsilon(\boldsymbol{k}_1)) f_{r_2}(\epsilon(\boldsymbol{k}_2)) \int_{-\infty}^{0} dt_1 \int_{t_1}^{0} dt_2 \int_{t_2}^{0} dt_3 e^{-\frac{i}{\hbar}(E_{s_2} - E_{s'_1} - \epsilon(\boldsymbol{k}_1) + e(V_D - V_{r_1}))t_1} \\
& e^{-\frac{i}{\hbar}(E_s - E_{s_2} - \epsilon(\boldsymbol{k}_2) + e(V_D - V_{r_2}))t_2} e^{-\frac{i}{\hbar}(E_{s'_1} - E_{s_3} + \epsilon(\boldsymbol{k}_2) - e(V_D - V_{r_2}))t_3} e^{\nu(t_1+t_2+t_3)}. \qquad (4.46)
\end{aligned}$$

The time integrations are straightforwardly treated with Eq. (4.41). Therefore, this specific co-tunneling diagram leads to

$$\begin{aligned}
\int_{-\infty}^{0} dt_1 \Sigma^{(a)}_{s's s'_1 s_1}(0,t_1) &= -\lim_{\nu\to 0^+} \frac{i^3}{\hbar} \sum_{s_2 s_3} \sum_{\boldsymbol{k}_1 \boldsymbol{k}_2} \sum_{r_1 r_2} \bar{T}^{r_1,*}_{\boldsymbol{k}_1 s_3 s'} \bar{T}^{r_1}_{\boldsymbol{k}_1 s_1 s_2} \bar{T}^{r_2,*}_{\boldsymbol{k}_2 s'_1 s_3} \bar{T}^{r_2}_{\boldsymbol{k}_2 s_2 s} \\
& f_{r_1}(\epsilon(\boldsymbol{k}_1)) f_{r_2}(\epsilon(\boldsymbol{k}_2)) \frac{1}{E_{s_2} - E_{s'_1} - \epsilon(\boldsymbol{k}_1) + e(V_D - V_{r_1}) + i\nu} \\
& \frac{1}{E_s - E_{s'_1} - \epsilon(\boldsymbol{k}_2) - \epsilon(\boldsymbol{k}_1) + e(2V_D - V_{r_2} - V_{r_1}) + i\nu} \\
& \frac{1}{E_s - E_{s_3} - \epsilon(\boldsymbol{k}_1) + e(V_D - V_{r_1}) + i\nu}. \qquad (4.47)
\end{aligned}$$

Similar to Chapter 2 it is assumed that the absolute value of the tunneling matrix element does only depend on the reservoir index r and the phases of the tunneling matrix elements are random with respect to the direction of the reservoir wave vector as described in Appendix A. Replacing the summation in $\boldsymbol{k}$-space of

(4.47) by $\sum_{\boldsymbol{k}} \to \int d\epsilon D(\epsilon)/4\pi \int d\Omega$ with the reservoir density of states $D(\epsilon)$ and following the steps of Appendix A the co-tunneling contribution of Eq. (4.47) can be written as

$$
\begin{aligned}
= \; & -\lim_{\nu\to 0^+} \frac{i^3}{\hbar} \sum_{s_2 s_3 r_1 r_2} \Bigg[\tau^{r_1}_{s_3 s' s_1 s_2} \tau^{r_2}_{s'_1 s_3 s_2 s} \int d\epsilon_1 D(\epsilon_1) \int d\epsilon_2 D(\epsilon_2) f_{r_1}(\epsilon(\boldsymbol{k}_1)) f_{r_2}(\epsilon(\boldsymbol{k}_2)) \\
& \frac{1}{E_{s_2} - E_{s'_1} - \epsilon(\boldsymbol{k}_1) + e(V_D - V_{r_1}) + i\nu} \\
& \frac{1}{E_s - E_{s'_1} - \epsilon(\boldsymbol{k}_2) - \epsilon(\boldsymbol{k}_1) + e(2V_D - V_{r_2} - V_{r_1}) + i\nu} \\
& \frac{1}{E_s - E_{s_3} - \epsilon(\boldsymbol{k}_1) + e(V_D - V_{r_1}) + i\nu} \Bigg]
\end{aligned}
\tag{4.48}
$$

where the shortcut

$$
\tau^{r_1}_{s_1 s'_1 s_2 s'_2} = \sum_{l_1} |t^{r_1}_{l_1}|^2 \langle s_1 | c_{l_1} | s'_1 \rangle^* \langle s_2 | c_{l_1} | s'_2 \rangle \tag{4.49}
$$

has been introduced. The energy integrals occurring are all well defined due to the regularized poles and can be, e.g., treated numerically. Generally there are two different integral types, where the first type can be written such that the inner energy integral has only one pole. Those integral types are found for all diagrams with one reservoir line starting before and ending after the other reservoir line, regardless on which time-branch the vertices are. All other diagrams lead to inner integrals with two poles. In Appendix G it is explicitly shown how both kind of occurring integrals are written in terms of principal value integrals and residua which is useful for a numerical treatment.

4.3 Signatures of the Excitation Spectrum in the Coulomb Blockade Regime

In the Coulomb blockade regime sequential tunneling is exponentially suppressed and co-tunneling becomes the leading contribution to the current. For metallic dots, i.e., the regime where the interaction energy U is much bigger than the typical excitation energy δ ($U \gg \delta$), it has been found that the co-tunneling current shows for low temperatures a cubic dependence on the applied transport voltage (see e.g. [13, 95]). In the regime where U and δ are of the same order, the tunnel current can show more complex signatures of the quantum dot's excitation spectrum even within the Coulomb blockade regime. This is in contrast to the sequential tunneling approximation where excited states influence transport only beyond the Coulomb blockade regime. The simplest quantum dot showing signatures of excited states within the Coulomb blockade regime is a dot containing two single-particle states separated by a finite energy difference δ. The additional interaction energy U has to be payed whenever both states are occupied. The four quantum dot states are labeled as: $|0,0\rangle$ empty dot, $|1,0\rangle$ single-particle ground state, $|1,1\rangle$ single-particle excited state, and $|2,0\rangle$ denotes the doubly occupied quantum dot state. Hence altogether four transport channels exist which are schematically sketched in the energy profile of Fig. 4.10. For the forthcoming considerations it is useful to discuss the charging diagram in the sequential tunneling approximation first. In the central region of Fig. 4.11 transport is Coulomb blocked and the quantum dot is occupied by one electron. The two resonance lines limiting the Coulomb blockade regime in the lower half correspond to the opening of the lowest transport channel $\mu(1,0;0,0)$. Similarly the limiting resonances of the upper half correspond to the ground state-ground state channel $\mu(2,0;1,0)$.

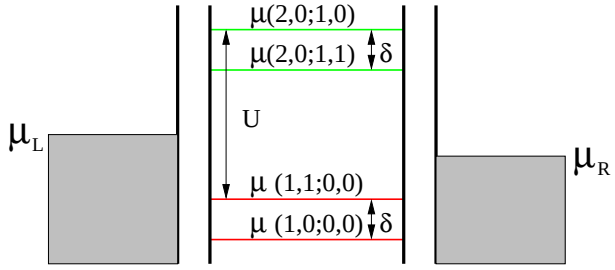

Figure 4.10: Shown are the four transport channels of a quantum dot with two single-particles states energetically split by the excitation energy δ. The interaction energy U has to be payed in case of double occupation.

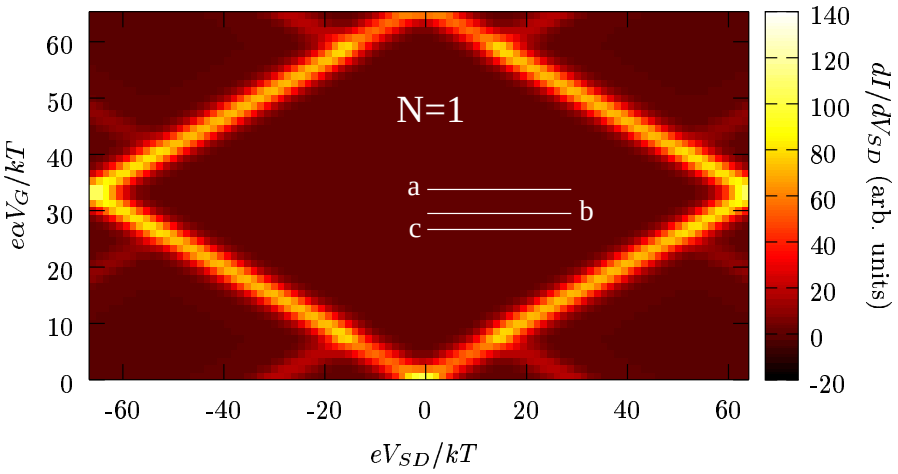

Figure 4.11: Charging diagram calculated in the sequential tunneling approximation. The tunneling current within the central Coulomb blockade regime is exponentially suppressed. Signatures of the excited single-particle state $|1,1\rangle$ are only found beyond the Coulomb blockade regime close to the corners of the diagram. The parameters used for calculating the charging diagram are: $\Gamma = 0.1kT$, $\delta = 14.67kT$, and $U = 52kT$.

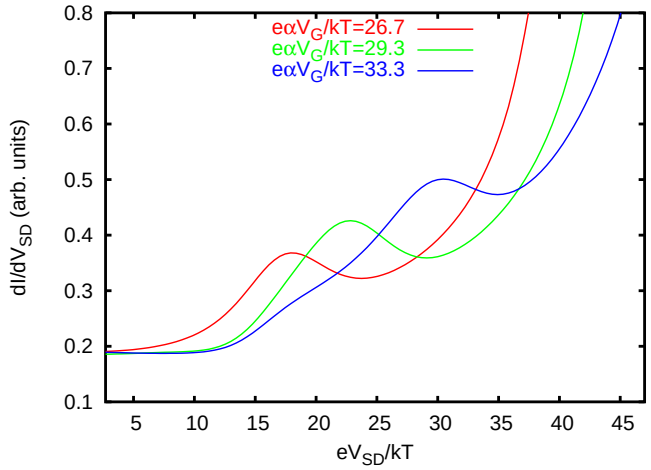

Figure 4.12: Co-tunneling signatures within the Coulomb blockade regime. Shown is the differential conductance versus the applied transport voltage for three different gate voltages $e\alpha V_G/kT = 26.7$, 29.3, and 33.3 corresponding to the traces a,b, and c in Fig. 4.11, respectively. The parameters used for this calculation are: $\Gamma = 0.1kT$, $\delta = 14.67kT$, and $U = 52kT$.

Signatures of excited states are only found beyond the Coulomb blockade regime which is the region in the vicinity of the corners of Fig. 4.11. Calculating the differential conductance, including the co-tunneling contributions of Section 4.2, leads to a qualitatively different result. As an example three traces within the Coulomb blockade regime, marked in Fig. 4.11, are shown in Fig. 4.12. For small voltages all three differential conductances start with the same value and at least the traces for $e\alpha V_G/kT = 29.3$ and $e\alpha V_G/kT = 33.3$ stay constant for small transport voltages. This constant and finite differential conductance is due to elastic co-tunneling by virtually tunneling through either the vacuum or the two-particle state. Additionally for all three traces a peak is found which shifts with increasing gate voltage linearly to higher source-drain voltages. In contrast to the traces at lower gate-voltages, the differential conductance of the highest gate-voltage ($e\alpha V_G/kT = 33.3$) shows an additional step emerging at the source-drain voltage $eV_{SD}/kT \approx 15$ which corresponds to the excitation energy δ. This step is strongly smeared due to temperature and especially due to the overlap with the peak occuring at higher voltages. On the left hand side of Fig. 4.13 the relative

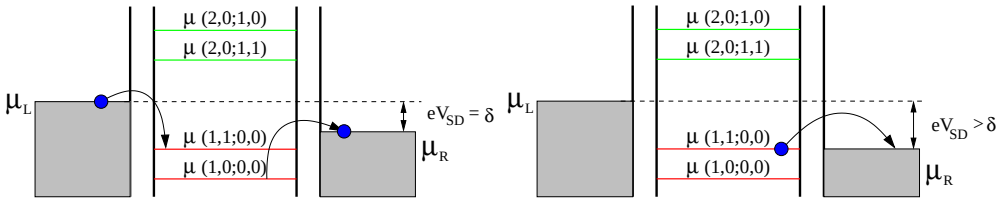

Figure 4.13: **Left:** At a high gate voltage the transport channel $\mu(1,1;0,0)$ is still below the transport window for $eV_{SD} = \delta$. Hence the quantum dot can be excited by an inelastic co-tunneling process but the excited electron is not able to leave the quantum dot by a sequential tunneling process. **Right:** Eventually, by further increasing V_{SD}, the electrochemical potential of the drain reservoir becomes resonant with the transport channel containing the excited state. Therefore an electron occupying the first excited state is able to tunnel out of the quantum dot by a sequential process with a higher tunneling rate as compared to co-tunneling processes.

position of the transport channels with respect to the electrochemical potentials in the reservoirs is shown at the parameters where the step occurs ($eV_{SD} = \delta$ and $e\alpha V_G/kT = 33.3$). In this situation inelastic co-tunneling becomes possible in which the quantum dot becomes excited during the tunneling process. This additional (to the elastic co-tunneling) co-tunneling process leads to a step in the differential conductance [103]. Eventually, by further increasing the source-drain voltage $eV_{SD} > \delta$, the electrochemical potential of the drain reservoir becomes resonant with the transport channel $\mu(1,1;0,0)$ (sketched on the right hand side of Fig. 4.13). Other than in the sequential tunneling approximation, where the $|1,1\rangle$ state cannot be occupied due to the Coulomb blockade effect, inelastic co-tunneling allows to occupy this excited state and the resonant channel leads to a peak in the differential conductance. The peak is, due to the smaller co-tunneling

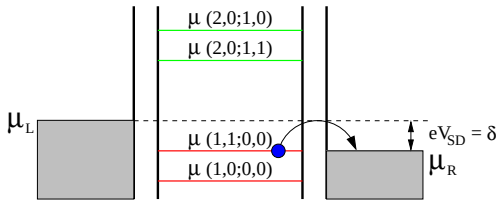

Figure 4.14: For low gate voltages the transport channel $\mu(1,1;0,0)$ is already within the transport window at $eV_{SD} = \delta$. The situation depicted is the gate voltage where $eV_{SD} = \delta$ coincides with the point where the electrochemical potential of the drain reservoir becomes resonant with the transport channel $\mu(1,1;0,0)$.

rate, lower as compared to the corresponding peak beyond the Coulomb blockade regime. For lower gate voltages the peak moves to lower source-drain voltages and eventually merges with the step at $eV_{SD} = \delta$ (see Fig. 4.14). For even lower gate voltages the channel $\mu(1,1;0,0)$ is already within the transport window at the source-drain voltage $eV_{SD} = \delta$ needed to allow for the inelastic co-tunneling process. Therefore the peak stays at the step position $eV_{SD} = \delta$ by further

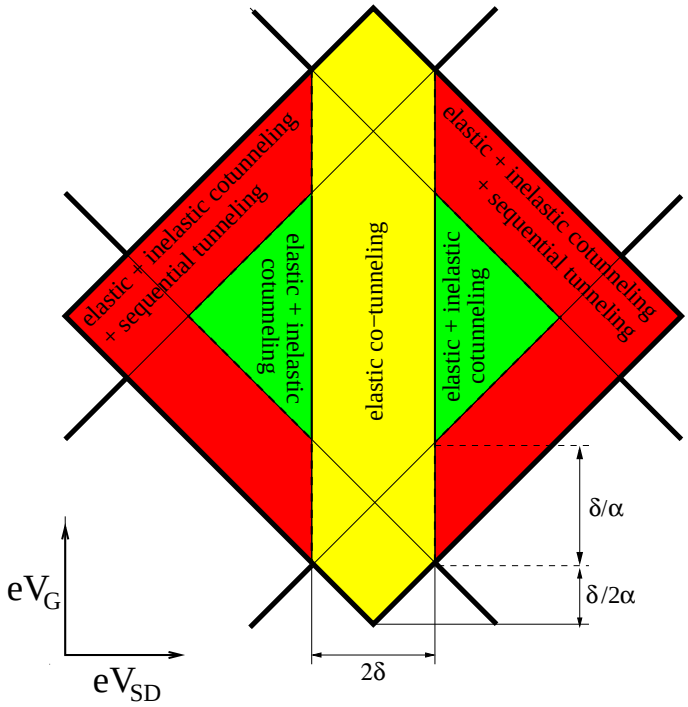

Figure 4.15: Schematic picture of the various tunneling regimes within the Coulomb blockade. By applying the gate voltage V_G the transport channel energies are shifted with respect to the electrochemical potentials in the reservoirs by $\Delta E = e\alpha V_G$.

decreasing V_G.

Combining all these processes various tunneling regimes within the Coulomb

blockade can be identified as sketched in Fig. 4.15. For transport voltages smaller than the excitation energy $eV_{SD} < \delta$ transport is dominated by elastic co-tunneling leading to a constant offset of the differential conductance. For gate-voltages in the vicinity of the Coulomb blockade center and $eV_{SD} > \delta$ a regime where elastic and inelastic co-tunneling occurs is found. In the remaining outer regime also sequential tunneling through the excited single-particle state is possible. At the border of this regime a peak occurs in the differential conductance. All described features are also found in the calculated charging diagram including co-tunneling (shown in Fig. 4.16). The onset of the inelastic co-tunneling

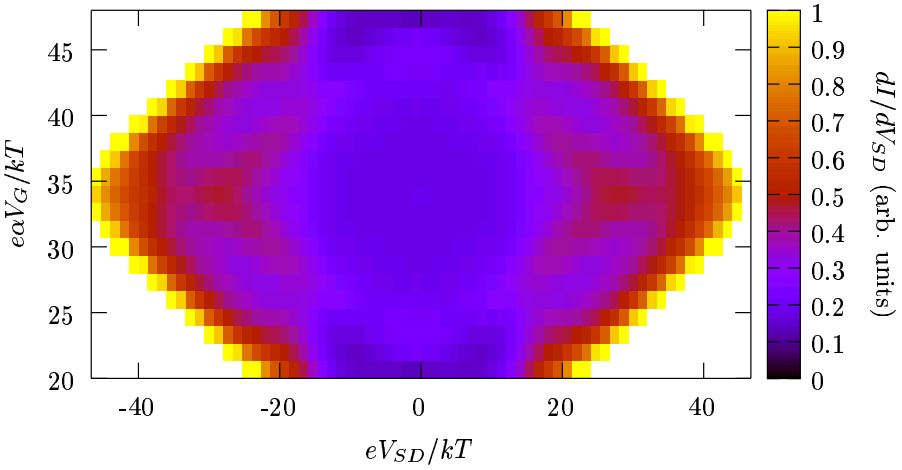

Figure 4.16: Calculated charging diagram within the Coulomb blockade regime including the co-tunneling contribution. The peak conductances due to resonant sequential tunneling have been "cut" from the color scale (white regions).

has been experimentally observed by Franceschi et al. [101] in a quantum dot formed from a deep etched rectangular heterostructure. The authors found an additional peak on top of the measured steps similar to the one obtained by the calculations presented in this section.

A diagram describing an inelastic co-tunneling process is shown in Fig. 4.17. Applying the diagrammatic rules the following mathematical expression is found

$$\int_{-\infty}^{0} dt_1 \Sigma^{(inel)}_{ssss}(0,t_1) \propto$$
$$Re\left\{ i \int d\epsilon_1 \frac{D(\epsilon_1)\left(1-f_R(\epsilon_1)\right)}{(E-\epsilon_1+i0^+)^2} \int d\epsilon_2 \frac{D(\epsilon_2) f_L(\epsilon_2)}{\epsilon_2-(\epsilon_1+\delta)+i0^+} \right\} \qquad (4.50)$$

with the state $s = |1,0\rangle$. Since the case discussed lies within the Coulomb blockade regime, the $\mu(1,0;0,0)$ channel energy E is below both electrochemical potentials of the reservoirs and one can argue that for sufficiently low temperatures the nominator of the first term in Eq. (4.50) vanishes at $\epsilon_1 = E$. Hence the main contribution originates from the Cauchy principal value ϵ_1-integral. In

Eq. (4.50) only the real part enters and therefore only the residuum of the inner integral needs to be considered. Therefore the integral of expression (4.50) yields

$$\int_{-\infty}^{0} dt_1 \Sigma^{(inel)}_{ssss}(0,t_1) \propto \int d\epsilon_1 \frac{D(\epsilon_1)\,(1-f_R(\epsilon_1))\,D(\epsilon_1) f_L(\epsilon_1+\delta)}{(E-\epsilon_1)^2}. \tag{4.51}$$

Due to the product of the two Fermi functions in Eq. (4.51) this diagram contributes to transport only if the applied source-drain voltage is bigger than or equal to the excitation energy ($eV_{SD} \geq \delta$). Due to the involved excitation of

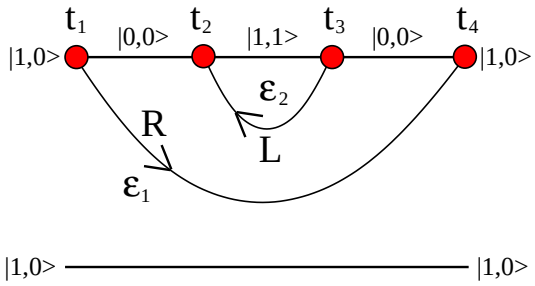

Figure 4.17: Shown is an example of a co-tunneling diagram describing a process which involves the single-particle ground and first excited state. Such a co-tunneling process is called inelastic.

the quantum dot this process is called inelastic co-tunneling and is schematically sketched in Fig. 4.13.

Chapter 5

Conclusions

In this thesis the electronic structure of isolated quantum dots as well as transport through dots coupled to two electronic reservoirs has been studied. Thereby special attention has been paid to the dependence of the tunneling current on Coulomb interaction and possible correlations in the quantum dot states.

In Chapter 2 transport in the weak coupling regime has been studied. While it is generally assumed that in this regime transport data can be straightforwardly interpreted in terms of energy differences of the isolated quantum dot states, it could be shown within this work that at finite temperature this is only true for non-degenerate energy levels. In case of degeneracy the resonance positions in the differential conductance generally depend on temperature and the level of degeneracy. On one hand this complicates the interpretation of transport data but, on the other hand, it allows to directly probe the degeneracy within a quantum dot.

One of the most prominent indicators for correlations in quantum dot states are negative differential conductances. Usually the negative differential conductance is caused by a partial reduction of the tunneling current by further increasing the applied transport voltage. In this thesis a mechanism is discussed which leads to a complete blocking of transport through a spherical quantum dot occupied by two and three Coulomb interaction electrons. This blocking mechanism leads to an enlargement of the regime where transport is exponentially suppressed and could be explained by the existence of a transition cascade, involving several dot states, which ends in a state blocked for further transport due to spin-selection rules.

In Chapter 3 the energy spectrum of an isolated spherical quantum dot has been studied in a particle-in-a-sphere model. Experimentally, spherical quantum dots are realized by colloidal nanocrystals which have been extensively probed by Scanning Tunneling Spectroscopy. In this work it could be shown that in such experiments the spherical symmetry of the electronic structure is broken due to the electric field induced by the tunneling tip. Calculating the quantum confined Stark effect on the electronic structure showed that the tip-induced electric field

can explain the broken symmetry found in wave-function mapping experiments. For the five-particle ground state it was found that exchange energy, caused by Coulomb interaction, is in competition to Stark energy. It could be shown that this competition leads to a transition of the symmetry of the ground state density as function of the nanocrystal radius.

Furthermore the effect of Coulomb interaction on the excitation spectrum of quantum dots in the strong confinement regime, i.e., the regime where a typical excitation energy is larger than the Coulomb energy, has been studied. It has been found that the lowest excitation energy generally decreases with increasing number of electrons occupying the dot. This effect has been recently measured in an inelastic light-scattering experiment performed on self-organized quantum dots which allowed to probe the excitation spectrum of the quantum dot for a varying number of dot electrons.

In Chapter 4 the influence of co-tunneling processes within the Coulomb blockade have been investigated by systematically calculating the tunneling current in fourth order perturbation theory in the tunnel coupling using a real-time Green's function approach for the case of non-equilibrium. A quantum dot with Coulomb interacting electrons was studied in the regime where the charging energy is bigger than the excitation energy. For such a dot a complex differential conductance pattern within the Coulomb blockade regime caused by a mixture of various co-tunneling and sequential tunneling processes has been found. The sequential tunneling is found to be possible even within the Coulomb blockade regime due to a preceding inelastic co-tunneling process. In particular the calculations presented in this work show a peak structure at the onset of sequential tunneling which has also been experimentally observed.

It seems inevitable in the treatment of such a wide subject that many questions remain open. In the following only two points will be mentioned that might be worth further considerations. One question mark concerns the channel blocking effect in the weak coupling regime. Although the reason for this blocking mechanism is connected to spin-selection rules it seems plausible that a similar blocking occurs if the spectral weight of the corresponding channel is not zero but small compared to the weights of the other channels participating in the transition cascade. Such small spectral weights are very likely in strongly correlated systems and hence such an "orbital" blocking mechanism could occur. Another question concerns possible correlation effects on the co-tunneling current. In the last part of this work a complex differential conductance pattern caused by the excitation spectrum of the quantum dot has been found within the Coulomb blockade regime and it seems plausible to ask if correlations would lead to as strong modifications of the tunneling current within the Coulomb blockade as, e.g., negative differential conductances in sequential transport outside the Coulomb blockade regime.

Appendix A

Spectral Weights

A.1 Sequential Tunneling

In a homogeneous reservoir the electronic energy does not depend on the direction of the corresponding wave vector such that the summation in $\boldsymbol{k}$-space of (2.6) can be replaced by $\sum_{\boldsymbol{k}} \to \int d\epsilon D(\epsilon)/4\pi \int d\Omega$ with the reservoir density of states $D(\epsilon)$. Furthermore assuming that the absolute values of the single particle tunneling matrix elements are also independent of the wave vector direction the summation over the wave vectors occurring in (2.6) reads

$$\begin{aligned}\sum_{\boldsymbol{k}} S^r_{\boldsymbol{k},s_i s_f} \ldots &= \int d\epsilon \frac{D(\epsilon)}{4\pi} \sum_{l,j} |T^r_{\epsilon l}||T^r_{\epsilon j}| < s_i|c_l|s_f >< s_f|c_j^+|s_i > \ldots \\ &\int d\Omega e^{-i(\Phi^r_{\epsilon\Omega l} - \Phi^r_{\epsilon\Omega j})}. \end{aligned} \tag{A.1}$$

For simplicity the Fermi functions and the Dirac delta functions which only depend on the reservoir and quantum dot energies are not written explicitly in (A.1). For those terms in Eq. (A.1) where the single-particle indices l and j are equal the phases will add constructively and the integration over Ω yields 4π. For the other terms where $l \neq j$ it is assumed that $e^{-i(\Phi^r_{\epsilon\Omega l} - \Phi^r_{\epsilon\Omega j})}$ is a random function with respect to Ω and hence

$$\int d\Omega e^{-i(\Phi^r_{\epsilon\Omega l} - \Phi^r_{\epsilon\Omega j})} = 4\pi\delta_{lj}. \tag{A.2}$$

For those randomly distributed phases the spectral weights read

$$S^r_{s_i s_f} = |T^r|^2 \sum_l | < s_i|c_l|s_f > |^2 \tag{A.3}$$

where the reservoir energy and dot state dependence of the tunneling matrix elements have been neglected for simplicity. Notice that the spectral weight (A.3)

also ensures that the electron spin is conserved during the tunneling process. Inserting this expression into (2.6) the sequential tunneling rates read

$$\begin{aligned}\Gamma^{r,+}_{s_i\to s_f} &= \frac{2\pi}{\hbar}S^r_{s_i s_f}D(E_{s_f}-E_{s_i}-e(V_D-V_r))f^r(E_{s_f}-E_{s_i}-e(V_D-V_r)) \qquad \text{(A.4)}\\ \Gamma^{r,-}_{s_i\to s_f} &= \frac{2\pi}{\hbar}S^r_{s_f s_i}D(E_{s_i}-E_{s_f}+e(V_D-V_r))\left[1-f^r(E_{s_i}-E_{s_f}+e(V_D-V_r))\right].\end{aligned}$$

A.2 Co-tunneling

As in the case of sequential tunneling the summations of the $\boldsymbol{k}$-space is replaced by $\sum_{\boldsymbol{k}} \to \int d\epsilon D(\epsilon)/4\pi \int d\Omega$, assuming that the energy of a reservoir electron does only depend on the absolute value of the wave vector $\boldsymbol{k}$. Also assuming that the absolute values of the single-particle tunneling matrix elements are independent of the wave vector direction an arbitrary co-tunneling contribution to the kernel can be written as

$$\begin{aligned}\int_{-\infty}^{0} dt_1 \Sigma^{(co)}_{s' s s'_1 s_1}(0,t_1) \propto \sum_{s_2 s_3}\sum_{r_1 r_2}\int d\epsilon_1 \frac{D(\epsilon_1)}{4\pi}\int d\epsilon_2 \frac{D(\epsilon_2)}{4\pi}...\\ \times\left[\sum_{l_1,j_1}|T^{r_1}_{\epsilon_1 l_1}|\langle s_3|c_{l_1}|s'\rangle^*|T^{r_1}_{\epsilon_1 j_1}|\langle s_2|c_{j_1}|s\rangle\int d\Omega_1 e^{-i(\Phi^{r_1}_{\epsilon_1\Omega_1 l_1}-\Phi^{r_1}_{\epsilon_1\Omega_1 j_1})}\right]\\ \times\left[\sum_{l_2,j_2}|T^{r_2}_{\epsilon_2 l_2}|\langle s'_1|c_{l_2}|s_3\rangle^*|T^{r_2}_{\epsilon_2 j_2}|\langle s_3|c_{j_2}|s_1\rangle\int d\Omega_2 e^{-i(\Phi^{r_2}_{\epsilon_2\Omega_2 l_2}-\Phi^{r_2}_{\epsilon_2\Omega_2 j_2})}\right] \qquad \text{(A.5)}\end{aligned}$$

where in the energy dependent integrand is not explicitly written in order to focus on the angular integration. Using expression (A.2) only those terms of Eq. (A.5) where $l_1 = j_1$ and $l_2 = j_2$ contribute such that

$$\begin{aligned}\int_{-\infty}^{0} dt_1 \Sigma^{(co)}_{s' s s'_1 s_1}(0,t_1) \propto \sum_{s_2 s_3}\sum_{r_1 r_2}\int d\epsilon_1 \frac{D(\epsilon_1)}{4\pi}\int d\epsilon_2 \frac{D(\epsilon_2)}{4\pi}... \qquad \text{(A.6)}\\ \sum_{l_1}|T^{r_1}_{\epsilon_1 l_1}|\langle s_3|c_{l_1}|s'\rangle^*|T^{r_1}_{\epsilon_1 l_1}|\langle s_2|c_{j_1}|s\rangle\sum_{l_2}|T^{r_2}_{\epsilon_2 l_2}|\langle s'_1|c_{l_2}|s_3\rangle^*|T^{r_2}_{\epsilon_2 l_2}|\langle s_3|c_{l_2}|s_1\rangle.\end{aligned}$$

Neglecting the reservoir energy dependence of the tunneling matrix elements and introducing

$$\tau^{r_1}_{s_1 s'_1 s_2 s'_2} = \sum_{l_1}|T^{r_1}_{l_1}|^2\langle s_1|c_{l_1}|s'_1\rangle^*\langle s_2|c_{l_1}|s'_2\rangle \qquad \text{(A.7)}$$

this expression reads

$$\int_{-\infty}^{0} dt_1 \Sigma^{(co)}_{s's s'_1 s_1}(0,t_1) \propto \sum_{s_2 s_3} \sum_{r_1 r_2} \tau^{r_1}_{s_3 s' s_2 s} \tau^{r_2}_{s'_1 s_3 s_3 s_1} \int d\epsilon_1 D(\epsilon_1) \int d\epsilon_2 D(\epsilon_2) ... \tag{A.8}$$

which also ensures spin-conservation during a tunneling process.

Appendix B

Transformed Time-evolution Operator

In the theoretical treatment of quantum mechanical problems it often proofed to be useful to apply some unitary transformation to the quantum states and operators in such a way that the observable quantities are left unchanged. The transformation rule of the time-evolution operator is in the following explicitly derived for an arbitrary time-dependent unitary transformation. If the Schrödinger equation reads

$$i\hbar\frac{\partial}{\partial t}|\psi(t)\rangle = \hat{H}(t)|\psi(t)\rangle \tag{B.1}$$

the time-evolution operator transforming a certain state from one point in time t' to another time t is known to be

$$T_D e^{-\frac{i}{\hbar}\int_{t'}^{t} dt'' \hat{H}(t'')}. \tag{B.2}$$

Dyson's time-ordering operator T_D orders according to the rule **last goes left** without any sign changes [104]. Transforming the time-dependent Schrödinger equation (B.1) by some unitary transformation $\hat{U}(t,t_0)$

$$\begin{aligned} i\hbar\frac{\partial}{\partial t}\hat{U}^+(t,t_0)\hat{U}(t,t_0)|\psi(t)\rangle = \\ \hat{U}^+(t,t_0)\hat{U}(t,t_0)\hat{H}(t)\hat{U}^+(t,t_0)\hat{U}(t,t_0)|\psi(t)\rangle \end{aligned} \tag{B.3}$$

and introducing the transformed state $|\bar{\psi}(t)\rangle = \hat{U}(t,t_0)|\psi(t)\rangle$ expression (B.3) can be written as

$$\begin{aligned} i\hbar\left(\frac{\partial}{\partial t}\hat{U}^+(t,t_0)\right) + i\hbar\hat{U}^+(t,t_0)\frac{\partial}{\partial t}|\bar{\psi}(t)\rangle = \\ \hat{U}^+(t,t_0)\hat{U}(t,t_0)\hat{H}(t)\hat{U}^+(t,t_0)|\bar{\psi}(t)\rangle. \end{aligned} \tag{B.4}$$

Multiplying from left with $\hat{U}(t,t_0)$ the transformed Schrödinger equation

$$i\hbar\frac{\partial}{\partial t}|\bar{\psi}(t)\rangle = \left[\hat{U}(t,t_0)\hat{H}(t)\hat{U}^+(t,t_0) - i\hbar\hat{U}(t,t_0)\left(\frac{\partial}{\partial t}\hat{U}^+(t,t_0)\right)\right]|\bar{\psi}(t)\rangle \quad \text{(B.5)}$$

is of the same form as the original Eq. (B.1) and therefore the operator occurring in the exponent of the transformed time-evolution operator is

$$\bar{H}(t) = \hat{U}(t,t_0)\hat{H}(t)\hat{U}^+(t,t_0) - i\hbar\hat{U}(t,t_0)\left(\frac{\partial}{\partial t}\hat{U}^+(t,t_0)\right). \quad \text{(B.6)}$$

B.1 Transport Hamiltonian

In the following (B.6) is explicitly applied to the transport Hamiltonian

$$\hat{H} = \hat{H}_R + \hat{H}_D + \hat{H}_T \quad \text{(B.7)}$$

$$\hat{H}_R = \sum_{\boldsymbol{k},r}\epsilon_{\boldsymbol{k}r}a^+_{\boldsymbol{k}r}a_{\boldsymbol{k}r} + e\sum_r V_r\hat{N}_r \quad \text{(B.8)}$$

$$\hat{H}_D = \sum_s E_s\hat{P}_{ss} + eV_D\hat{N} \quad \text{(B.9)}$$

$$\hat{H}_T = \sum_{\boldsymbol{k},l,r}T^r_{\boldsymbol{k}l}a^+_{\boldsymbol{k}r}c_l + (h.c.) \quad \text{(B.10)}$$

using the unitary transformation

$$U(t,t_0) = e^{\frac{ie}{\hbar}\left(\sum_r V_r\hat{N}_r + V_D\hat{N}\right)(t-t_0)}. \quad \text{(B.11)}$$

Inserting (B.7) in (B.6) leads to

$$\bar{H} = UH_RU^+ + UH_DU^+ + UH_TU^+ - i\hbar U\left(\frac{\partial}{\partial t}U^+\right). \quad \text{(B.12)}$$

In the following the four terms on the right hand side of Eq. (B.12) are calculated:

Transformation $-i\hbar U\left(\frac{\partial}{\partial t}U^+\right)$

The derivative of (B.11) with respect to the time t can be easily calculated and leads to

$$\frac{\partial}{\partial t}U^+ = -\frac{ie}{\hbar}\left(\sum_r V_r\hat{N}_r + V_D\hat{N}\right)U^+. \quad \text{(B.13)}$$

Since the operator in the exponent of the unitary transformation is the same as the operator within the brackets on the right hand side of (B.13) those two terms commute ($[\hat{A}, e^{\hat{A}}] = 0$) and the desired transformation yields

$$-i\hbar U\left(\frac{\partial}{\partial t}U^+\right) = -e\left(\sum_r V_r\hat{N}_r + V_D\hat{N}\right). \quad \text{(B.14)}$$

Transformation UH_RU^+

For the following transformations the fact that the commutator $[\hat{A}, e^{\hat{B}}]$ does vanish if $[\hat{A}, \hat{B}] = 0$ (see Appendix C) can be use. Writing the transformed reservoir Hamiltonian as

$$UH_RU^+ = H_R + U\left[H_R, U^+\right] \tag{B.15}$$

and looking at the commutator

$$\left[H_R, -e\left(\sum_r V_r\hat{N}_r + V_D\hat{N}\right)\right] = 0 \tag{B.16}$$

it is found that this commutator is zero since both number operators commute with H_R. Hence the reservoir Hamiltonian is invariant under the transformation (B.11):

$$UH_RU^+ = H_R. \tag{B.17}$$

Transformation UH_DU^+

Similarly to the reservoir Hamiltonian it can be shown that the dot Hamiltonian is also invariant under the unitary transformation $U(t, t_0)$ and therefore

$$UH_DU^+ = H_D. \tag{B.18}$$

Transformation UH_TU^+

In contrast to H_R and H_D the tunnel Hamiltonian (B.10) does not commute with the unitary transformation (B.11). Therefore this transformation has to be discussed in more detail. Writing the transformed Hamiltonian as

$$UH_TU^+ = H_T + U\left[H_T, U^+\right] \tag{B.19}$$

the right hand side commutator reads

$$\begin{aligned}
\left[H_T, U^+\right] &= \sum_{n=0}^{\infty}\frac{1}{n!}\left[H_T, \left\{-\frac{ie}{\hbar}\left(\sum_r V_r\hat{N}_r + V_D\hat{N}\right)(t-t_0)\right\}^n\right] \\
&= \sum_{r'}\sum_{n=0}^{\infty}\frac{1}{n!}\left[H_T^{r',(i)}, \left\{-\frac{ie}{\hbar}\left(\sum_r V_r\hat{N}_r + V_D\hat{N}\right)(t-t_0)\right\}^n\right] \\
&\quad + \sum_{r'}\sum_{n=0}^{\infty}\frac{1}{n!}\left[H_T^{r',(o)}, \left\{-\frac{ie}{\hbar}\left(\sum_r V_r\hat{N}_r + V_D\hat{N}\right)(t-t_0)\right\}^n\right].
\end{aligned}$$

In this expression the *tunneling-in* operator $H_T^{r',(i)} = \sum_{\boldsymbol{k},l} T_{\boldsymbol{k}l}^{r,*} c_l^+ a_{\boldsymbol{k},r}$ and the *tunneling-out* operator $H_T^{r',(o)} = \sum_{\boldsymbol{k},l} T_{\boldsymbol{k}l}^{r} a_{\boldsymbol{k},r}^+ c_l$ have been introduced. The commutators

$$\begin{aligned}\left[H_T^{r',(i)}, -\frac{ie}{\hbar}\left(\sum_r V_r\hat{N}_r + V_D\hat{N}\right)(t-t_0)\right] &= -\frac{ie}{\hbar}(V_D - V_r)(t-t_0)\,H_T^{r,(i)}\\ \left[H_T^{r',(o)}, -\frac{ie}{\hbar}\left(\sum_r V_r\hat{N}_r + V_D\hat{N}\right)(t-t_0)\right] &= \frac{ie}{\hbar}(V_D - V_r)(t-t_0)\,H_T^{r,(o)}\end{aligned}$$

are obtained by using Appendix C. Combining those commutators with the relation $\sum_{n=0}^{\infty}\frac{1}{n!}[A,B^n] = e^B(e^\xi - 1)A$ which holds as long $[A,B] = \xi A$ (see Appendix C) it is found that

$$\begin{aligned}\left[H_T, U^+\right] &= \sum_r U^+\left(e^{-\frac{ie}{\hbar}(V_D-V_r)(t-t_0)} - 1\right)H_T^{r,(i)}\\ &+ \sum_r U^+\left(e^{\frac{ie}{\hbar}(V_D-V_r)(t-t_0)} - 1\right)H_T^{r,(o)}.\end{aligned} \tag{B.20}$$

Hence by introducing the transformed tunneling matrix element

$$\bar{T}_{\boldsymbol{k}l}^r(t) = T_{\boldsymbol{k}l}^r e^{-\frac{ie}{\hbar}(V_D-V_r)(t-t_0)} \tag{B.21}$$

the desired transformation reads

$$UH_TU^+ = \sum_{\boldsymbol{k},l,r}\bar{T}_{\boldsymbol{k}l}^r(t)a_{\boldsymbol{k}r}^+c_l + (h.c.). \tag{B.22}$$

Transformed Transport Hamiltonian

Adding all transformed terms it is found that the constant potentials V_r and V_D are transformed into the tunneling matrix elements

$$\bar{H}_R = \sum_{\boldsymbol{k},r}\epsilon_{\boldsymbol{k}r}a_{\boldsymbol{k}r}^+a_{\boldsymbol{k}r} \tag{B.23}$$

$$\bar{H}_D = \sum_s E_s\hat{P}_{ss} \tag{B.24}$$

$$\bar{H}_T = \sum_{\boldsymbol{k},l,r}\bar{T}_{\boldsymbol{k}l}^r(t)a_{\boldsymbol{k}r}^+c_l + (h.c.). \tag{B.25}$$

Appendix C

Commutators

In the following some frequently used commutators involving parts of the transport Hamiltonian

$$\hat{H}_R = \sum_{\boldsymbol{k},r} \epsilon_{\boldsymbol{k}r} a^+_{\boldsymbol{k}r} a_{\boldsymbol{k}r} + e \sum_r V_r \hat{N}_r \tag{C.1}$$

$$\hat{H}_D = \sum_s E_s \hat{P}_{ss} + eV_D \hat{N} \tag{C.2}$$

$$\hat{H}_T = \sum_{\boldsymbol{k},l,r} T^r_{\boldsymbol{k}l} a^+_{\boldsymbol{k}r} c_l + (h.c.) \tag{C.3}$$

are calculated.

Commutator $\left[H_R, \hat{N}_r\right]$

$$\begin{aligned} \left[H_R, \hat{N}_r\right] &= \sum_{\boldsymbol{k},r} \sum_{\boldsymbol{k'},r'} \epsilon_{\boldsymbol{k}r} \left[a^+_{\boldsymbol{k}r} a_{\boldsymbol{k}r}, a^+_{\boldsymbol{k'}r'} a_{\boldsymbol{k'}r'}\right] + e \sum_{r'} V_{r'} \left[\hat{N}_{r'}, \hat{N}_r\right] \\ &= 0 \end{aligned} \tag{C.4}$$

Commutator $\left[H_R, \hat{N}\right]$

$$\begin{aligned} \left[H_R, \hat{N}\right] &= \sum_{\boldsymbol{k},r} \sum_l \epsilon_{\boldsymbol{k}r} \left[a^+_{\boldsymbol{k}r} a_{\boldsymbol{k}r}, c^+_l c_l\right] + e \sum_{r'} V_r \left[\hat{N}_r, \hat{N}\right] \\ &= 0 \end{aligned} \tag{C.5}$$

Commutator $\left[H_D, \hat{N}_r\right]$

$$\left[H_D, \hat{N}_r\right] = \sum_{\boldsymbol{k},r} \sum_s E_s \left[\hat{P}_{ss}, a^+_{\boldsymbol{k}r} a_{\boldsymbol{k}r}\right] + eV_D \left[\hat{N}, \hat{N}_r\right] = 0 \tag{C.6}$$

The commutator involving the projection operator $\hat{P}_{ss}$ is zero because a diagonal projection operator does conserve the number of particles.

Commutator $\left[H_D, \hat{N}\right]$

$$\left[H_D, \hat{N}\right] = \sum_l \sum_s E_s \left[\hat{P}_s, c^+_l c_l\right] + eV_D \left[\hat{N}, \hat{N}\right] = 0 \tag{C.7}$$

Commutator $\left[H_T, \hat{N}_{r'}\right]$

Introducing the *tunneling-in* operator $H_T^{r',(i)} = \sum_{\boldsymbol{k},l} T^{r,*}_{\boldsymbol{k}l} c^+_l a_{\boldsymbol{k},r}$ and the *tunneling-out* operator $H_T^{r',(o)} = \sum_{\boldsymbol{k},l} T^r_{\boldsymbol{k}l} a^+_{\boldsymbol{k},r} c_l$ the tunnel Hamiltonian (C.3) can be written as

$$H_T = \sum_r H_T^{r,(o)} + H_T^{r,(i)} \tag{C.8}$$

and hence

$$\left[H_T, \hat{N}_{r'}\right] = \sum_r \left[H_T^{r,(o)}, \hat{N}_{r'}\right] + \left[H_T^{r,(i)}, \hat{N}_{r'}\right]. \tag{C.9}$$

The commutator of the introduced *tunneling-out* operator with the reservoir number operator is

$$\left[H_T^{r,(o)}, \hat{N}_{r'}\right] = \sum_{\boldsymbol{k}',\boldsymbol{k},l} T^r_{\boldsymbol{k}l} \left[a^+_{\boldsymbol{k}r} c_l, a^+_{\boldsymbol{k}'r'} a_{\boldsymbol{k}'r'}\right]. \tag{C.10}$$

Using the commutator relation $[AB, C] = A[B, C] + [A, C]B$ the commutator of the right hand side of (C.10) reads

$$\begin{aligned} \left[a^+_{\boldsymbol{k}r} c_l, a^+_{\boldsymbol{k}'r'} a_{\boldsymbol{k}'r'}\right] &= a^+_{\boldsymbol{k}r} a^+_{\boldsymbol{k}'r'} \left[c_l, a_{\boldsymbol{k}'r'}\right] + a^+_{\boldsymbol{k}r} \left[c_l, a^+_{\boldsymbol{k}'r'}\right] a_{\boldsymbol{k}'r'} \\ &\quad \left[a^+_{\boldsymbol{k}r}, a^+_{\boldsymbol{k}'r'}\right] a_{\boldsymbol{k}'r'} c_l + a^+_{\boldsymbol{k}'r'} \left[a^+_{\boldsymbol{k}r}, a_{\boldsymbol{k}'r'}\right] c_l \\ &= \delta_{\boldsymbol{k},\boldsymbol{k}'} \delta_{r,r'} a^+_{\boldsymbol{k}'r'} c_l \end{aligned} \tag{C.11}$$

where in the last step the relation $[A,B] = [A,B]_+ - 2BA$ was used. Inserting expression (C.10) into (C.11) leads to

$$\begin{aligned}\left[H_T^{r,(o)}, \hat{N}_{r'}\right] &= \delta_{r,r'} \sum_{\boldsymbol{k},l} T^r_{\boldsymbol{k}l} a^+_{\boldsymbol{k}r} c_l \\ &= \delta_{r,r'} H_T^{r,(o)}. \end{aligned} \tag{C.12}$$

Similarly one can show that

$$\left[H_T^{r,(i)}, \hat{N}_{r'}\right] = -\delta_{r,r'} H_T^{r,(i)} \tag{C.13}$$

leading to the desired commutator

$$\left[H_T, \hat{N}_{r'}\right] = H_T^{r',(o)} - H_T^{r',(i)}. \tag{C.14}$$

Commutator $\left[H_T, \hat{N}\right]$

$$\left[H_T^{r,(o)}, \hat{N}\right] = \sum_{\boldsymbol{k},l,l'} T^r_{\boldsymbol{k}l} \left[a^+_{\boldsymbol{k}r} c_l, c^+_{l'} c_{l'}\right] \tag{C.15}$$

Using the commutator relation $[AB,C] = A[B,C] + [A,C]B$ the right hand side of Eq. (C.15) yields

$$\begin{aligned}\left[a^+_{\boldsymbol{k}r} c_l, c^+_{l'} c_{l'}\right] &= a^+_{\boldsymbol{k}r} c^+_{l'} \left[c_l, c_{l'}\right] + a^+_{\boldsymbol{k}r} \left[c_l, c^+_{l'}\right] c_{l'} \\ &\quad \left[a^+_{\boldsymbol{k}r}, c^+_{l'}\right] c_{l'} c_l + c^+_{l'} \left[a^+_{\boldsymbol{k}r}, c_{l'}\right] c_l \\ &= -\delta_{l,l'} a^+_{\boldsymbol{k}'r} c_l \end{aligned} \tag{C.16}$$

where in the last step the relation $[A,B] = [A,B]_+ - 2BA$ was used. Inserting expression (C.16) into (C.15) leads to

$$\begin{aligned}\left[H_T^{r,(o)}, \hat{N}\right] &= -\sum_{\boldsymbol{k},l} T^r_{\boldsymbol{k}l} a^+_{\boldsymbol{k}r} c_l \\ &= -H_T^{r,(o)}. \end{aligned} \tag{C.17}$$

Similarly one can show that

$$\left[H_T^{r,(i)}, \hat{N}\right] = H_T^{r,(i)} \tag{C.18}$$

leading to the commutator

$$\left[H_T, \hat{N}\right] = \sum_r H_T^{r,(i)} - H_T^{r,(o)}. \tag{C.19}$$

Commutator $\sum_{n=0}^{\infty}[A,B^n]$

The commutator

$$\sum_{n=0}^{\infty}[A,B^n] = \sum_{n=0}^{\infty}(-B^nA+AB^n) \tag{C.20}$$

can be further simplified if the relation $[A,B]=\xi A$ holds with ξ being a complex number. Then

$$\begin{aligned} AB^n &= BAB^{n-1}+[A,B]\,B^{n-1} \text{ with } [A,B]=\xi A \\ &= BAB^{n-1}+\xi AB^{n-1} \\ &= (B+\xi)\,AB^{n-1} \\ &= (B+\xi)\,(B+\xi)\,AB^{n-2} \\ &\ldots \\ &= (B+\xi)^n A \end{aligned} \tag{C.21}$$

can be inserted into Eq. (C.20) leading to

$$\begin{aligned} \sum_{n=0}^{\infty}[A,B^n] &= \sum_{n=0}^{\infty}(-B^nA+(B+\xi)^nA) \\ &= \left(-e^B+e^{B+\xi}\right)A \end{aligned} \tag{C.22}$$

and therefore

$$\sum_{n=0}^{\infty}[A,B^n] = e^B\left(e^{\xi}-1\right)A. \tag{C.23}$$

Commutator $[A,B^n]$

By successively expanding the commutator $[A,B^n]$ one obtains

$$[A,B^n] = B^{n-1}[A,B]+\left[A,B^{n-1}\right]B \tag{C.24}$$

$$= B^{n-1}[A,B]+B^{n-2}[A,B]\,B+\left[A,B^{n-2}\right]B^2 \tag{C.25}$$

$$\ldots$$

$$[A,B^n] = \sum_{m=0}^{n-1}B^{n-1-m}[A,B]\,B^m. \tag{C.26}$$

This relation is e.g. useful if the commutator

$$\left[A,e^B\right]=\sum_{n=0}^{\infty}\frac{1}{n!}[A,B^n] \tag{C.27}$$

is considered. Inserting (C.26) into (C.27) yields

$$\left[A, e^{B}\right] = \sum_{n=0}^{\infty} \frac{1}{n!} \sum_{m=0}^{n-1} B^{n-1-m} \left[A, B\right] B^{m}. \tag{C.28}$$

being zero whenever the operators A and B commute.

Appendix D

Interaction Picture

Having a Hamiltonian of form

$$H(t) = H_0 + V(t) \tag{D.1}$$

the interaction picture is defined by

$$|\psi_I(t)\rangle := U_0^+(t, t_0)\,|\psi_S(t)\rangle \tag{D.2}$$

with the unitary transformation

$$U_0(t, t_0) := e^{-\frac{i}{\hbar}H_0(t-t_0)}. \tag{D.3}$$

where the subscript $_S$ stand for the usual Schrödinger picture and the subscript $_I$ for the interaction picture. Note that t_0 is the point in time where the Schrödinger and interaction picture coincide, $|\psi_I(t_0)\rangle = |\psi_S(t_0)\rangle$, and can be chosen arbitrarily. Inserting (D.2) and (D.3) in

$$\begin{aligned}
|\psi_S(t)\rangle &= U_S(t, t')\,|\psi_S(t')\rangle & \text{(D.4)}\\
|\psi_I(t)\rangle &= U_0^+(t, t_0)U_S(t, t')\,|\psi_S(t')\rangle & \text{(D.5)}\\
|\psi_I(t)\rangle &= U_0^+(t, t_0)U_S(t, t')U_0(t', t_0)\,|\psi_I(t')\rangle & \text{(D.6)}\\
|\psi_I(t)\rangle &= U_I(t, t')\,|\psi_I(t')\rangle & \text{(D.7)}
\end{aligned}$$

leads to the time-evolution operator in the interaction picture

$$U_I(t, t') = T_D\; e^{-\frac{i}{\hbar}\int_{t'}^{t} dt'' V_I(t'')} \tag{D.8}$$

with Dyson's time-ordering operator T_D, ordering the operators in the exponential in such away that operators at later times occur first [104]. The required transpositions to achieve such an ordering are performed without sign changes. By requiring that the expectation value of some observable A is independent of the chosen picture one finds that an operator transforms in the following way:

$$A_I(t) = U_0^+(t, t_0)A_S U_0(t, t_0) \tag{D.9}$$

Appendix E

Keldysh Contour

The aim of this appendix is to show how one can write following expression

$$U_I^+(t,t_0)\hat{A}_I(t)U_I(t,t_0) = \tilde{T}_D\left\{e^{-\frac{i}{\hbar}\int_t^{t_0}dt'\,\bar{H}_T^I(t')}\right\}\hat{A}_I(t)T_D\left\{e^{-\frac{i}{\hbar}\int_{t_0}^{t}dt'\,\bar{H}_T^I(t')}\right\} \tag{E.1}$$

as a single exponential operator function. This is rather useful in order to write down a systematic perturbative expression in as straight forward manner. Expanding both exponentials this formula reads

$$\sum_{l,m=0}^{\infty}\frac{1}{m!l!}\left(-\frac{i}{\hbar}\right)^{l+m}\tilde{T}_D\left\{\left[\int_t^{t_0}dt'\bar{H}_T^I(t')\right]^l\right\} \hat{A}_I(t)T_D\left\{\left[\int_{t_0}^{t}dt'\bar{H}_T^I(t')\right]^m\right\}. \tag{E.2}$$

In order to write this expression as one single exponential function one has to collect all terms of order $n = l + m$. Since there are $n + 1$ terms of order n the sum over l and m can be rewritten into one sum over all orders n and a second sum running from 0 to n. The denominator $l!m!$ transforms to $k!(n-k)!$ and hence this expression reads

$$\sum_{n=0}^{\infty}\frac{1}{n!}\left(-\frac{i}{\hbar}\right)^{n}\sum_{k=0}^{n}\frac{n!}{k!(n-k)!}\tilde{T}_D\left\{\left[\int_t^{t_0}dt'\bar{H}_T^I(t')\right]^k\right\} \hat{A}_I(t)T_D\left\{\left[\int_{t_0}^{t}dt'\bar{H}_T^I(t')\right]^{n-k}\right\}. \tag{E.3}$$

Introducing the Keldysh time-ordering operator T_K ordering those operators on the forward integration path from t_0 to t according to T_D and those operators on

the backward path the other way round it is possible to write

$$\sum_{n=0}^{\infty} \frac{1}{n!} \left(-\frac{i}{\hbar}\right)^n T_K \left\{ \sum_{k=0}^{n} \frac{n!}{k!(n-k)!} \right. \\ \left. \left[\int_t^{t_0} dt' \bar{H}_T^I(t')\right]^k \left[\int_{t_0}^{t} dt' \bar{H}_T^I(t')\right]^{n-k} \hat{A}_I(t) \right\}. \quad \text{(E.4)}$$

Hence the sum over k is nothing else than the binominal formula such that

$$\sum_{n=0}^{\infty} \frac{1}{n!} \left(-\frac{i}{\hbar}\right)^n T_K \left\{ \left[\int_t^{t_0} dt' \bar{H}_T^I(t') + \int_{t_0}^{t} dt' \bar{H}_T^I(t')\right]^n \hat{A}_I(t) \right\}. \quad \text{(E.5)}$$

Introducing the Keldysh integration contour $\int_K = \int_{t_0}^{t} + \int_t^{t_0}$ this operator can be written as a single exponential operator function

$$U_I^+(t,t_0)\hat{A}_I(t)U_I(t,t_0) = \; T_K \left\{ e^{-\frac{i}{\hbar}\int_K dt' \bar{H}_T^I(t')} \hat{A}_I(t) \right\}. \quad \text{(E.6)}$$

Appendix F

Separation of Reservoir and Dot Operators

In calculating a quantum statistic expectation value as in Eq. (4.19) following sequence of lead and dot operators occur

$$\hat{T}_K \left\{ a_{k_1}^+(t_1) c_{l_1}(t_1) c_{l_2}^+(t_2) a_{k_2}(t_2) \cdots c_{l_n}^+(t_n) a_{k_n}(t_n) \hat{A}(t) \right\}. \tag{F.1}$$

In order to apply Wick's theorem to the reservoir operators it is necessary to separate those operators form the rest of this sequence. Since the a_k's are reservoir and the c_l's are dot operators the following anti-commutator relations hold

$$[a_k, c_l]_+ = \left[a_k^+, c_l^+\right]_+ = \left[a_k, c_l^+\right]_+ = \left[a_k^+, c_l\right]_+ = 0. \tag{F.2}$$

Looking at a specific time-ordering of Eq. (F.1) one notices that there have to be always as many annihilator as creator operators otherwise the trace performed in (4.19) would be zero. Therefore a phase-factor $(-1)^{n/2}$ is caught by ordering reservoir and dot operators of the same time t_i such that the reservoir operator occurs always first

$$(-1)^{\frac{n}{2}} a_{k_1}^+(t_1) c_{l_1}(t_1) a_{k_2}(t_2) c_{l_2}^+ \cdots \hat{A}(t) \cdots a_{k_n}(t_n) c_{l_n}^+(t_n). \tag{F.3}$$

In the case of the reduced density matrix $\hat{A}(t) = \hat{P}_{ss'}(t)$ the reservoir operators do commute with $\hat{A}(t)$. Moving the second reservoir operator next to the first one leads to a minus sign since this operator had to interchange place with one dot operator. The third reservoir operator needs to interchange twice its place with a dot operator in order to get separated and so on. Therefore an additional phase of $(-1)^{1+2+3....n-1} = (-1)^{n(n-1)/2}$ is caught leading to

$$(-1)^{\frac{n^2}{2}} a_{k_1}^+(t_1) a_{k_2}(t_2) \cdots a_{k_n}(t_n) c_{l_1}(t_1) c_{l_2}^+ \cdots \hat{A}(t) \cdots c_{l_n}^+(t_n). \tag{F.4}$$

Since only even orders n have non-zero contributions this phase factor is always $+1$ and can be dropped. Note that the time-ordering within each type of operators

did not change such that one can write for the general case

$$\hat{T}_K \left\{ a^+_{k_1}(t_1) c_{l_1}(t_1) c^+_{l_2}(t_2) a_{k_2}(t_2) \cdots c^+_{l_n}(t_n) a_{k_n}(t_n) \hat{A}(t) \right\} = \\ \hat{T}_K \left\{ a^+_{k_1}(t_1) a_{k_2}(t_2) \cdots a_{k_n}(t_n) \right\} \hat{T}_K \left\{ c_{l_1}(t_1) c^+_{l_2}(t_2) \cdots c^+_{l_n}(t_n) \hat{A}(t) \right\} . \quad \text{(F.5)}$$

In the case of calculating the tunneling current the operator $\hat{A}(t)$ has the same structure as the tunneling Hamiltonian and the reader might easily verify that the separation does again lead to no additional phase factor.

Appendix G

Co-tunneling Energy Integrals

In order to numerically treat the energy integrals occurring for the co-tunneling diagrams it is useful to write them in terms of residua and Cauchy principal value integrals. Fortunately it turns out that there are only two different kind of integrals occurring. The first kind can be written such that the inner integral has only one pole. Those integrals appear for all diagrams with a reservoir line starting before and ending after the second reservoir line, irrespective one which time branch the vertices are. All other diagrams lead to inner integrals with two poles. Those integrals are further on called integrals of second kind. Beyond that, each integral type is in the following subdivided into four different types which differ only by some signs.

G.1 Integrals of 1st Kind

The first two integrals of 1st kind look like

$$\int_{-\infty}^{\infty} dx \frac{f(x)}{(a-x+i0^+)(b-x+i0^+)} \int_{-\infty}^{\infty} dy \frac{g(y)}{\pm(q(x)-y)+i0^+}. \tag{G.1}$$

Using Dirac's identity

$$\lim_{\nu\to 0^+} \int_{-\infty}^{\infty} \frac{f(x)}{a-x+i\nu} dx = P\int_{-\infty}^{\infty} \frac{f(x)}{a-x} dx - i\pi f(a) \tag{G.2}$$

and rewriting the integrand in partial fractions

$$\frac{1}{(a-x+i0^+)(b-x+i0^+)} = \frac{1}{b-a}\left[\frac{1}{(a-x+i0^+)} - \frac{1}{(b-x+i0^+)}\right] \tag{G.3}$$

this integral reads for the case $a \neq b$

$$\begin{aligned} = \quad & \frac{1}{b-a}\left[\pm P\int_{-\infty}^{\infty} dx \frac{f(x)\chi_g(q(x))}{a-x} \mp P\int_{-\infty}^{\infty} dx \frac{f(x)\chi_g(q(x))}{b-x}\right. \\ & +\pi^2 f(b)g(q(b)) - \pi^2 f(a)g(q(a)) \\ & +i\pi P\int_{-\infty}^{\infty} dx \frac{f(x)g(q(x))}{b-x} - i\pi P\int_{-\infty}^{\infty} dx \frac{f(x)g(q(x))}{a-x} \\ & \left.\pm i\pi f(b)\chi_g(q(b)) \mp i\pi f(a)\chi_g(q(a))\right]. \end{aligned} \tag{G.4}$$

In case $a = b$ one can integrate by parts

$$\int_{-\infty}^{\infty} \frac{f(x)}{(a-x+i0^+)^2} dx = \left.\frac{f(x)}{a-x+i0^+}\right|_{-\infty}^{\infty} - \int_{-\infty}^{\infty} \frac{f'(x)}{a-x+i0^+} dx$$

leading to following expression

$$\begin{aligned} = \quad & \mp P\int_{-\infty}^{\infty} dx \frac{f'(x)\chi_g(q(x))}{a-x} \mp P\int_{-\infty}^{\infty} dx \frac{f(x)q'(x)\chi_{g'}(q(x))}{a-x} \\ & +\pi^2 f(a)q'(a)g'(q(a)) + \pi^2 f'(a)g(q(a)) \\ & +i\pi P\int_{-\infty}^{\infty} dx \frac{f(x)q'(x)g'(q(x))}{a-x} + i\pi P\int_{-\infty}^{\infty} dx \frac{f'(x)g(q(x))}{a-x} \\ & \pm i\pi f(a)q'(a)\chi_{g'}(q(a)) \pm i\pi f'(a)\chi_g(q(a)) \end{aligned} \tag{G.5}$$

where the following function has been introduced

$$\chi_g(u) = P\int_{-\infty}^{\infty} dy \frac{g(y)}{u-y}. \tag{G.6}$$

The other two types of integrals of the 1st kind are

$$\int_{-\infty}^{\infty} dx \frac{f(x)}{(x-a+i0^+)(x-b+i0^+)} \int_{-\infty}^{\infty} dy \frac{g(y)}{\pm(q(x)-y)+i0^+}. \tag{G.7}$$

Similarly to the previous two integrals it is found that for $a \neq b$

$$\begin{aligned} = \quad & \frac{1}{b-a}\left[\pm P\int_{-\infty}^{\infty} dx \frac{f(x)\chi_g(q(x))}{a-x} \mp P\int_{-\infty}^{\infty} dx \frac{f(x)\chi_g(q(x))}{b-x}\right. \\ & -\pi^2 f(b)g(q(b)) + \pi^2 f(a)g(q(a)) \\ & +i\pi P\int_{-\infty}^{\infty} dx \frac{f(x)g(q(x))}{b-x} - i\pi P\int_{-\infty}^{\infty} dx \frac{f(x)g(q(x))}{a-x} \\ & \left.\mp i\pi f(b)\chi_g(q(b)) \pm i\pi f(a)\chi_g(q(a))\right]. \end{aligned} \tag{G.8}$$

and for the case of $a = b$

$$\begin{aligned} = \quad & \mp P\int_{-\infty}^{\infty} dx \frac{f'(x)\chi_g(q(x))}{a-x} \mp P\int_{-\infty}^{\infty} dx \frac{f(x)q'(x)\chi_{g'}(q(x))}{a-x} \\ & -\pi^2 f(a)q'(a)g'(q(a)) - \pi^2 f'(a)g(q(a)) \\ & +i\pi P\int_{-\infty}^{\infty} dx \frac{f(x)q'(x)g'(q(x))}{a-x} + i\pi P\int_{-\infty}^{\infty} dx \frac{f'(x)g(q(x))}{a-x} \\ & \mp i\pi f(a)q'(a)\chi_{g'}(q(a)) \mp i\pi f'(a)\chi_g(q(a)). \end{aligned} \tag{G.9}$$

G.2 Integrals of 2nd Kind

The first type of an integral of 2nd kind reads

$$\int_{-\infty}^{\infty} dx \frac{f(x)}{a-x+i0^+} \int_{-\infty}^{\infty} dy \frac{g(y)}{(d-x-y+i0^+)(b-y+i0^+)}. \tag{G.10}$$

After substituting $z = d - x$ one can write this integral as

$$\begin{aligned} = \quad & P\int_{-\infty}^{\infty} dz \frac{f(d-z)\xi_b(z)}{d-a-z} - \pi f(a)\varphi_b(d-a) \\ & +i\left[P\int_{-\infty}^{\infty} dz \frac{f(d-z)\varphi_b(z)}{d-a-z} + \pi f(a)\xi_b(d-a)\right] \end{aligned} \tag{G.11}$$

where the functions $\xi_b(z)$

$$\xi_b(z) = \begin{cases} \frac{1}{b-z}\left[\chi_g(z) - \chi_g(b)\right] & \text{for } z \neq b, \\ -\chi_{g'}(b) & \text{for } z = b \end{cases} \tag{G.12}$$

and $\varphi_b(z)$

$$\varphi_b(z) = \begin{cases} \frac{\pi}{b-z}\left[g(b) - g(z)\right] & \text{for } z \neq b, \\ \pi g'(b) & \text{for } z = b. \end{cases} \tag{G.13}$$

have been introduced. The other types of integrals of 2nd kind are

$$\begin{aligned} & \int_{-\infty}^{\infty} dx \frac{f(x)}{a-x+i0^+} \int_{-\infty}^{\infty} dy \frac{g(y)}{(y-x-d+i0^+)(y-b+i0^+)} \\ & \quad = P\int_{-\infty}^{\infty} dz \frac{f(z-d)\xi_b(z)}{a+d-z} - \pi f(a)\varphi_b(a+d) \\ & \qquad -i\left[P\int_{-\infty}^{\infty} dz \frac{f(z-d)\varphi_b(z)}{a+d-z} + \pi f(a)\xi_b(a+d)\right], \end{aligned} \tag{G.14}$$

$$\int_{-\infty}^{\infty} dx \frac{f(x)}{x-a+i0^+} \int_{-\infty}^{\infty} dy \frac{g(y)}{(x+y-d+i0^+)(y-b+i0^+)}$$
$$= -P \int_{-\infty}^{\infty} dz \frac{f(d-z)\xi_b(z)}{d-a-z} + \pi f(a)\varphi_b(d-a)$$
$$+i \left[P \int_{-\infty}^{\infty} dz \frac{f(d-z)\varphi_b(z)}{d-a-z} + \pi f(a)\xi_b(d-a) \right], \qquad \text{(G.15)}$$

$$\int_{-\infty}^{\infty} dx \frac{f(x)}{x-a+i0^+} \int_{-\infty}^{\infty} dy \frac{g(y)}{(d+x-y+i0^+)(b-y+i0^+)}$$
$$= -P \int_{-\infty}^{\infty} dz \frac{f(z-d)\xi_b(z)}{a+d-z} + \pi f(a)\varphi_b(a+d)$$
$$-i \left[P \int_{-\infty}^{\infty} dz \frac{f(z-d)\varphi_b(z)}{a+d-z} + \pi f(a)\xi_b(a+d) \right]. \qquad \text{(G.16)}$$

Notice that the only difference between the 1st and 3rd as well as between the 2nd and 4th integral type is a sign change of the real part.

Bibliography

[1] S. I. Association, *International Technology Roadmap Semiconductors (ITRS) Update* (PUBLISHER, USA, 2002).

[2] L. Jacak, P. Hawrylak, and A. Wójs, *Quantum Dots* (Springer, Berlin, 1997).

[3] L. P. Kouwenhoven *et al.*, *in Mesoscopic Electron Transport, edited by L. L. Sohn, L. P. Kouwenhoven, and Gerd Schön* (Kluwer Academic Publishers, Dordrecht, Boston, London, 1997), pp. 105–214.

[4] H. Schoeller, *in Mesoscopic Electron Transport, edited by L. L. Sohn, L. P. Kouwenhoven, and Gerd Schön* (Kluwer Academic Publishers, Dordrecht, Boston, London, 1997), pp. 291–330.

[5] L. P. Kouwenhoven, G. Schön, and L. L. Sohn, *in Mesoscopic Electron Transport, edited by L. L. Sohn, L. P. Kouwenhoven, and Gerd Schön* (Kluwer Academic Publishers, Dordrecht, Boston, London, 1997), pp. 1–44.

[6] L. S. Kuz'min and K. K. Likharev, JETP Lett. **45**, 495 (1987).

[7] J. B. Barner and S. T. Ruggiero, Phys. Rev. Lett. **59**, 807 (1987).

[8] J. H. F. Scott-Thomas *et al.*, Phys. Rev. Lett. **62**, 583 (1989).

[9] M. Büttiker, Phys. Rev. B. **46**, 12485 (1992).

[10] H. Schoeller and G. Schön, Phys. Rev. B. **50**, 18436 (1994).

[11] D. V. Averin and A. A. Odintsov, Phys. Lett. A **140**, 251 (1989).

[12] D. V. Averin and Y. V. Nazarov, Phys. Rev. Lett. **65**, 2446 (1990).

[13] L. J. Geerligs, D. V. Averin, and J. E. Mooij, Phys. Rev. Lett. **65**, 3037 (1990).

[14] J. Weis, R. J. Haug, K. von Klitzing, and K. Ploog, *in Quantum Dynamics of Submicron Structures, edited by H. A. Cerdeira, B. Kramer, and G. Schön* (Kluwer Academic Publishers, Dordrecht, Boston, London, 1995), pp. 263–274.

[15] L. P. Kouwenhoven, D. G. Austing, and S. Tarucha, Rep. Prog. Phys. **64**, 701 (2001).

[16] U. Banin and O. Millo, Annu. Rev. Physn Chem. **54**, 465 (2003).

[17] D. Pfannkuche and S. E. Ulloa, Phys. Rev. Lett. **74**, 1194 (1995).

[18] D. Weinmann *et al.*, Europhysics Letters **26**, 467 (1994).

[19] D. Weinmann, W. Häusler, and B. Kramer, Phys. Rev. Lett. **74**, 984 (1995).

[20] K. Jauregui, W. Häusler, D. Weinmann, and B. Kramer, Phys. Rev. B. **54**, 1713 (1996).

[21] A. P. Jauho, *in Theory of Transport Properties of Semiconductor Nanostructures, edited by Eckehard Schöll* (Chapman and Hall, London, 1998), pp. 127–172.

[22] M. H. Cohen, L. M. Falicov, and J. Phillips, Phys. Rev. Lett. **6**, 316 (1962).

[23] F. Schwabl, *Quantenmechanik* (Springer, Berlin, 1998), Vol. 1.

[24] D. K. Ferry and S. M. Goodnick, *Transport in Nanostructures* (Cambridge University Press, United Kingdom, 1997).

[25] D. Pfannkuche, *Habilitation Thesis* (Universität Karlsruhe, Germany, 1999).

[26] *Single-Charge Tunneling: Coulomb Blockade Phenomena in Nanostructures, edited by H. Grabert and M. Devoret* (Plenum, New York, 1992).

[27] J. Weis, *Habilitation Thesis* (Universität Stuttgart, Max-Planck-Institut für Festkörperforschung, Germany, 2002).

[28] M. R. Deshpande, J. W. Sleight, M. A. Reed, and R. G. Wheeler, Phys. Rev. B. **62**, 8240 (2000).

[29] P. R. König, *PhD Thesis* (Universitätsbibliothek und technische Informationsbibliothek, Hannover, Germany, 2000).

[30] E. Bonet, M. M. Deshmukh, and D. C. Ralph, Phys. Rev. B. **65**, 045317 (2002).

[31] D. Weinmann, *PhD Thesis* (Physikalisch-Technische Bundesanstalt, PTB-Bericht PTB-PG-4, Braunschweig, 1994).

[32] W. Häusler, Z. Phys. B **99**, 551 (1996).

[33] X. Peng, J. Wickham, and A. P. Alivisatos, J. Am. Chem. Soc. **120**, 5343 (1998).

[34] E. Lifshitz *et al.*, NANO LETTERS **3**, 857 (2003).

[35] X. Peng *et al.*, NATURE **404**, 59 (2000).

[36] N. Tessler *et al.*, Science **295**, 1506 (2002).

[37] H. Mattoussi *et al.*, Journal of Applied Physics **83**, 7965 (1998).

[38] M. C. Schlamp, X. Peng, and A. P. Alivisatos, Journal of Applied Physics **82**, 5837 (1997).

[39] B. O. Dabbousi, M. G. Bawendi, O. Onitsuka, and M. F. Rubner, Applied Physics Letters **66**, 1316 (1995).

[40] V. L. Colvin, M. C. Schlamp, and A. P. Alivisatos, NATURE **370**, 354 (1994).

[41] N. C. Greenham, X. Peng, and A. P. Alivisatos, Phys. Rev. B. **54**, 17628 (1996).

[42] V. I. Klimov *et al.*, Science **290**, 314 (2000).

[43] M. Kazes *et al.*, Advanced Materials **14**, 317 (2002).

[44] M. B. Jr. *et al.*, Science **281**, 2013 (1998).

[45] W. C. W. Chan and S. Nie, Science **281**, 2016 (1998).

[46] D. L. Klein *et al.*, NATURE **389**, 699 (1997).

[47] M. G. Bawendi *et al.*, Phys. Rev. Lett. **65**, 1623 (1990).

[48] H. Park *et al.*, Applied Physics Letters **75**, 301 (1999).

[49] B. Alperson *et al.*, Applied Physics Letters **75**, 1751 (1999).

[50] B. Alperson, S. Cohen, I. Rubinstein, and G. Hodes, Phys. Rev. B. **52**, 17017 (1995).

[51] E. P. Bakkers and D. Vanmaekelbergh, Phys. Rev. B. **62**, 7743 (2000).

[52] E. Bakkers, Z. Hens, L. Gurevich, and D. Vanmaekelbergh, Nanotechnology **13**, 1 (2002).

[53] E. Bakkers *et al.*, NANO LETTERS **1**, 551 (2001).

[54] L. Gurevich, L. Canali, and L. P. Kouwenhoven, Nanostructured Materials and Devices 3 (2001).

[55] O. Millo, D. Katz, Y. Cao, and U. Banin, Phys. Rev. B. **61**, 16773 (2000).

[56] U. Banin, Y. Cao, D. Katz, and O. Millo, Letters to Nature **400**, 542 (1999).

[57] D. Katz, O. Millo, S.-H. Kan, and U. Banin, Applied Physics Letters **79**, 117 (2001).

[58] O. Millo, D. Katz, Y. Cao, and U. Banin, Phys. Stat. Sol. **224**, 271 (2001).

[59] V. L. Colvin, A. N. Goldstein, and A. P. Alivisatos, J. Am. Chem. Soc. **114**, 5221 (1992).

[60] T. Maltezopoulos *et al.*, Phys. Rev. Lett. **91**, 196804 (2003).

[61] O. Millo, D. Katz, Y. Cao, and U. Banin, Phys. Rev. Lett. **86**, 5751 (2001).

[62] B. Grandidier *et al.*, Phys. Rev. Lett. **85**, 1068 (2000).

[63] E. E. Vdovin *et al.*, Science **290**, 122 (2000).

[64] D. J. Norris and M. G. Bawendi, Phys. Rev. B. **53**, 16338 (1996).

[65] A. I. Ekimov *et al.*, J. Opt. Soc. Am. B **10**, 100 (1993).

[66] S. Lee *et al.*, Phys. Rev. B. **63**, 195318 (2001).

[67] Y. Niquet, C. Delerue, G. Allan, and M. Lannoo, Phys. Rev. B. **65**, 165334 (2002).

[68] A. J. Williamson and A. Zunger, Phys. Rev. B. **59**, 15819 (1999).

[69] L. Brus, Journal of Chemical Physics **79**, 5566 (1983).

[70] L. Brus, Journal of Chemical Physics **80**, 4403 (1984).

[71] D. I. Chepic *et al.*, Journal of Luminescence **47**, 113 (1990).

[72] C. R. Pidgeon and R. N. Brown, Phys. Rev. **146**, 575 (1966).

[73] A. L. Efros and M. Rosen, Annu. Rev. Mater. Sci. **30**, 475 (2000).

[74] U. Banin *et al.*, Journal of Chemical Physics **109**, 2306 (1998).

[75] L. I. Schiff, *Quantum Mechanics* (Springer, Berlin, 1993).

[76] M. G. Burt, J. Phys.: Condens. Matter **4**, 6651 (1992).

[77] G. W. Bryant, *private communication.*

[78] Slater, *Quantum Theory of Atomic Structure* (McGraw-Hill, New York, 1960), Vol. 2.

[79] G. Goldoni *et al.*, Physica E **6**, 482 (2000).

[80] L. D. Hallam, J. Weis, and P. Maksym, Phys. Rev. B. **53**, 1452 (1996).

[81] T. Brocke *et al.*, Physica E (in press).

[82] T. Brocke *et al.*, Phys. Rev. Lett. **91**, 257401 (2003).

[83] R. J. Warburton *et al.*, Phys. Rev. B. **58**, 16221 (1998).

[84] D. Leonard *et al.*, Applied Physics Letters **63**, 3203 (1993).

[85] H. Drexler *et al.*, Phys. Rev. Lett. **73**, 2252 (1994).

[86] M. Tews and D. Pfannkuche, Phys. Rev. B. **65**, 073307 (2002).

[87] M. Tews and D. Pfannkuche, Proceedings of 26th International Conference on the Physics of Semiconductors, Edinburgh (2002).

[88] R. Wiesendanger, *Scanning Probe Microscopy and Spectroscopy*, 1 ed. (Cambridge University Press, Cambridge, 1994).

[89] D. J. Griffiths, *Introduction to Electrodynamics* (Prentice, Hall, 1998).

[90] O. Madelung, *Semiconductors-Basic Data*, 2nd revised ed. (Springer, Berlin, 1996).

[91] B. S. Kim, M. A. Islam, L. E. Brus, and I. P. Herman, Journal of Applied Physics **89**, 8127 (2001).

[92] J. König, H. Schoeller, and G. Schön, Phys. Rev. Lett. **78**, 4482 (1997).

[93] J. König, *PhD Thesis* (Shaker Verlag, Aachen, 1999).

[94] A. E. Hanna, M. T. Tuominen, and M. Tinkham, Phys. Rev. Lett. **68**, 3228 (1992).

[95] D. C. Glattli *et al.*, Condensed Matter **85**, 375 (1991).

[96] D. C. Glattli, Physica B **189**, 88 (1993).

[97] C. Pasquier, U. Meirav, F. I. B. Williams, and D. C. Glattli, Phys. Rev. Lett. **70**, 69 (1993).

[98] C. Pasquier *et al.*, Surface Science **263**, 419 (1992).

[99] H. Matsuoka and S. Kimura, Jpn. J. Appl. Phys. **34**, 1326 (1995).

[100] D. J. Paul, J. R. A. Cleaver, H. Ahmed, and T. E. Whall, Phys. Rev. B. **49**, 16514 (1994).

[101] S. D. Franceschi *et al.*, Phys. Rev. Lett. **86**, 878 (2001).

[102] H. Schoeller, *Habilitation Thesis* (Universität Karlsruhe, Fakultät für Physik, Germany, 1997).

[103] Y. Funabashi, K. Ohtsubo, M. Eto, and K. Kawamura, Jpn. J. Appl. Phys. **38**, 388 (1999).

[104] G. D. Mahan, *Many-Particle Physics* (Plenum Press, New York, 1981).

Curriculum Vitae

Name:	**Michael Tews**
02/20/1974	born in Nürtingen
08/1980-07/1984	*Ersbergschule Nürtingen* (elementary school)
08/1984-07/1991	*Neckar-Realschule Nürtingen* (primary school)
08/1991-06/1994	*Technisches Gymnasium Kirchheim/Teck* (secondary school); graduated on June 24, 1994 obtaining the Abitur
07/1994-09/1995	civil service in the *Karl-Olga Haus Friedrichshafen* (nursing home)
10/1995-07/1998	*Universität Stuttgart*; Vordiplom on October 2, 1997
08/1998-05/2000	*Michigan Technological University*, Houghton, Michigan; graduated on April 11, 2000 with a Master of Science in Physics
05/2000-07/2000	*Philips Medical Systems*, Hamburg; industrial trainee
since 10/2000	dissertation at the *Universität Hamburg*

Selbständigkeitserklärung

Hiermit erkläre ich, die vorliegende Arbeit selbständig ohne fremde Hilfe verfaßt und nur die angegebene Literatur und Hilfsmittel verwendet zu haben.

Michael Tews
06. Januar 2004